JAIST Repository
https://dspace.jaist.ac.jp/

Title	ソフトロボティクスにおける感覚及び把握を促進する適応形態学の研究
Author(s)	QI, Qiukai
Citation	
Issue Date	2021-03
Type	Thesis or Dissertation
Text version	ETD
URL	http://hdl.handle.net/10119/17474
Rights	
Description	Supervisor:HO, Anh Van, 先端科学技術研究科, 博士

JAPAN
ADVANCED INSTITUTE OF
SCIENCE AND TECHNOLOGY

Japan Advanced Institute of Science and Technology

A Study of Adaptive Morphology That Facilitates Sensing and Grasping in Soft Robotics

Qiukai QI

Japan Advanced Institute of Science and Technology

Doctoral Dissertation

A Study of Adaptive Morphology That Facilitates Sensing and Grasping in Soft Robotics

Qiukai QI

Supervisor: Associate Professor Van Anh Ho

Graduate School of Advanced Science and Technology
Japan Advanced Institute of Science and Technology
Information Science

March 2021

Abstract

The past few decades have seen a rapid growth of robotic research in many fields including, for example, industry, medical care, entertainment and education. Conventional robots are typically fabricated with metals and plastics that are resistant to deformation. While these robots can perfectly complete their jobs in closely structured environment because of speed, precision and predictability, they raise severe challenges in those scenario characterized by human interactions due to concerns about safety.

Soft robotics has been expected to compensate the situations where their rigid cousins fail to function, as they usually employ compliant and adaptive materials that could potentially serve as a safety layer when interacting with humans. Therefore, safety, adaptability and autonomy have long been preferred to achieve with soft robotics. However, despite the ubiquitous research on soft robotics during last decade, there is yet an effective principle or methodology to design soft robots with adaptive behavior. Embodied intelligence, or embodiment, in this situation delivers profound insights on robot intelligence. It considers that the intelligence of robotics lies not merely in the control domain ("brain"), but in the combination of brain, body, and the interaction with environment. In this sense, the morphology of robotic body is a source of intelligence that can potentially shape the functionality of soft robots. Consequently, morphology that is adaptive, coined as adaptive morphology, has been a popular theme for soft robotics.

Adaptive morphology has the potential to enable adaptive behavior of soft robots. It can either optimize the performance or add new functions to existing robotic agents. Despite the numerous successful demonstrations, adaptive morphology has been dominantly investigated in terms of robotic actuation. The kingdom of robotic sensing, however, has remained largely unexplored. Even within the actuation, there are still many questions to be answered, for example, the role of adaptive behavior in improving the energy efficiency. To this end, this thesis attempts to bridge the gap by studying how adaptive morphology can influence, or facilitate in specific, sensing and grasping of soft robotics, based on our work on two prototypes, "WrinTac" and "RetracTip".

WrinTac is a soft tactile sensor that has been formed in wrinkle morphology. When actuated by stretching or bending, the wrinkle morphology can change its wavelength and magnitude continuously thus varying the sensing property of the sensing element embedded in the wrinkle bump. The fabrication process was simulated using finite element method (FEM) to show the effectiveness, and the morphological changes were characterized by analytic and FEM modeling. It was found that the more it is stretched or bent, the longer the wavelength is and the stiffer the overall structure becomes, which all affecting the sensing ability of the sensor. In order to find out how the morphological changes influence the sensing functionality, we examined the sensitivity to normal and tangential force. Further, we implemented two tasks, shape discrimination and texture detection, to study the influence by the adaptive morphology. In shape classification, we adopted machine learning (decision tree, k nearest neighbors and supporting vector machine) and deep learning techniques (convolutional neural network) as the "brain" to perceive the difference. In texture detection, we used Fast Fourier Transform (FFT) to analyze the performance and found the optimal morphology for this task. Finally, we found out that there is always an optimal morphology for different task and the adaptive morphology offers promising opportunity to adapt the sensor morphology to different tasks and environments based on the specific performance.

RetracTip is an universal and energy-efficient gripper coupled with sensing functionality. It is capable of gripping objects of arbitrary size and shapes. The design was initially inspired by the sea anemone while can find its artificial ancestor that is a tactile sensor with dome shape fingerprints on the external surface. By comparing RetracTip with its artificial predecessor, we demonstrated that how the morphology can be utilized and optimized in order to augment the original design with gripping functionality. Additionally, we demonstrated how the energy efficiency was improved by integrating a bistable morphing dome structure thus eliminating the requirement for continuous power input during object-holding action that is a common posture for pick and place scenario. Specifically, we investigated the sensing and gripping functionality individually by implementing tasks including self-state sensing, direction and terrain detecting, and gripping force testing and object gripping testing. Then, by implementing an autonomous gripping system, we validated the potential of this design towards future autonomous robots.

The findings in this thesis demonstrate the potential of adaptive morphology in shaping the sensing behavior, maximizing the information gain, and bringing about autonomous and energy efficient gripping functionality of soft robotics. It is shown that adaptive morphology could be utilized to design future soft robotics with adaptive sensation and energy efficient actuation.

Keywords: Adaptive morphology, Soft robotics, Tactile sensors, Soft grippers, Morphological computation

Acknowledgments

I would like to thank my supervisors Dr. Van Anh Ho, who has offered me the opportunity to work on this interesting topic and guided me through the whole process, and Dr. Shogo Okada for his necessary discussions. Many thanks to my collaborators, Prof. Shinichi Hirai and Dr. Zhongkui Wang, for their useful advises on our collaborated work. I am thankful to all my colleagues in Soft Haptics Lab. for their very kind support and understanding, and my dear friends in JAIST, Dr. Haoran Xie, Dr. Longchuan Li, Dr. Fayong Liu and many others, for their important information over the years. Special thanks to Prof. Jonathan Rossiter and Dr. Helmut Hauser for their intimate supervision during my visiting at the SoftLab Group in University of Bristol, and to all my colleagues there, especially Dr. Jianglong Guo, Dr. Chaoqun Xiang, Dr. Martin Garrad and Dr. Krishna Manaswi Digumarti, who helped me to settle down during initial days and afterwards and who have provided countless help to my research. I would like to thank Dr. Michael Wasielewski for his very kind host and useful discussions when I was visiting Delft Haptics Lab. in TU Delft. I also would like to thank the examiners of this dissertation, Dr. Kohei Nakajima, Dr. Hiromi Mochiyama, Prof. Ryuhei Uehara, Prof. Nak Young Chong, Dr. Shogo Okada, for their time spent on checking the thesis and offering their valuable and insightful comments. I am grateful to my families who have supported me both mentally and financially. Many many thanks to my girlfriend, Fengwei Dai, for her company and constantly cheering me up during my down time. I love you.

Table of Contents

Abstract **i**

Acknowledgments **iii**

Table of Contents **iv**

List of Figures **vii**

List of Tables **xv**

Acronym and Abbreviation **xvii**

1 Introduction **1**

- 1.1 Adaptive Morphology 2
- 1.2 Motivations 3
- 1.3 Contributions 3
  - 1.3.1 Adaptive morphology facilitating sensing functionality 4
  - 1.3.2 Adaptive morphology facilitating gripping functionality 4
- 1.4 Structure of Thesis 4

2 Adaptive Morphology **6**

- 2.1 Introduction 6
- 2.2 Enabling Technology 7

2.2.1 Shape changing 8
2.2.2 Variable stiffness 8
2.3 Adaptive Morphology in Actuation 9
2.3.1 Stability, damping and impact response 9
2.3.2 Load capacity 10
2.3.3 Energy efficiency 10
2.3.4 New functionality 11
2.4 Adaptive Morphology in Sensing 11
2.4.1 Sensing range and sensitivity 11
2.4.2 Perception performance 12
2.5 Adaptive Morphology in Computation 12
2.6 Summary 13

3 Adaptive Morphology Facilitating Sensing : WrinTac Based on Stretching Actuation 14

3.1 Introduction 14
3.2 Related Works 16
3.2.1 Sensorized soft body 16
3.2.2 Bio-inspired active tactile sensing system 16
3.2.3 Variable afferent network morphology 16
3.3 Wrinkle Morphology 17
3.3.1 Mimicking abstraction 17
3.3.2 Understanding wrinkle morphology through modeling 18
3.4 Design and Fabrication 21
3.5 Experiments and Results 23
3.5.1 Self-deformation 24

3.5.2 Interaction 25
3.6 Discussion 31
3.7 Conclusion 32

4 Adaptive Morphology Facilitating Sensing : WrinTac Based on Bending Actuation 34

4.1 Introduction 34
4.2 Related Works 35
4.2.1 Active tactile sensing 35
4.2.2 Biomimetic researches of fingerprints on tactile sensor 36
4.2.3 Texture and shape detection with tactile sensation 37
4.2.4 Comparison with previous design 37
4.3 Fabrication, Characterization and Finite Element Modeling 37
4.3.1 Fabrication 37
4.3.2 Geometrical characterization of wrinkle structure 38
4.3.3 Finite element modeling 39
4.4 Experiments and Results 42
4.4.1 Normal indention 43
4.4.2 Shape discrimination 44
4.4.3 Texture detection 48
4.5 Discussion 51
4.6 Conclusion 52

5 Adaptive Morphology Facilitating Gripping Functionality : RetracTip 55

5.1 Introduction 55
5.2 Related Works 57
5.2.1 Robotic grippers 57

5.2.2 Tactile sensing in robotics 58
5.2.3 Energy efficiency and bistable structures 59
5.3 Concept, Simulation and Design 59
5.3.1 Concept 59
5.3.2 Design and simulation 61
5.4 Experiments and Results 63
5.4.1 Experimental setup and methodology 64
5.4.2 Sensing 66
5.4.3 Gripping 68
5.4.4 Friction Modulating 69
5.4.5 Autonomous Gripping Control 70
5.5 Discussion 70
5.6 Conclusion 72

6 Conclusions and Outlook **74**
6.1 Summary of Contributions 74
6.2 Conclusions 75
6.3 Outlook 76

Bibliography **79**

Publications **93**

List of Figures

2.1 Illustrations of adaptive morphology with examples in computation, sensing and actuation. It indicates the properties of each category that can be influenced by the adaptive morphology. The sample illustration in computation is adapted from [1]. 7

3.1 Wrinkle-based morphology inspired soft sensing system with tactile perception: (a) By stretching and releasing, embedded strain gauge's posture, as well as electrical response change, resulting in self-deformation response. (b) The sensor in various morphology (wrinkle magnitude and wavelength) responds differently to even same sliding stimuli. 15

3.2 Imagination of variable afferent network morphology (VANmorph). Embedded sensor inside soft body does not need to be fixed, instead it can vary its relative posture. Interaction with sensor under various postures leads to different dynamic responses. (a), (b) and (c) illustrate posture changes (angular) of embedded sensor in three modes. 17

3.3 An implementation example of VANmorph: a multi-layered structure consists of a thick, soft layer covered by a thin, inextensible, flexible film with a strain gauge sandwiched in between. Slope of the bump changes in response to the actuation (compression in this case)and so do the posture and sensitivity surface of the strain gauge. 18

3.4 Illustration for derivation of wrinkle numbers over a substrate with length l, and a film layer with length L. It is assumed that, at the stable state, the height from the tip of the wrinkle to the original surface (before formation) decreases correspondingly to the increased number of wrinkle over a certain length. 19

3.5 The fabrication setup. (a) Ecoflex 00-50 is poured into a mould, vacuumized and cured to form the soft substrate with length l. (b) The substrate is clamped on a motorized linear stage and stretched to length L. (c) A thin film with length L is glued to the substrate. 22

3.6 The experimental setup for preliminary evaluation: The X linear stage stretches and releases the soft body and X-Z stage performs indention and sliding. A loadcell was installed on the X-Z stage to measure the force and data was transmitted to computer through an ADC data acquisition box. The strain gauge output was measured by a strain measurement device with a built-in Wheaston bridge. 23

3.7 Verification of the embedded strain gauge's posture during self-deformation, extracted from consecutive images of the strain gauge: (a) The original, grey-scaled and edged images of the wrinkled soft body. (b) Inclined angles of the strain gauge during self-deformation, implying remarkable change in orientation of the sensing element during morphological change of wrinkles. 24

3.8 Strain gauge output in form of strain [μm/m]. (a) Under self-deformation (stretching and releasing) condition. It shows approximately linear relation with stretching strain of the substrate. The output hysteresis is considered to be due to the viscoelasticity of silicone rubber. Inset graph shows enlarged view of data mean and standard deviation. (b) Under step stretching (up to 2%) and releasing condition. The response is rather timely and steady even though there is a gradual output decreasing because of the stress relaxation behaviour viscoelastic material. 26

3.9 (a) Normal indention (1 N) test under step stretching input. Response consists of two parts, stretching and indention. Static response to each step stretching agrees with previous section and that to indention can measure the sensitivity to normal indention, where steps 6, 7 and 8 show larger sensitivity than the rest. (b) Illustration of two trade-off factors on sensitivity variance. The effect of stain gauge (positive) is dominant in small stretching strain while stiffness change effect (negative) is in charge after a critical stretching strain. 27

3.10 (a) Normal indention test with various forces at two stretching strains, case 1 with 14% and case 2 with 20%. Case 1 performs better sensitively than case 2 at lower forces. Inset graph shows enlarged view of data mean and standard deviation. (b) Illustration of normal indention in two cases. When larger force is applied, Case 1 undergoes a combination of indention and constraint from both sides while case 2 is subjected to combination of stretching and indention. 28

3.11 Response of soft sensor to forward and backward sliding. (a) The response of sensor with various state of wrinkle is different, where wrinkle with stretching rate at 14% outperforms the others. (b) Illustration of a typical forward sliding mechanism. 29

3.12 (a) Repeated response to forward sliding with different shapes of probe in the case with wrinkle (30 times each). The spherical and cone probes are similar in term of time spanning while the former has a negative peak with larger absolute value. The time span of flat probe response is larger than the others thanks to its larger contact surface, and it gives a more stable response when sliding over the wrinkle 1. (b) Mean and standard deviation of each trial. It gives a glimpse that how distinguishable each shape is. . . 33

4.1 (A) An envisioned future application scenario: texture exploration with the wrinkled tactile sensor on a robotic finger. (B) The morphological variation of wrinkles is actuated by joint rotation mimicking joint movement of human fingers. When it rotates clockwise, the sensor is bent thus wrinkle magnitude shorten, wavelength prolonged, overall stiffness increased. All contribute to variation of sensor property, offering the chance to optimize perception by adapting sensor morphology. 35

4.2 Illustration of scenario when human stroke with finger a surface of fine while detectable texture. (A) Palpation with slight pressing force. (B) Palpation with larger force. As observed, upon pressing harder, the soft tissue between textures and mechanoreceptors becomes locally thinner, denser and stiffer, benefiting vibration detection. 36

4.3 Sensor fabrication process. (A) Ecoflex00-20 was mixed with the weight ratio of Part A:B being 1:1, then poured into a 3D printed mold. (B) The whole model was degassed and cured at room temperature in a vacuum oven. (C) The sensing element and kapton tape were attached in sequence to the pre-stretched substrate. (D) After 5 minutes for glue drying, the pre-stretch was released. (E) Wrinkle structure formed on top with sensing element located at one wrinkle bump. (F) Another tape was attached to the bottom for easy integration into experimental platform. 38

4.4 Geometrical modeling of sensor, where geometrical property of wrinkle structure can be approximated by that of the characterization triangle marked in red. Symbols and definitions are listed in Table 4.1. 39

4.5 The wrinkling process of proposed sensor in Finite Element Modeling. This is a two-step analysis, where step - 1 is the pre-stretching of the substrate and step - 2 includes attachment of film and strain gauge, and release of pre-strteching. It shows merely step - 2 as wrinkle forms in this stage. The stress is expressed in Mpa. (A) Initial state of step - 2 where three boundary conditions were set. (B) Wrinkling process with two insets, one showing node displacement along vertical direction from initial state and the other the stress distribution. It shows that where there is no vertical displacement in Inset - 1, there is minimum stress in Inset - 2. 41

4.6 Simulation of sensor bending behavior. (A) - (H) Morphological difference when bent by different angles. As observed, the more the bending is, the shorter the wrinkle magnitude and longer the wavelength. Note that the modeling was performed as a symmetric structure while visualized as a whole. The colormap was expressed in mm. 42

4.7 Experimental setup and wrinkle morphological variation under different bending states. (A) - (F) Different bending states showing the same trend of morphology change as in Fig. 4.6. Since the strain gauge was embedded at one side of wrinkle bump, its orientation changes during bending as well. θ indicates the bending angle. 43

4.8 (A) The loading cases while sensor was bent by $\theta=\pi/3$. The sensor was pressed up to a normal force threshold while reading recorded. The same pressing was repeated for each of [0.1, 0.2, 0.3, 0.4, 0.5] N. Inset - 1 is a closeup showing step response manner. (B) The response profiles to a series of normal forces as in (A) when sensor is under various bending angles [0, $\pi/6$, $\pi 4/3$, $\pi/2$, $2\pi/3$, $5\pi/6$, π]. The sensitivity to stimuli under 0.3 N was affected by a combination of two factors that are the inclined angle of strain gauge and the overall stiffness, as verified in [2]. While sensitivity to larger force was dominantly tuned by the latter. 45

4.9 Architecture of the convolutional neural network, in which feature of signal was extracted by four convolutional layers and four pooling layers before it was flattened and fed to a fully connected network with one hidden layer for final classification. The overhead number indicates the data structure of that layer. 47

4.10 Sensor reading when indenter of different shapes slides on it with two speed options, 8 mm/s in (A) and 4 mm/s in (B). C, S and W indicate the shapes, namely semi-Cylinder, Square and Wedge, respectively. The solid line indicates the average of 50 samples, and the shading area the standard deviation. The response patterns are quite constant within each shape, and unique compared with other shapes. Different speeds resulted in the same profile but in different time scale, indicating that the response pattern contains information unique to that indenter of particular shape. 48

4.11 Feature representation of sliding data with indenters of different shapes. Here, mean and standard deviation of each sliding data were extracted to represent one sliding sample. Panel (A), (B) and (C) show data points derived from sensor under $\theta = 0$, $\theta = \pi/3$ and $\theta = \pi$ in 3D (left) and 2D (right) spaces. Note that data in 3D coordinates are same data as those in 2D space but scattered by item number in order to visualize all the data points. Intuitively, sensor without bending shows most separable responses, as in panel (A). 49

4.12 Indenters with grooves of 0.1 mm (Texture 1) in (A) and of 0.2 mm (Texture 2) in (B). (C) & (D) show closeup views of Texture 1 & 2 by a violet laser microscope. Dotted lines with item number indicate sections of measurement, where widths in (C) are 127.143, 127.979, 99.720 μm and in (D) are 183.097, 201.105, 181.158 μm. Note that the groove edges are blurred since laser beam goes through transparent indenters, causing less reflection for clearer boundaries. 51

4.13 Sensor responses to sliding with two textures when sensor is under three banding states, $\theta = 0$ in (A), $\theta = \pi/3$ in (B) and $\theta = \pi$ in (C). Since two grooves slided over the sensor for 4 times, it is expected to detect 8 peaks. Obviously, the sensor can not find grooves on Texture 1 while was able to detect those on Texture 2. While it performed best when sensor was bent by $\pi/3$ as the distance between minimum peak and signal mean is most obvious, which limits the best sensitivity to that groove. This conclusion will be further justified by spectral analysis. 53

4.14 Illustration of texture detection scenarios. (A) When there is no wrinkle on sensor, no local deformation happens in between object and sensor. (B) Wrinkle of feasible size can extend itself and interact with texture more closely in order to respond during sliding. 54

4.15 FFT analysis of texture sliding signal when sensor is under three different bending states, $\theta = 0$ in (A), $\theta = \pi/3$ in (B) and $\theta = \pi$ in (C). While the sensor in all three bending states can find the real sliding frequency, the sensor bent by $\pi/3$ is argued to perform the best based on two observations, (1) compared with case of no bending, the ranking of the true sliding frequency in (B) is higher than in (A), making the true frequency more obvious among other components, (2) compared with bending case by π, true frequency has higher magnitude which infers sensitive detection of the true frequency. 54

5.1 Conceptual design of RetracTip and its engineering setup of an autonomous gripping system. Inset 1 is the biological structure of sea anemone and inset 2 is the bio-inspired structure of RetracTip. Insets 3 and 4 indicate the two states (“natural” and “retracted”) that enable the grip and release functionality. 56

5.2 Demonstration of preying process of sea anemones and the gripping and sensing functionality of RetracTip. (A)-(E) show the preying behaviors of sea anemone, and filming courtesy of Erlendur Bogason [3]. (F) - (J) present the spring-gripping process of RetracTip. The gripping is enabled by pressing RetracTip against the target to activate the snap-through behavior of RetracTip along which the wrapping movement of pins happens. (K) - (O) show the distribution of markers during the spring gripping process, demonstrating the sensing capability of RetracTip. 58

5.3 FEM simulation results of bistability of spherical caps and of RetracTip. (A) indicates the dimension of spherical caps. (B) and (C) present the typical behavior of monostability ($H < 3.3\,\mathrm{mm}$) and bistability ($H > 3.3\,\mathrm{mm}$), respectively. The colormaps show the displacement along Y-axis. (D) verifies the bistability of RetracTip before fabrication. 60

5.4 Mechanical design of RetracTip. 54 tapered pins and 61 markers are printed on a bistable membrane. The rigid core inside the pins is to stiffen them and the white cap on top of markers is for the tactile information tracking by the overhead camera sensor. External pneumatic source is used to trigger the snap-through and snap-back by vacuuming and pressurizing RetracTip via the tube joint. 61

5.5 The experimental setup. (A) overviews the system setup including control, power, pneumatic and motor systems. The control system consists of one main controller and two local controllers (DS 102 for the motor system and Arduino for the pneumatic system). The main controller synchronizes the sensing of RetracTip and the control of two local controllers. (B) illustrates the pneumatic system which is capable of vacuuming and pressurizing RetracTip by switching off/on the solenoid valve. A distributed control algorithm is implemented in local controller 2 (Arduino) which receives a control signal from the main controller. 63

5.6 Two gripping modes and the corresponding characterization of griping capability. (A) shows the schematic of two gripping modes, that is, grasping and pinching, depending on the size of objects. (B) indicates the experimental setup for the characterization experiments in (C) the gripping size testing and in (D) the gripping force testing. The gripping size testing was performed by examining the successful rate of gripping a series of spherical objects with various diameters. The gripping force testing was conducted for the two gripping modes by selecting the size of targets. 64

5.7 Demonstration of gripping capability. (A) – (H) show the gripping of a series of printed objects by grasping (A) - (D) and by pinching (E) - (H). (I) – (P) present the gripping of various daily objects, from those that are rigid to those that are thin, soft and flexible. 67

5.8 Friction modulation testing. (A) is the experimental setup and (B) presents the friction rate for two stable states of RetracTip. The friction can be tuned very effectively by selecting either. 69

5.9 The control flowchart of the RetracTip control system. 70

5.10 The trade-off relationship between two functionalities (gripping and friction modulating) induced by the variance of pin length (L) and membrane depth (H). Both functionalities can be achieved simultaneously only when a suitable ratio of the two parameters (L, H) is selected as in (A). 71

List of Tables

3.1 Shape Classification Results 31

4.1 Nomenclatures (refer to fig. 4.4) 40

4.2 Learning Results (Classification Accuracy) 47

4.3 Information about Lower Peak 52

5.1 Results for Proprioceptive and Exteroceptive Sensing 65

Acronym and Abbreviation

DOF	Degrees of freedom
FEM	Finite element method
FFA	Flexible fluidic actuator
SMM	Shape memory material
SME	Shape memory effect
FEA	Finite element analysis
DEA	Dielectric elastomer actuator
EAP	Electro active polymer
IEAP	Ionic electro active polymer
MR	Magneto rheological
ER	Electro rheological
HMA	Hot melt adhesive
PAM	Pneumatic artificial muscle

Chapter 1

Introduction

Robots are autonomous machines capable of sensing their environments, computing to make decisions, and actuating to act in the real world [4]. They are usually designed to serve human beings [5] in a variety of fields and scenarios, such as industry, healthcare, and entertainment [6–8]. Despite the fact that, after a few decades of development, many intelligent and capable robots can execute various tasks and outperform human beings in terms of speed, accuracy and precision in well structured environments, outside there they are still not able to complete basic tasks that humans can perform with ease and elegance, for example unlocking doors with keys. Conventionally, robots are made of rigid materials (metal or plastic) that are resistant to deformation. This, on the one hand, is beneficial as so robots can achieve high level of load capability, repeatability, predictability and precision, but on the other hand is potentially dangerous to humans and other assets around the robots, which is a key consideration in humans oriented situations such as medical and educational applications [9]. Therefore, robots are increasingly required to be able to work alongside humans in unknown and dynamic environments with improved safety, adaptivity, and autonomous capability.

Soft robots provide a promising solution towards development of future multi-functional and energy efficient robotic systems with adaptivity and robustness [9, 10]. They are soft and compliant intrinsically, thus safe during interaction with surrounding humans and other animals. They are usually lightweight such that they need less energy for actuation. They exploit novel functional materials, which enables functional diversity and behavioural adaptivity rarely seen on their conventional rigid counter parts. The use of soft materials offers new opportunities for seamless integration of sensing, actuation, computation and even communication within basic materials and simple structures [11, 12], creating more lift-like intelligent robots with enhanced functional diversity while with reduced control complexity [13]. For example, the universal jamming gripper surprisingly simplified the gripping of a wide range of objects with arbitrary sizes and shapes, which, otherwise, would be only possible with very closely coupled sensory motor coordination in rigid gripper systems [14].

Despite a number of successful and interesting demonstrations, soft robotics is still in its infancy thus there are still many challenges to overcome [9]. One is that, due to the distinguishing differences between soft and rigid robotics, for example the inherent softness, the existing design framework for traditional robotics is no more suitable for the newcomer. Novel design approaches and insights are needed.

Embodiment has been demonstrated to be an effective design principle for soft robotics [13]. Typically, it sees robotic components not separately but jointly as a whole for designing, and considers that the properties and performance of the functional components, such as sensors and actuators, are strongly influenced and shaped by the physical body scheme they are incorporated as well as by the interaction between them and their environments. Further, as a branch notion of embodiment, morphological computation views morphology of an agent as a source of intelligence in that smartly designed soft robots can “offload” part of the computational burden from the central controllers to the physical body [15]. These notions are particularly useful for designing future environmentally adaptive robots as they both emphasize that the morphology and the interaction with environment should be considered.

Many morphological exploitations have been done in soft robotics, including those for sensors, actuators and whole robots [16–19]. One robotic component, when in different morphology, can usually have either optimized, shifted or altered functionality that depending on the level of the difference. It has been increasingly recognized that there is a coupling relationship between morphology and functionality. From this point of view, a robot with a uniquely fixed morphology would somehow lose its functional diversity, thereby compromising in its behavioural adaptivity to the environment. In this case, variable and adaptive morphology enabling the robustness of soft robots in large task space and dynamic environment is highly required [20].

1.1 Adaptive Morphology

Living creatures manoeuvre adaptive and variable morphology actively in their daily activities to tackle uncertainties and optimize performance in the open and ever-changing world [21]. Humans, for example, tune their postures during motion on different terrains in order to obtain optimal body dynamics. Birds change their wing morphology (e.g. the degree of extension) to aid the shift among different flying patterns. In sensing and perception, eyes, as sensors, can actively regulate the amount of light that enters into it in order to fit to environment with different lightness. To trace sound from various directions, ears actively reorientate themselves for better sensation and perception. Adaptive morphology is crucial for living beings to optimize their behavioural performance, extend their operational space, and improve their multi-functionalities.

Inspired by these biological insights, scientists are beginning to incorporate changeable and adaptive morphology in robotics with the hope to bring these intelligent machines to a new level in terms of robustness, adaptivity and autonomy [21]. Initial explorations have been done in such fields as compliant, modular, swarm, evolutionary as well as soft robotics. While each field has its particularly unique approaches, shape-changing and variable stiffness are two common technologies that have been applied overall [22–24]. Here, it is not trivial to clarify the definition and scope of the term, morphology. This notion, in initial works, was applied to refer to the geometrical characteristics such as shape of body and placement of sensors, excluding those material properties [13]. Nonetheless, it is now increasingly utilised to describe property about geometry and material [16, 17], which, in the author's belief, is more suitable for the generalization of the idea, morphological computation, thereby is adopted through out this thesis.

1.2 Motivations

The majority of research about adaptive morphology sit in the area of conventional robots [21]. Despite a few number of morphological investigations in soft robotics [25], adaptive morphology that purposively adjusts itself and fits to specific workload has remained largely untouched. To bridge this gap, thus drawing insights for designing future soft robots that are more intelligent, adaptive, robust and autonomous, this study concentrates on the adaptive morphology in soft robotics and to investigate how it can benefit the sensing and gripping functionality.

1.3 Contributions

Based on works on two soft robotic prototypes ("WrinTac" and "RetracTip") that have been proposed and developed with adaptive morphology, this study contributes to the field in mainly two aspects that are described below. Note that the two models are different and separate in design and function, but are same in terms of the main theme, adaptive morphology. They both have been designed with variable morphology which has a role to play in tuning the main functionality of each, sensing for WrinTac and gripping for

RetracTip.

1.3.1 Adaptive morphology facilitating sensing functionality

Research on soft sensor morphology in the literature prevailingly took the binary approach investigating how a particular morphology can aid achieving better performance of the sensor, thus to provide guidance for future sensor design. Sensors with adaptive morphology are very rare. Here, inspired by the water-induced wrinkle morphology on human fingers, we developed a soft tactile sensor with wrinkle morphology that is capable of adapting itself in shape and size to a given task. By integrating the adaptive morphology, the operational space was largely extended because the adaptive morphology enables multiple sensitivity options and it affects the performance in tasks such as shape classification and texture detection. Therefore, this study contributes to the early investigation of adaptive wrinkle morphology in soft tactile sensing. It is expected to pave the way potentially for active sensing with a novel methodology, that is, morphological adaptation, which is believed to be cheaper computationally, instead of sensory motor coordination.

1.3.2 Adaptive morphology facilitating gripping functionality

Pick and place is an common task for soft robotic manipulation. Most soft grippers need continuous energy input when holing an object before placing, which is less efficient in energy. RetracTip overcomes this challenge by integrating an adaptive morphing membrane in its compact pin-patterned design. The membrane is bistable so that it can settle at either of its two stable configurations. The gripping and releasing functionality is realized by the snapping-through and snapping-back process of the pinned membrane. Compared with its predecessor, TacTip which is a tactile sensor based on visual information, this gripper is enabled by the embedding of the adaptive morphology, demonstrating that the adaptive morphology can extend the functionality of soft robotics, as well as optimize the functional performance.

1.4 Structure of Thesis

Followed the introduction, next chapter provides a brief review of the technology and early investigation of adaptive morphology applied in soft robotics. Prevailing technologies and existing models are presented in a comparative manner, providing some background knowledge in this theme. Subsequently, the following chapters concentrate on the main contributions claimed above. Chapter 3 and Chapter 4 present the work on WrinTac based on stretching and bending actuation, respectively, demonstrating the potential of adaptive morphology to benefit sensing functionality. Chapter 5 introduces the development and evaluation of RetracTip to show the beneficial effect of adaptive morphology on achievement of energy-efficient gripping functionality. Based on the aforementioned content, chapter 6 discusses the pros and cons and points out some improvement to be implemented in the future before briefly concluding the thesis.

Chapter 2

Adaptive Morphology

This chapter presents a review of recent progress for soft robotic research on adaptive morphology. The enabling technologies in general will be identified, then the implementation in sensing, actuation and computation will be summarized and the benefits of each category highlighted.

2.1 Introduction

Embodied intelligence suggests that morphology is of crucial role in shaping the functions of agents [26]. In this perspective, morphology that is variable and adaptable, coined as adaptive morphology, offers agents a series of functional variations, thereby providing the opportunity to adapt their functions to different environments and tasks. Biological beings actively exploit the morphological variance for different purposes. Birds, for example, morph their wings and tails to obtain different aerodynamics when switching over among multiple flying modes [27]. Elephants, as shown in Fig 2.1, selectively stiffen their trunks for different exerting forces. Mammals, such as rats, reorientate their sensory organs for optimized sensing and perception, as in Fig. 2.1. The adaptive morphology has been key to their adaptivity and robustness.

Adaptive morphology has been applied to intelligent robotics design in order to obtain additional functions and optimize performance [21]. A flying drone equipped with adaptive morphology (foldable arms) can enter and navigate narrower spaces where fix morphology drone could not enter because of the body size [28]. A walking robot with shape morphing joint embedded in legs presents multiple trajectories with simple actuation [29]. Actuators with variable stiffness or impedance were investigated to achieve functional adaptivity, such as energy efficiency [30, 31]. In order to obtain adaptive morphology, these previous research usually involves with integration of components that are morphologically variable and adjustable.

Soft materials are potential to bring robotics to an unprecedented level of adaptivity because of the intrinsic softness which enables their morphological diversity [21]. Compared with rigid materials, soft materials deform more easily, thus requiring less driving energy for morphing. Therefore, soft technologies have been prevailingly exploited for adaptive morphology. The enabling technologies, materials and existing models are reviewed herein. Note that morphology, as stated in last chapter, refers to, in a more general perspective, both the geometrical, such as size and shape, and the material properties.

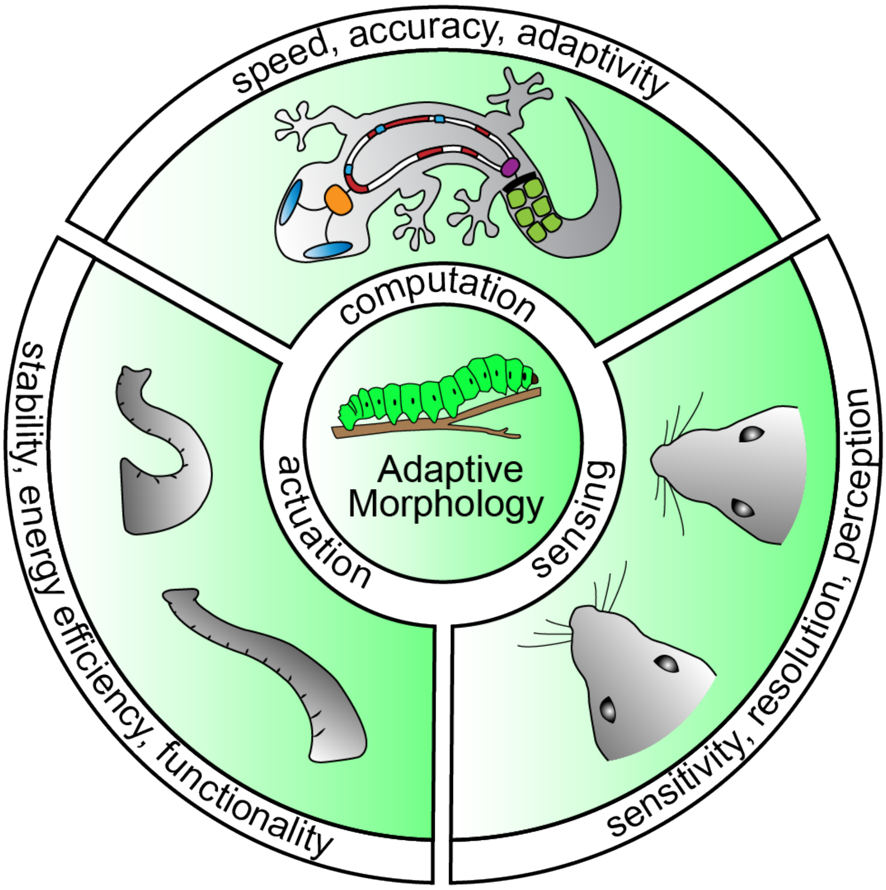
speed, accuracy, adaptivity
stability, energy efficiency, functionality
sensitivity, resolution, perception
computation
actuation
sensing
Adaptive Morphology

Figure 2.1: Illustrations of adaptive morphology with examples in computation, sensing and actuation. It indicates the properties of each category that can be influenced by the adaptive morphology. The sample illustration in computation is adapted from [1].

2.2 Enabling Technology

Biological beings employ different approaches and mechanisms to acquire complex behaviours for survival from dynamic environment. One prevailing strategy is shape changing [23, 32]. For example, octopuses reshape their body in order to enter or squeeze out from openings much narrower than their normal size. In this category, the term “shape” contains not only the physical shape of the agent, but also the other geometrical parameters such as orientation of key elements within a system, which have an effect on the overall shape. Rats, for example, alter the orientations of the whiskers to better sense the world [33]. Here, the whiskers as a whole can be seen as a tactile sensor and its shape varies because of the orientation changes. Another approach commonly adopted is variable stiffness, in which through adjusting the stiffness agents can achieve desired kinematic and dynamic behaviour [24]. One typical example is the selective stiffening in elephant trunk, a hydrostatic structure, mentioned earlier. The two categories do not exclude each other completely because one can be triggered by the other passively, for example shape changes always lead to stiffness variations. Nonetheless, they provide a framework to effectively classify the existing designs and materials in the literature.

2.2.1 Shape changing

The shape changing research of soft robotics have been concentrated on the functional materials and mechanisms [23]. Among the quite a few interesting examples, the stimuli-responsive materials have stayed at the center. For example, Robert *et al.* developed a morphing limb with thermoset material and flexible fluidic actuator (FFA), capable of shape morphing in order to suit to different locomotion, swimming or walking [34]. Another example is the robot by Shah and colleagues [35]. They combined a morphing skin made of cable stitched fabric and a FFA locomotion skin to generate a robot that can morphing in order to avoid obstacles during motion. As with novel mechanisms and structure, origami is an interesting approach. In [36], the authors reported an origami morphing skin capable of changing the structure dramatically by folding. Lee *el al.* proposed an origami wheel structure enabling the vehicle equipped with it moving across a wide range of distinct terrains [37].

2.2.2 Variable stiffness

There are mainly two prevailing strategies to realize variable and adjustable stiffness [24]. One is to implement active actuators in an antagonistic arrangement, and the other is the usage of functional materials and mechanisms.

The former category usually involves a combination of a active actuator and at lease one other component, active or passive, and exploits the equilibrium position of the whole structure. For example, Suzumori *et al.* proposed a structure that consists of a bundle of McKiben actuators arranged antagonistically [38]. By selectively pressurizing or vacuumizing each particular actuator, the structure can vary its stiffness effectively. Another example adopted the active-passive combination was presented in [39]. Here, the authors fabricated octopus arm with variable stiffness by integrating shape memory alloy, that is the active part, into a passive hollow tube. A variety of actuating technologies have been employed, including flexible fluidic actuator (FFA), shape memory materials (SMM), electro-active polymers (EAP) and tendon-driven actuators. Literately each can be utilised with another one jointly, enabling numerous opportunities.

As for the second strategy, a variety of functional materials and mechanisms have been investigated, which includes jamming, SMM, magneto- (MR) and electrorheological (ER) and low melting point materials [24]. As exemplified in [14], the jamming structures change the stiffness significantly enabled by the pressure changes. Different jamming mechanisms have been developed, including fibre jamming [40], layer jamming [41], and tubular jamming [42]. Shape memory effects on SMM are realized due to their phase or glass transitions which can vary the mechanical property [24]. The transition is usually triggered by temperature and other energy sources such as light, electric field. Variable stiffness structures with MR and ER technology usually employ the MR and ER material together with other soft materials which constrain the movement of MR and ER materials [43, 44]. Similar to SMM, the low melting point materials are another category that changes elastic modulus considerably because of the glass transition phenomenon [45].

2.3 Adaptive Morphology in Actuation

Adaptive morphology has been applied to robotic actuation either to optimize performance or to gain new functions [21]. For example, a soft crawling robot can change its dynamic posture when passing over different terrains [46], which otherwise would be impossible with fix body morphology. In this section, a brief review of such application in soft actuation will be presented with a focus on what benefits could possible be obtained from adaptive morphology. Note that the complete robots whose function are mainly enabled by actuation, for example the crawling robot, will be included as well.

2.3.1 Stability, damping and impact response

Adaptive morphology can be explored to achieve improved static and dynamic stability and the damping property for soft actuation. Aktas and colleagues composed layer jamming beams in a flexure structure that is promising to provide precise motion control without friction and wear issues [47]. By modulating the pressure of the layer jamming beams, the impedance of the flexure can be adjusted dramatically, thus the characteristics of damping and impact response tuned effectively. Further, these property variations have been demonstrated to influence the control and positioning accuracy.

2.3.2 Load capacity

Adaptive morphology, variable stiffness in particular, can tune the profile of exerting force to meet different requirements. For example, Yang *et el.* developed an actuator with variable stiffness enabled by two actuators, one pneumatic actuator and the other supercoiled polymer (SCP) actuator, arranged antagonistically [48]. The SCP actuator contracts when heated, thus providing the diving power. When different force profile is required, the soft actuator can selectively actuate the pneumatic actuator and the SCP to modulate the overall stiffness, thus the load-bearing characteristics. Another example combined the pneumatic and layer jamming actuation to create soft actuators with variable stiffness capability [49]. The actuator can adjust its stiffness significantly when the jamming layers are vacuumized. Further, two actuators, as gripping fingers, were implemented in a gripper which was found to be able to provide multiple gripping force options. A similar structure can be found in [50], where instead of layer jamming, they utilized a chain-like structure to generate the granular jamming for stiffening.

2.3.3 Energy efficiency

Sun *et el.* introduced a soft morphing actuator with variable stiffness, which can bend and hold its position without the need for continues power input [51]. Within a soft material body, they integrated a twisted and coiled actuator (TCA) for bending and a polylactide (PLA) element for stiffness varying. When the PLA is soften, the TCA will drive the actuator to desired configuration. The PLA is then cooled down to stiffen until it is enough to hold the actuator in position. Depend on the specific application, the adaptive morphology enables the actuator to hold the posture with improved power efficiency by eliminating the holding energy input. A bending actuator with similar approach was presented by Buckner and co-workers [52]. Here, the two coupling components are pneumatic artificial muscles (PAMs) and synthesis of SMP for actuating and changing softness, respectively.

2.3.4 New functionality

Ruotolo *et el.* proposed a spiny paw structure with a particle jamming palm embedded [53]. When in its low stiffness state, the paw can comply to surfaces of arbitrary shapes, thus allowing the pins to extend to the concave details on the surface. The paw then stiffen the palm, thereby freezing the pin rotation to distribute the shear load more evenly to every contact pin. This design was implemented in a climbing robot and enabled the ability to climb steep rocky surface, which otherwise would have been impossible.

2.4 Adaptive Morphology in Sensing

Tactile sensing has been in the focus of soft robotics as it most typically involves touch or collision that is key for safety. In human, tactile sensing is mediated by the skin and the mechanoreceptors underneath [54, 55]. Tactile sensors for soft robots follow the same analogy, where usually sensing elements composed in a sensor body is involved. This scheme offers a role for morphology to play in shaping the functions of tactile sensor. There have been research studying how tactile sensors with different morphology lead to distinct performances [56–58]. While most existing research investigated discrete morphology, fewer have focused on morphology that is variable and adaptable comparatively.

2.4.1 Sensing range and sensitivity

Among the few research, quite an outstanding example is the work presented by Nurzaman and colleagues [59]. They implemented a active tactile sensing system that can adjust the morphology to suit for specific environments. To be specific, the sensor uses hot melt adhesive (HMA), a thermoplastic material, as sensing probe and a camera to convert deformation into other perceivable information such as force. When put in unstructured environments, the sensor can remove and reprint the probe with another shape and size, thus tuning the morphology to obtain enhanced performance including extended sensing range and adjustable sensitivity. Because of the thermoadhisive characteristic of HMA, the sensor can also detect temperature difference. Therefore, though simple function was demonstrated, this work presents an intuitive example to show that adaptive morphology is effective to tune the sensor characteristics.

2.4.2 Perception performance

Another morphology that is promising to be adaptive is the whisker sensor, which has been inspired by the vibrissae of rodents such as rats. Since the early demonstrations [60, 61], there have been a variety of solutions which typically include a physical whisker, rigid or soft, to contact targets, and a transduction mechanisms based on different sensing technologies such as capacitance and resistance [62, 63]. While early works focused on static and passive sensing, the concentration has been shifted to active sensing inspired by the fact that rats explore the environment with an active movement of their whiskers [64]. As an analogue, the artificial whisker with adaptive morphology is often enabled by a rotational mechanism that usually is located at the base [65, 66]. The morphology here refers to the orientation of the whiskers. Although it was most often studied in the perspective of sensori-motor coordination, the active process has been demonstrated to be able to improve the sensing and perception performance in tasks such as noise filtering, target localization and object exploration [64, 67]. Here, the active process was indeed realized because of the variable morphology, but further investigations in terms of adaptive morphology particularly are still needed to identify and characterize the benefits.

2.5 Adaptive Morphology in Computation

While conventionally research on computation or control of soft robotics remain dominantly in the algorithmic scope, of which the implementation always involves rigid computers and electronics, this review focuses on soft computers that can potentially be carried on by soft robotics and perform on-board computation and decision making. Such computers are envisioned to have flexible and compliant electronics embedded in soft bodies with variable morphology. An early such implementation was presented by Garrad *et el.* in [1]. In here, inspired by how animals use the vascular system, the authors demonstrated the concept of soft matter computers (SMCs) that consist of a vascular system for conductive fluid, a pumping system for liquid circulation, and a series of conductive fluid receptors (CFRs). By varying the length, offset and space of the CFRs, the soft computer is capable of switching, amplifying, filtering and digital logc computing. Further, they implemented this prototype to control a range of common soft robots including a worm robot, a soft gripper and a bending actuator, demonstrating outstanding performance and enormous potential of this computing mechanism.

Strictly speaking, Garrad *et el.* has yet essentially incorporated adaptive morphology in the SMC. Nonetheless, they included a soft body in the loop of computation, providing many chances to further introduce morphology that can be tuned to suit for different scenarios and to optimize performance. With these being said, a series of famous work by Nakajima *et al.* investigated the possibility of using soft material body for information processing and as robotic controllers [68–72], in which they found that the morphological property of the soft material, stiffness for example, has significant influence on the property of controllers. Similarly, another on-board control example was introduced by Mahon and co-workers in [73], in which they implemented a simple on-board controller / computer capable of switching between walking mode and gripping mode.

2.6 Summary

Compared with the investigations for actuation, the research of adaptive morphology in sensing and computation are far behind the schedule. The reasons, in part, might be that the adaptive behaviour in actuation is more effective tuning the actions of complete robot. For example, the modulated impedance find its role in affecting the body dynamics more than other aspects. In part it might because of the enabling technology such as manufacture and material development. Consider the case for computation. Fabricating a soft matter computer prototype is already ultra difficult, letting alone to let them meet the functional performance that are required for the soft robotics. However, each of the three components are essential for future autonomous robots to better suit for dynamic environment and open tasks. More attentions need to be put on sensing and computation.

Chapter 3

Adaptive Morphology Facilitating Sensing : WrinTac Based on Stretching Actuation

Abstract

This chapter presents the soft tactile sensor with adaptive wrinkled morphology, coined as “WrinTac”. Inspired by the water induced wrinkle structure on human fingertips, the wrinkle morphology on WrinTac is enabled by a multilayer structure, which, when stretched, varies in terms of magnitude, wavelength and overall stiffness. The morphological variation leads to some beneficial influences on the sensing functionality. A series of experiments to verify and evaluate this function-morphology relation are introduced and results presented. By doing so, it argues that adaptive morphology is beneficial for tactile sensing functionality, in that it extends the working range of the sensor, and improves the signal stability.

3.1 Introduction

Soft robots and their interaction behaviour with surroundings (objects, humans and environment) have been emerging in the field of robotics. The intrinsic characteristics of soft robots, infinite degree of freedom and great compliance, benefit such tasks as perception and manipulation on one hand, and on the other hand increase difficulties to apply traditional actuation and sensation methods [9]. For example, the embedded sensing element in soft body for tactile sensation responds to not only external interaction but

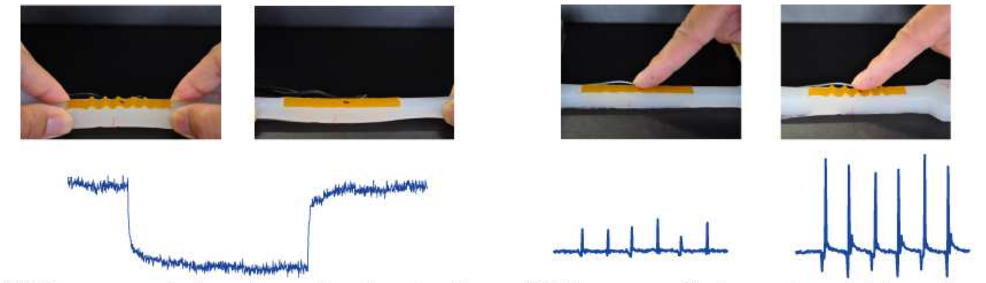
(a) Response during elongation/contraction (b) Response during external interaction

Figure 3.1: Wrinkle-based morphology inspired soft sensing system with tactile perception: (a) By stretching and releasing, embedded strain gauge's posture, as well as electrical response change, resulting in self-deformation response. (b) The sensor in various morphology (wrinkle magnitude and wavelength) responds differently to even same sliding stimuli.

also self-deformation, making it hard to distinguish them [74]. Most of recent work in this field attempted to solve each part separately [75] - [76].

Morphological computation has been utilized for recognizing novel mechanisms. Authors in [77] pointed out that geometrical shape and its mechanical properties may play a vital role for benefiting different perceptions, especially tactile sensing. However, sensing systems that can actually utilize their own morphology for different sensing tasks were barely found. Our previous work used pneumatic actuation for inflating a chamber covered by a skin layer to generate different morphology. Nonetheless, it introduced bulky external devices (compressor and its regulating circuit) [78]. Andrew *et al.* proposed a WormTIP design that adopts a dielectric elastomeric actuator (DEA) to make a sensory membrane capable of extending itself onto an object and conforming to the surface for better sensation. One concern is that DEA requires a large input voltage, thus not suitable for common applications [79].

This paper introduces the idea of Variable Afferent Network Morphology (referred as "VANmorph") to describe the phenomenon that soft sensor's morphological change (geometrical and mechanical properties) varies the sensing capability, and presents the implementation of VANmorph on a sensorized soft body inspired by the water-induced wrinkle on human fingers. The morphology of the sensor can be readily modulated by simply stretching and releasing in order to obtain different sensing capabilities as illustrated in Fig. 4.1, thus to benefit perception. The actuation mechanism is improved in that it can be possibly realized by less bucky actuator compared with previous work. Preliminary evaluation of the soft sensor reveals promising advantages of such design in facilitating tactile sensing and in implementing active sensing system.

3.2 Related Works

3.2.1 Sensorized soft body

Current designs of sensorized soft body focus on feedback of deformation information during operation of robots. These involves either smart selection of sensing element or dedicated application. Magnet sensor and light sensor were adopted repectively in [80] and [81] for detection of local curvnture of soft finger. Conductive fluid was selected in [82] and [83] to sense deformation of large body. Culha *et al.* proposed a method for realization of different deformation patterns, such as serpentine or twisting [84]. There are tons of promising approaches for specific feedback of deformation, yet no generic strategy for such sensorized soft body design. Hughes and Iida attempted to construct a framework for calculation of localized deformation based on differential outputs of embedded strain gauges. Nonetheless, the scalability of this framework is uncertain [74].

3.2.2 Bio-inspired active tactile sensing system

Tactile sensing is inspired by nature through mimicking not only anatomy of the touch organs, but also the combination of motory and sensory complex in active sensing of diverse stimuli [17]. For example, manatees can actively adjust the tactile hair follicle-sinus complexes for different sening environment [85]. In order to acomplish such task in robotic agents, both sensation and actuation are needed. A mobile robot was reported in [86] to be capable of actively adjusting its whiskers for better feedbacking location/vibration in different terrains. The self-actuating sensor of dielectric elastomeric actuator (DEA) in [79] can achieve active sensing by forming a sensory membrane, extending itself to an object and conforming to the surface for better sensation. These studies involve active sensing from the stance of motion control and processing algorithms.

3.2.3 Variable afferent network morphology

Current researches on sensing deformation are limited to static analysis for matching embedded sensor response and deformation amount. Since deformation of soft robot bodies have diverse patterns (bending, twisting, traction, localized deformation, and so on) and ambient environment is changing, static analysis might not be eligible for complex cases. We hereby propose the idea of VANmorph to describe the phenomenon that by changing the morphology of the soft body, sensing capability could be adjusted accordingly. VANmorph considers the ambient environment as illustrated in Fig. 3.2. Self-deformation and

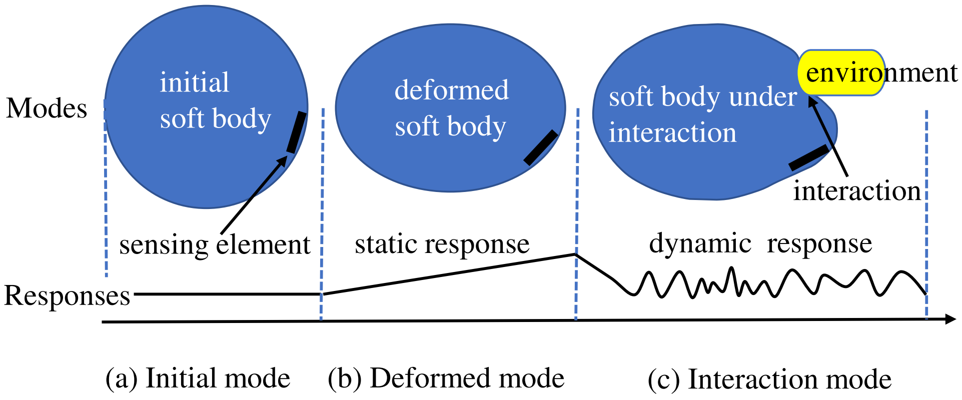
Modes
initial soft body
deformed soft body
soft body under interaction
environment
interaction
sensing element
static response
dynamic response
Responses
(a) Initial mode
(b) Deformed mode
(c) Interaction mode

Figure 3.2: Imagination of variable afferent network morphology (VANmorph). Embedded sensor inside soft body does not need to be fixed, instead it can vary its relative posture. Interaction with sensor under various postures leads to different dynamic responses. (a), (b) and (c) illustrate posture changes (angular) of embedded sensor in three modes.

external environment cause static and dynamic response of the embedded sensor respectively. By studying the mechanism of VANmorph, we expect to propose sensing systems with multiple sensing capabilities.

3.3 Wrinkle Morphology

3.3.1 Mimicking abstraction

Natural morphology provides a great source of hints and ideas for development of artificial applications. Wrinkle morphology as one of the most common phenomenon has been utilized in various ways in scientific and engineering researches, such as adhesion analysis of soft structures [87], measurement of mechanical properties [88], stretchable electronic devices [89] and so on. In this paper, we utilized the morphology of wrinkled surface to change the posture of the embedded sensing element with the purpose to vary the sensibility of the sensing element.

The mechanism of the wrinkle formation has long been considered to be due to the mismatch of expanding and shrinking ratio of different materials in a multi-layered structure [90]. A common way to generate this pattern is to compress inward two ends of a multi-layered structure that consists of a soft, thicker substrate and a thin, stiffer layer as illustrated in Fig. 3.3. The wavelength of the wrinkle patten (λ) decreases upon compressing, thus resulting in steeper edge of each bump and vice versa. Imagine that if a sensing element is embedded right under the skin layer near a bump edge, the posture

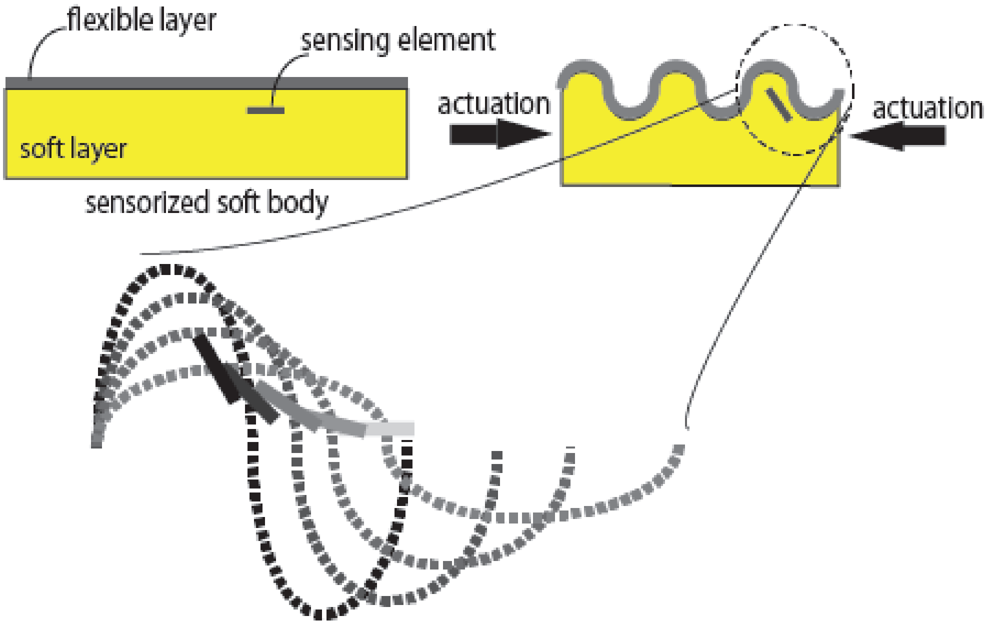

Figure 3.3: An implementation example of VANmorph: a multi-layered structure consists of a thick, soft layer covered by a thin, inextensible, flexible film with a strain gauge sandwiched in between. Slope of the bump changes in response to the actuation (compression in this case)and so do the posture and sensitivity surface of the strain gauge.

of the sensing element will change accordingly upon compressing. In this research, we chose strain gauge as the sensing element, but one can exploit other sensing elements such as pressure sensor, accelerator, magnet (with Hall sensor), and so on. When the wrinkle morphology changes, strain gauge's sensitive surface also varies, and so does its sensitivity with respect to the direction of applied external loads (normal indention or tangential traction). In this way, the sensing system possesses multiple sensing abilities which be selected among by changing the wrinkle morphology.

3.3.2 Understanding wrinkle morphology through modeling

There are quite a number of attempts to describe the wrinkles qualitatively or quantitatively on multi-layered structures. Wang and Zhao [90] introduced a phase diagram of surface instabilities for estimation of various wrinkle patterns induced by mismatch strain and they validated successfully this method with a finite element model using Abaqus. Cerda and Mahadevan build an analytical model wto depict the wrinkle patterns [91]. However, these models are complicated to understand for researchers in different areas. In this section, we attempted to build a simplified model for easier understanding the wrinkle's mechanism based on basic physics of bending and stretching, under the light of energy stability.

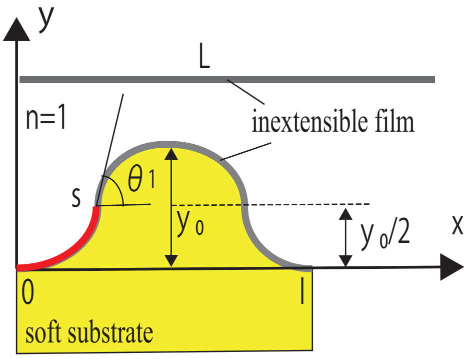

(a) When number of wrinkle n = 1

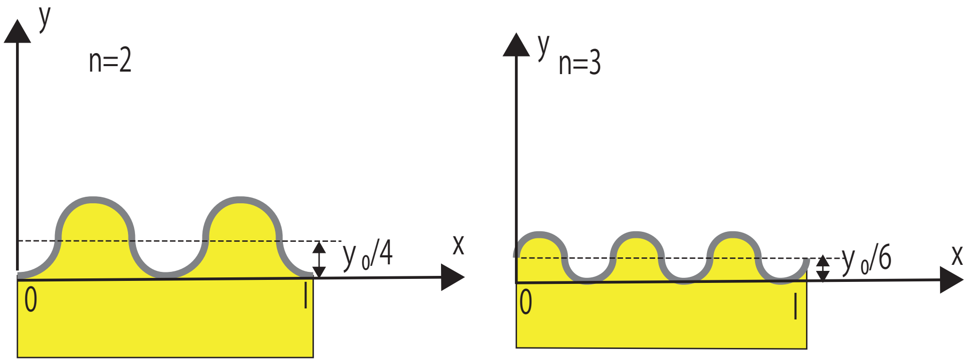

(b) When number of wrinkle n = 2 (c) When number of wrinkle n = 3

Figure 3.4: Illustration for derivation of wrinkle numbers over a substrate with length l, and a film layer with length L. It is assumed that, at the stable state, the height from the tip of the wrinkle to the original surface (before formation) decreases correspondingly to the increased number of wrinkle over a certain length.

The modelling was based on two assumptions: First, the structure stabilize where the energy in the system is minimal; Second, all wrinkle bumps in one configuration are identical in terms of geometry and each is with uniform curvature. Further, we assume that the wrinkle state has a length l with a number of sinusoidal wrinkles n. The value of n is an argument that minimizes the potential energy of the wrinkled surface as follows:

$$N = \underset{n}{\arg\min} \quad U = \underset{n}{\arg\min} \quad (U^n_{flex} + U^n_{sub}), \tag{3.1}$$

where U^n_{flex} and U^n_{sub} are flexural energy of the thin film and deformation energy of the soft substrate respectively.

In order to estimate flexural energy, we started with $n = 1$. The flexural energy of of the film can be calculated as follows:

$$U^{n=1}_{flex} = K_{bend} \int_0^L \left(\frac{d\theta_1(s)}{ds} \right)^2 ds, \tag{3.2}$$

where K_{bend} is the stiffness of the film material, and ds is an infinitesimal length along the film, and $\theta_1(s)$ is the function that defines the shape of the flexural film with respect to the length of the film L (see Fig. 3.4). When $n = 2$, corresponding flexural energy $U_{flex}^{n=2}$ is estimated similarly as:

$$U_{flex}^{n=2} = K_{bend} \int_0^L \left(\frac{d\theta_2(s)}{ds} \right)^2 ds. \tag{3.3}$$

Since the substrate's length l is unchanged, and the film is inextensible with $L = const$, it is sufficient to assume that $\theta_2(s) = \theta_1(2s)$. Flexural energy $U_{flex}^{n=2}$ is then calculated as:

$$U_{flex}^{n=2} = K_{bend} \int_0^L \left(2\frac{d\theta_1(s)}{ds} \right)^2 ds = 2^2 U_{flex}^{n=1}. \tag{3.4}$$

Similarly for other case of wrinkle number, a generic estimation of flexural energy at n wrinkle is derived as follows:

$$U_{flex}^{n=N} = N^2 U_{flex}^{n=1}. \tag{3.5}$$

We also attempted to estimate the energy of the substrate's deformation of n wrinkles based on mathematical induction from derivation of $U_{sub}^{n=1}$. Let peak height of a wrinkle when $n = 1$ be y_0, then deformation amount at a location $y_1(s)$ be $y_1(s) - y_0/2$. The potential energy related to this morphology is estimated as :

$$U_{sub}^{n=1} = K_{sub} \int_0^L \frac{1}{2} \left(y_1(s) - \frac{y_0}{2} \right)^2 cos\theta_1(s) ds, \tag{3.6}$$

where K_{sub} is the stiffness of the substrate material. When $n = 2$, we assumed that the peak heigh of the wrinkle in this case was half of the previous case's height, *i.e.* $y_0/4$. Then, energy accumulated in this case is derived by the following equation (note that $\theta_2(s) = \theta_1(2s)$ as aforementioned):

$$U_{sub}^{n=2} = K_{sub} \int_0^L \frac{1}{2} \left(\frac{1}{2} y_1(2s) - \frac{y_0}{4} \right)^2 cos\theta_1(2s) ds. \tag{3.7}$$

Let $2s = r$, then Eq. (3.7) is re-arranged as:

$$U_{sub}^{n=2} = \left(\frac{1}{2} \right)^2 K_{sub} \int_0^{2L} \frac{1}{2} \left(y_1(r) - \frac{y_0}{2} \right)^2 cos\theta_1(r) \frac{dr}{2}. \tag{3.8}$$

By integrating from $[0, L]$ and $[L, 2L]$, Eq. (3.8) is re-written as

$$U_{sub}^{n=2} = \left(\frac{1}{2} \right)^2 K_{sub} \int_0^L \frac{1}{2} \left(y_1(r) - \frac{y_0}{2} \right)^2 cos\theta_1(r) dr. \tag{3.9}$$

or:

$$U_{sub}^{n=2} = \left(\frac{1}{2} \right)^2 U_{sub}^{n=1}. \tag{3.10}$$

By doing the similar derivation, the generic formulation for estimation of the substrate's energy is followed:

$$U_{sub}^{n=N} = \left(\frac{1}{N} \right)^2 U_{sub}^{n=1}. \tag{3.11}$$

Replacing U^{n}_{flex} and U^{n}_{sub} in Eq. (3.1) by Eq. (3.5) and Eq. (3.11), number of wrinkles N can be calculated based on minimization of total wrinkle energy U as:

$$\frac{dU}{dN} = 2K_{flex}U^{n=1}_{sub}N - 2K_{sub}U^{n=1}_{sub}N^{-3} = 0 \tag{3.12}$$

or:

$$N = \sqrt[4]{\frac{K_{sub}}{K_{flex}}\frac{U^{n=1}_{sub}}{U^{n=1}_{flex}}}. \tag{3.13}$$

As a result, the balance between film's flexural energy and the substrate's energy decides the generated number of wrinkles on the surface. Based on Eq. (3.13), N depends on both mechanical property (ratio K_{sub}/K_{flex}) and geometrical property (ratio $U^{n=1}_{sub}/U^{n=1}_{flex}$), which is similar to derivations in [91]-Eq. (6). Computation of $U^{n=1}_{sub}$ and $U^{n=1}_{flex}$ could be conducted using information of l and L and related work of Wakamatsu and Hirai [92]. Equation (3.13) suggests that with the same geometrical property, number of wrinkles can be varied by selection of appropriate materials of the substrate and thin film.

3.4 Design and Fabrication

Based on the mimicking abstraction and understanding of the wrinkle morphology, we proposed a process for fabrication of a wrinkle-inspired sensorized soft body. The sensing system is a wrinkled sandwich structure: namely a strain gauge embedded in between a soft substrate and a stiffer thin film. When the soft body changes its length, the wrinkle morphology varies, leading to static change of strain gauge output. Meantime strain gauge posture also alters, resulting in different sensitivities to stimuli from different directions.

In order to create the soft wrinkled surface, we glued a stiff, thin film with length $L = 120\,\mathrm{mm}$ onto a pre-stretched relatively thick, soft substrate (the substrate was stretched from original length $l = 100\,\mathrm{mm}$ to $L = 120\,\mathrm{mm}$), then released as illustrated in Fig. 3.5. The reason why we pre-stretched the substrate rather than compressed after attachment of the film is that the compression causes elastic instability, which is common when compressive load is applied to slender object. In this preliminary research, we chose Ecoflex 00-50 (by SmoothOn, USA) for making soft layer, and a Kapton (by Teraoka Seisakusho, Japan) film as the stiff layer. The fabrication process is summarized as follows:

1. First, Ecoflex 00-50 was poured into a mould with basic size of $100\,\mathrm{mm} \times 15\,\mathrm{mm} \times 20\,\mathrm{mm}$. We also designed two pads at two ends for clamping in the experiment afterwards. Then, the mould was put in a vacuum chamber with temperature of $50\,^{o}\mathrm{C}$, and the soft substrate was cured in about 2 hours.

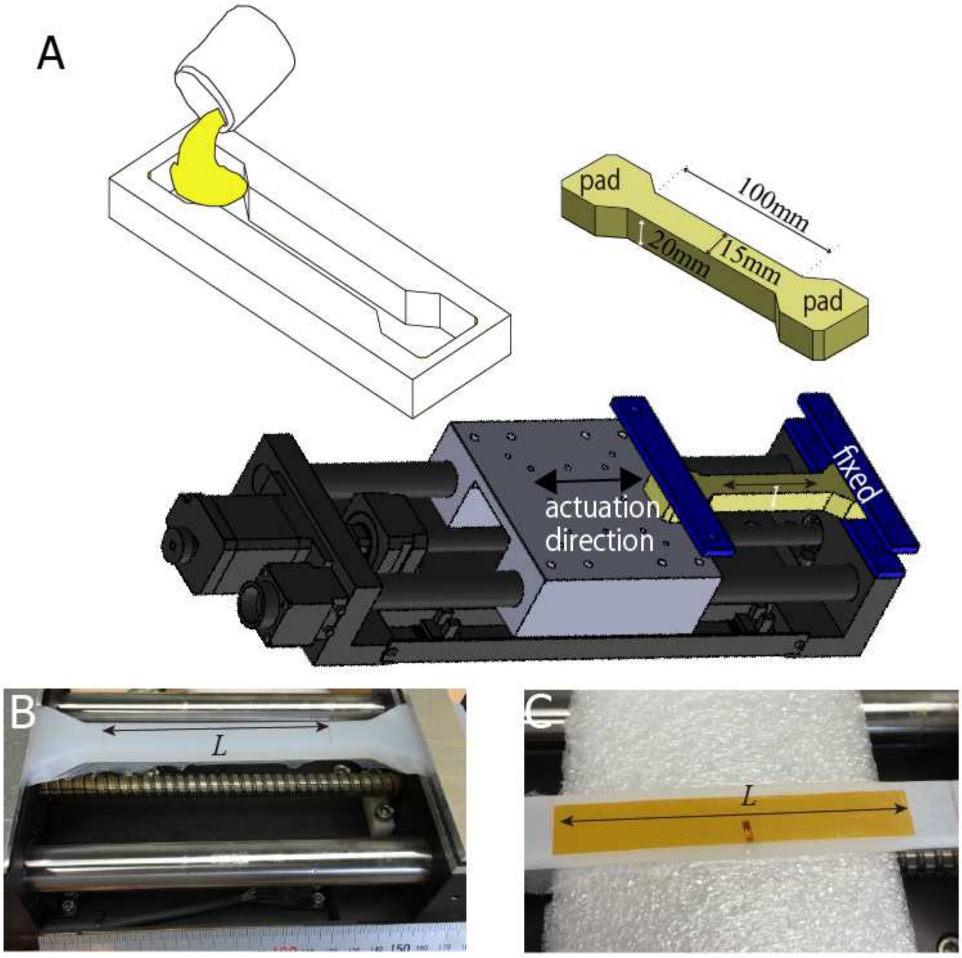

Figure 3.5: The fabrication setup. (a) Ecoflex 00-50 is poured into a mould, vacuumized and cured to form the soft substrate with length l. (b) The substrate is clamped on a motorized linear stage and stretched to length L. (c) A thin film with length L is glued to the substrate.

2. The cured substrate was fixed by two clamps attached on a motorized linear stage whose translational movement could be controlled at resolution of $5\,\mu$m.
3. The substrate was stretched to length $L = 120\,$mm. After this stage, strain gauges were directly attached on the pre-stretched surface of the soft substrate using a silicon-compatible glue (PPX) before attachment of the Kapton film on the entire surface of the substrate using the same glue. After 2 mins when the glue was cured, wrinkle pattern appeared on the surface upon releasing the pre-stretch.

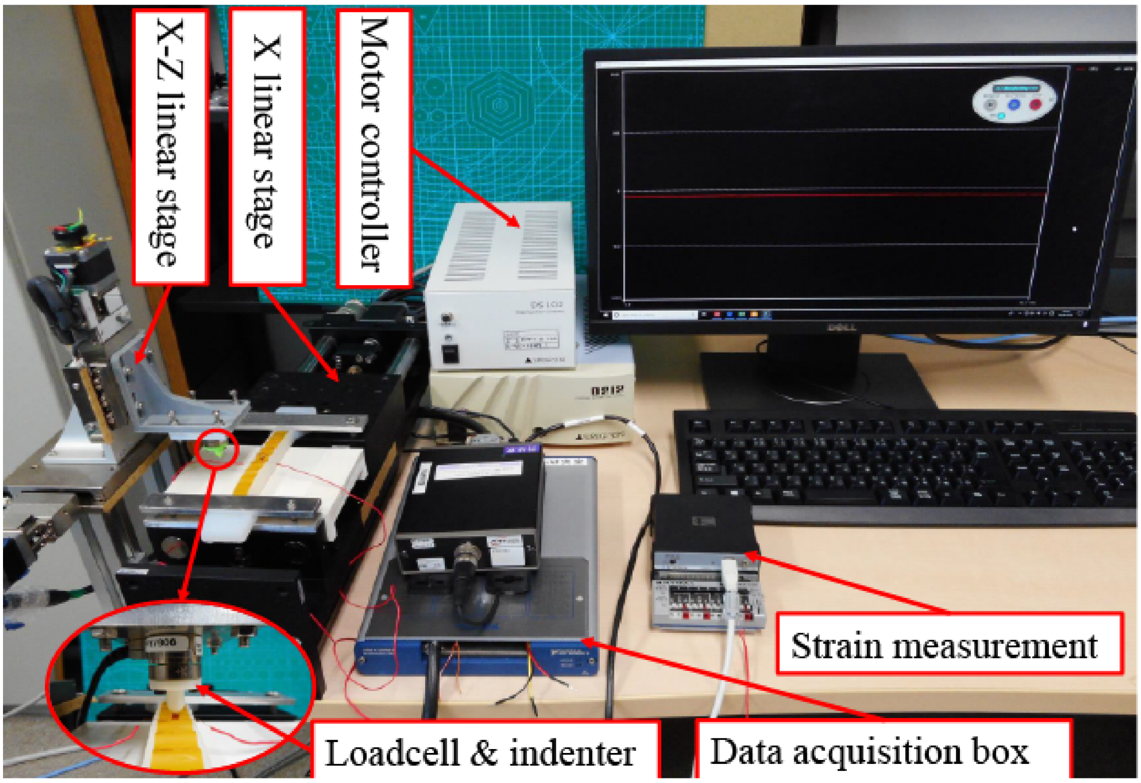

Figure 3.6: The experimental setup for preliminary evaluation: The X linear stage stretches and releases the soft body and X-Z stage performs indention and sliding. A loadcell was installed on the X-Z stage to measure the force and data was transmitted to computer through an ADC data acquisition box. The strain gauge output was measured by a strain measurement device with a built-in Wheaston bridge.

3.5 Experiments and Results

Since both self-deformation and external interaction cause strain gauge output change, it is worthy of verifying this in separate cases. We set up an experiment platform as illustrated in Fig. 3.6 to evaluate the response of wrinkle-based sensing system to self-deformation and interaction test (indention and sliding action). The X linear stage was used to stretch and release the soft body and the X-Z linear stage to drive the indenter for expected motions. The indenter was installed on a loadcell (Nano 17, by ATI Industrial Automation, USA) so as to record the force information which was transmitted to computer through an ADC data acquisition device (NI USB-6343, by National Instrument, USA). The strain gauge output was measured by an integrated strain measurement device with a built-in Wheaston bridge (EDX-10B, EDX15A and UI54A-120, by Kyowa, Japan). This device directly recorded the resistance and strain change.

3.5.1 Self-deformation

As aforementioned, self deformation (*i.e.* not caused by interaction with surroundings) of soft body with wrinkled surface results in change of embedded sensing element (strain gauge) posture. We set up an experiment for evaluation of this conclusion with a moving camera taking consecutive images from side of the wrinkled surface and the strain gauge. The inclined angle information was extracted by image processing techniques with MATLAB. Fig. 3.7(a) shows the processing process of the figures. The original figure was cropped to focus on only the middle wrinkle where the strain gauge is installed. It was then converted into gray-scale intensity image to eliminate the effect of the colour information on the edge detecting. Edge detection with "Sobel" filter was performed to extract the edge information from which the inclined angle information can be derived by calculating the gradient of the wrinkle bump. Fig. 3.7(b) plots the inclined angle information versus the stretching strain. Inclined angle of the embedded strain gauge changes significantly during the elongation, thanks to morphological change of the wrinkled surface. The relationship in between is quite linear, which implies that the sensitive direction of the strain gauge can be varied for better assessing external force from different directions.

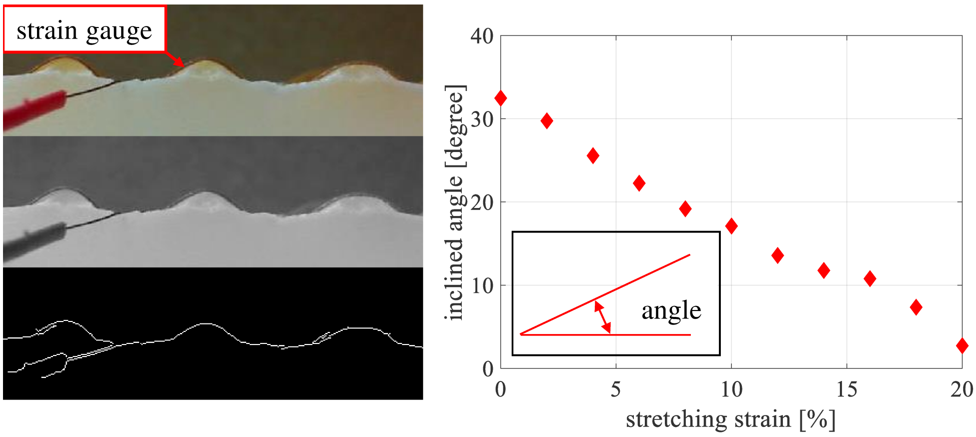

(a) Original and processed images (b) Inclined angles vs. stretching strain

Figure 3.7: Verification of the embedded strain gauge's posture during self-deformation, extracted from consecutive images of the strain gauge: (a) The original, grey-scaled and edged images of the wrinkled soft body. (b) Inclined angles of the strain gauge during self-deformation, implying remarkable change in orientation of the sensing element during morphological change of wrinkles.

We conducted a measurement of the strain gauge output under elongation of the soft body. In this experiment, the soft body was stretched from $l = 100\,\text{mm}$ to $L = 120\,\text{mm}$ then released, and the strain gauge output was recorded meantime using the experiment setup in Fig. 3.6. The driving speed was 3 mm/s and data acquisition frequency was 1kHz. The trial was conducted three times back and forth, and the result average and deviation are plotted in Fig. 3.8(a). Note that the output was presented in the unit of "μm/m" which is an option offered by the strain gauge measuring device to reflect the resistance change of the strain gauge. The relation could be described by the equation "$\varepsilon = \frac{\Delta R/R}{GF}$", where ε is the output in strain, ΔR and R are the resistance change and gauge resistance respectively, and GF stands for the gauge factor specified by vendor. (In this case, $R = 120.4 \pm 0.4\%\,\Omega$, $GF = 2.21 \pm 1\%$.) The output, as can be noticed, increases linearly with the stretching rate and decreases upon releasing. The relatively small hysteresis in between was considered to be due to the viscoelasticity effect of silicone rubber that is typical and readily observable in the constitutional relationship of strain and stress. The variance of the output is quite small demonstrating high repeatability and stability, which makes it possible to discriminate the static response caused by self-deformation from that caused by interactive stimuli.

The stability of the self-deformation output can be further demonstrated by the step response in Fig. 3.8(b), where the dynamic response of the strain gauge under a sudden stretching input was presented. The soft body was stretched at 3 mm/s from $l = 100$ mm to $l = 102$ mm, then released to initial state after 4 secs. In general, the strain gauge responds correspondingly at the same time as the elongation and relaxation starts. After the stretch stopped, the response remains relatively steady around 150 μm/m, which agrees with the result shown in Fig. 3.8(a). The slight decrease at the beginning is considered to be due to the stress relaxation effect in that viscoelastic material presents stress decrease when kept in a constant strained position. Consequently, as investigated, the inclined angle of the strain gauge and the response to self-deformation change linearly upon varying morphology of the wrinkled soft body, through which each can be readily mapped from insight of the other.

3.5.2 Interaction

As mentioned in the previous section, the inclined angle of the strain gauge can be varied by adjusting the morphology of the wrinkle. It was assumed that the strain gauge would be sensitive to external stimuli perpendicular to its surface, which makes it possible to actively change its sensitive surface according to stimuli from various directions in order to achieve higher, or lower where it is preferred, sensitivity. In this experiment, we attempted to evaluate responses of the sensor during variation of wrinkle morphology under two common interactive tasks, normal indention and tangential traction/sliding using the setup shown in Fig. 3.6. A hemispherical indenter attached to a 6-dof (degrees of freedom) loadcell is mounted on a 2-dof motorized linear stage that provides precise movement

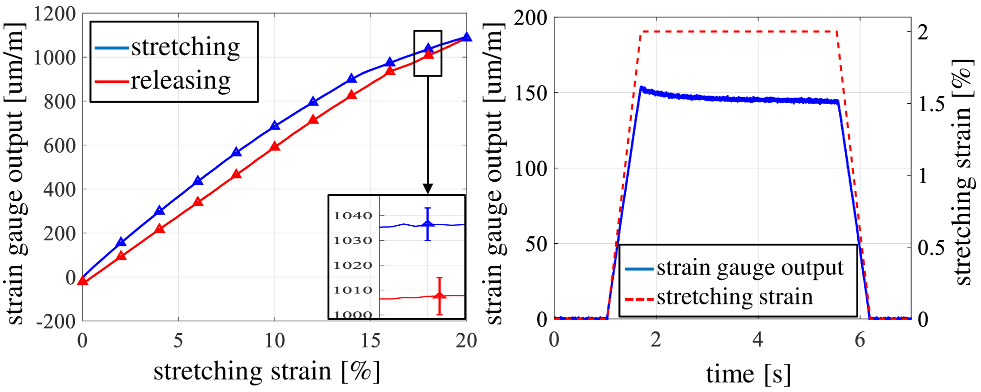

(a) Sensor output under self-deformation (b) Sensor output under step stretching

Figure 3.8: Strain gauge output in form of strain [μm/m]. (a) Under self-deformation (stretching and releasing) condition. It shows approximately linear relation with stretching strain of the substrate. The output hysteresis is considered to be due to the viscoelasticity of silicone rubber. Inset graph shows enlarged view of data mean and standard deviation. (b) Under step stretching (up to 2%) and releasing condition. The response is rather timely and steady even though there is a gradual output decreasing because of the stress relaxation behaviour viscoelastic material.

(with resolution of 2 μm) in both vertical (z-axis) and horizontal (x-axis) directions. The loadcell is used to monitor the actual contact force and moment generated.

Normal Indention

In this experiment, the soft body was stretched from $l = 100\,\text{mm}$ to $L = 120\,\text{mm}$ by 10 steps and at each step, vertical indention of 1 N was applied. The detailed process is as followed: (a) Stretch the soft body by 2 mm with X linear stage; (b) Apply vertical indention (1 N) at the top of the wrinkle bump where the strain gauge is located, then remove the indenter; (c) Repeat steps (a)-(b) 10 times. The strain gauge output was recorded before starting (a) and was presented in Fig. 3.9(a).

As clearly illustrated, both stretching and indention contribute to the sensor output. Each stretching prior to indenting causes increased response from previous state. The stretching response remains steady when no further stretching is applied, and returns to same level when indenter is removed, even though stress relaxation induced output drop remains here but negligible. This agrees with previous result in Fig. 3.8. The indention induces dynamic response, which peaks when reaching the maximum force, on the basis of stretching response. The sensitivity to indention can be evaluated by examining the peak values after subtracting the static stretching response. As observed, the sensor presents various sensitivities to indention of same force, where sensitivities at steps 6, 7 and 8 are much greater than the others thanks to the combined effect of both the strain gauge inclined angle and stiffness change of substrate. The stiffness increases upon stretching thus provides larger resistance to external stimuli. Note that the stiffness is different from elastic modulus that is an intrinsic property of a material whereas stiffness is generally referred as the resistive ability of a structure to external stimuli. Change of the structure may introduce variance of the stiffness.

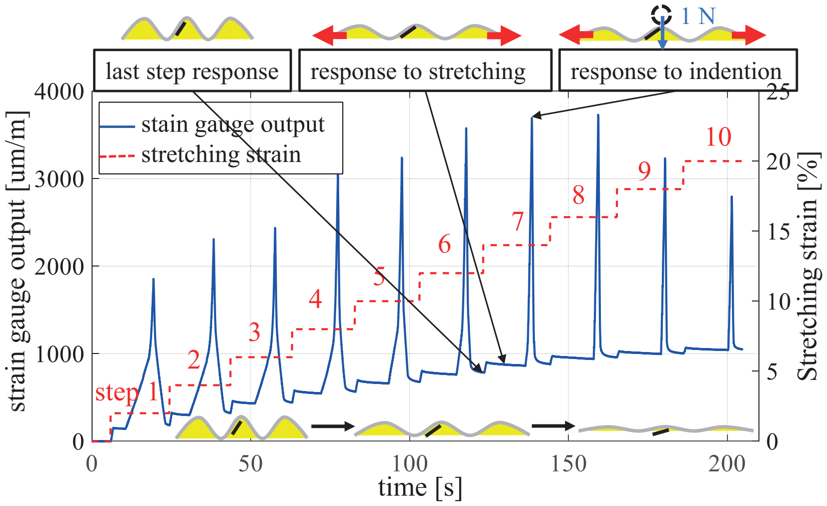

(a) Normal indention under step stretching input (low steps relate to bigger wrinkles)

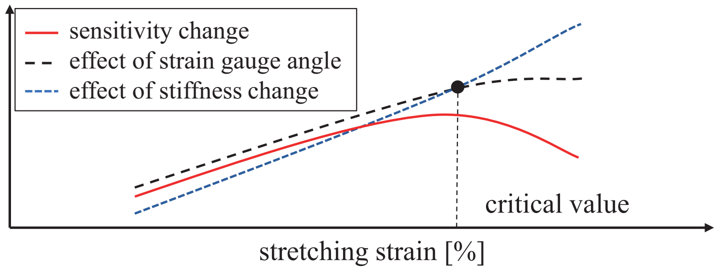

(b) Illustration of two trade-off influence factors on sensitivity variance

Figure 3.9: (a) Normal indention (1 N) test under step stretching input. Response consists of two parts, stretching and indention. Static response to each step stretching agrees with previous section and that to indention can measure the sensitivity to normal indention, where steps 6, 7 and 8 show larger sensitivity than the rest. (b) Illustration of two trade-off factors on sensitivity variance. The effect of stain gauge (positive) is dominant in small stretching strain while stiffness change effect (negative) is in charge after a critical stretching strain.

Fig. 3.9(b) illustrates the trade-off relation between effect of two factors, strain gauge angle and stiffness change, on the sensitivity variance. The angle change tends to increase the sensitivity since that the strain gauge becomes vertical to the indenter. While the stiffness affects the sensitivity negatively because the stiffer the sensor is, the smaller deformation the soft sensor needs to generate in response to same indention. When the stretching strain is small, the positive effect of the strain gauge posture is dominant, thus the overall sensitivity increases upon stretching. The negative effect of stiffness change increases with stretching and at some critical stretching strain (14% in our case) it becomes large enough to balance off the strain gauge angle effect. From here after, the negative effect takes the charge and results in decreased sensitivity.

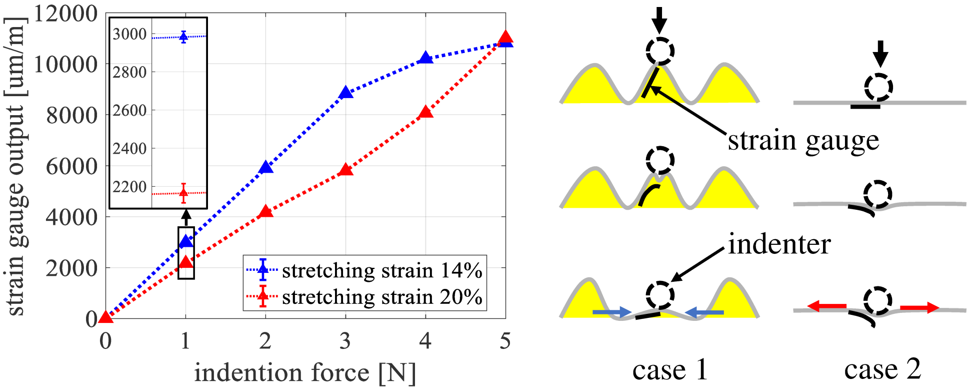

(a) Normal indention of various forces (b) Illustration of normal indention

Figure 3.10: (a) Normal indention test with various forces at two stretching strains, case 1 with 14% and case 2 with 20%. Case 1 performs better sensitively than case 2 at lower forces. Inset graph shows enlarged view of data mean and standard deviation. (b) Illustration of normal indention in two cases. When larger force is applied, Case 1 undergoes a combination of indention and constraint from both sides while case 2 is subjected to combination of stretching and indention.

We performed normal indention test with multiple larger forces for the same sensor in two different stretching rates, namely 14% (with best sensitivity verified earlier, referred as "case 1") and 20% (maximum rate when no wrinkle formed, referred as "case 2") in order to find out how the soft sensor would response to different indention forces. Indention with forces from 1 N to 5 N was performed for the two cases and each was repeated for 5 times. The sensor output at each peak force was recorded, averaged and plotted in Fig. 3.10(a). Note that the static stretching response has been eliminated so as to better evaluate the reaction to indention. As can be seen, case 1 performs better sensitivity and linearity dominantly at lower force range (below 4 N) as expected. Case 2 is likely to outperform case 1 if larger force applied considering the trend of two curves. This can be understood by considering the typical indention processes in two cases illustrated in Fig. 3.10(b). When lower force applied, strain gauge in case 1 undergoes indention induced bending , which causes positive output, and tiny constraints from both sides, which causes contraction to strain gauge leading to negative feedback (compressive stress). However, it can be neglected due to its tiny effect. In contrast, case 2 is subjected to indention and tiny stretching effect, which causes positive feedback (tensile stress), thanks to its stiffness. In this stage, case 1 outperforms case 2 with respect to sensitivity and linearity. When larger force applied, the compressive stress in case 1 and tensile stress in case 2 can no more be ignored, thus case 2 has a trend to outperform case 1.

Tangential Sliding Action

In this experiment, we clarified the dependence of the strain gauge output on wrinkle's morphology under sliding action. In each trial, the hemispherical probe was controlled by the linear stage to traverse over two wrinkles, including the wrinkle where strain gauge was located (referred as "wrinkle 2") and the one in front (referred as "wrinkle 1"), forward and backward for three times. The probe had been adjusted to make contact with the surface at roughly 0.1 N before the sliding action started. Fig. 3.11(a) shows the responses of the soft sensor in different stretching rates, 10%, 14% and 20%, which stand for cases of high wrinkle, low winkle and no wrinkle respectively.

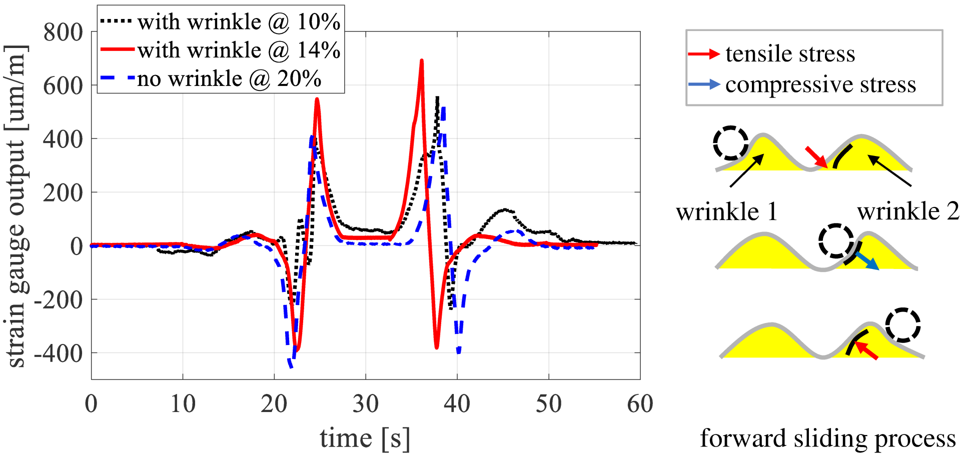

(a) Sliding feedback with different wrinkle state (b) Sliding mechanism

Figure 3.11: Response of soft sensor to forward and backward sliding. (a) The response of sensor with various state of wrinkle is different, where wrinkle with stretching rate at 14% outperforms the others. (b) Illustration of a typical forward sliding mechanism.

We first examine the typical response to a back-and-forth sliding action, as shown in Fig. 3.11(a). The underlying mechanism is as Fig. 3.11(b), characterizing the process qualitatively rather than quantitatively since that the sensor interacts with the probe in a complex manner during sliding, making it hard to formalize a genetic way to describe quantitatively. Generally, when sliding over wrinkle 1, the soft body is compacted by the probe and the stiff film tends to move rightward to compress the bottom end of wrinkle 2. Since there is no constraint on wrinkle 2, the compressing causes elongation and bending of strain gauge as shown, resulting in tensile stress. This explains the first small bump in the response curve. When on the uphill of wrinkle 2, the probe deforms the strain gauge and causes compressive stress. When it slips over the top of wrinkle 2, the wrinkle inside causes tensile force as illustrated. The backward process is quite symmetric to the counter process but with a higher peak thanks to different directions of friction in between the contact. The sensor output generally follows this output pattern when low or no wrinkle formed, while fluctuates for high wrinkle case because of the large non-linear deformation. Additionally, the low wrinkle case performs better than when there is no wrinkles with respect to sensitivity, as observed in the indention case as well. However, the high wrinkle case does not perform better. In this case, the soft body is said to be sensitive to not only the sliding distance since it can capture the number of wrinkles it passes over, but also the direction considering the symmetric response pattern it generates.

From the qualitative description of the sliding process where the dedicated contact in between the probe and soft sensor is vital, we assumed that shape of the probe might be a factor affecting the output. We then investigated the sliding response to probes of different shapes by repeating the sliding test with three different shapes of probe, namely spherical, flat and cone, for the low wrinkle case. Note that only forward sliding was performed due to the fact that symmetric response would not provide more information than merely one-way sliding. Thirty times each were performed. The responses were plotted in Fig. 3.12(a). Note that data for each shape have been shifted 15s for clearer presentation. The spherical and cone probes perform quite similar in term of time span with that of the cone probe being slightly shorter due to the smaller contact area. Besides, the spherical probe responses have negative peaks with larger absolute values. Compared to these two cases, time span of flat probe responses are larger thanks to its larger contact surface, and it gives more stable responses when sliding over wrinkle 1. We avoid to analyze the underlying mechanics for such differences because of the complexity of the sliding process discussed earlier, but one can do the same as how we did the qualitative explanation earlier.

We considered these differences would benefit the task of discriminating various shapes, which can be observed from Fig. 3.12(b) presenting simply mean and standard deviation of each trial. We then investigated this possibility by implementing a machine learning task to classify different probe shapes. For all the three probes, we performed the forward sliding for 30 times in each of two cases, low wrinkle and no wrinkle, and collected all the data for implementation in MATLAB. In total, for each case, there were 90 observations with 30 for each probe. We abstracted the mean and standard deviation of each observation as the input augments to train and validate the classifiers. In order to demonstrate the intrinsic advantages of this sensor in such task, we selected three common machine learning classifiers including Decision Tree (DC), K-Nearest Neighbours (KNN) and Support Vector Machine with Gaussian kernel (Gaussian SVM). Considering relatively small dataset size, the statistical method of 10-Fold Cross-Validation was applied, in that the following steps are executed: (1) Divide dataset into 10 subsets randomly and equally, (2) Select 1 subset as the testing set and remaining as training set, (3) Perform classification trial, (4) Repeat (2)-(3) by selecting 1 subset other than previous one until each subset has been used as testing set for once, (5) Average the results from 10 trails. The classification accuracy for both cases was listed in Table 3.1. As presented, the wrinkled case outperforms the counterpart for all the three classifiers and each classifier takes less than 1 second to train and validate.

Table 3.1: Shape Classification Results

Cases	**DC**	**KNN**	**Gaussian SVM**
With wrinkle	99.2%	100%	100%
Without wrinkle	97.8%	97.8%	94.2%

3.6 Discussion

The soft sensor was demonstrated preliminarily to possess multiple sensibilities to both normal indention and tangential sliding interaction and among these multiple options preferred sensibility can be switched by simply stretching and releasing the soft sensor for different sensing tasks. This property enable the future implementation of active tactile sensing system. In this sense, a thoroughly trained *brain* that actually decides which wrinkle morphology optimally suit for specific sensing task is required. Dataset for training would be strain gauge response under different postures of itself, morphologies of the soft body, and diverse interaction conditions with surroundings. Both time-domain and frequency-domain data obtained from the strain gauge would be taken into account for best inclusion of static and dynamic properties in self deformation and interaction of the sensorized soft body.

Proper actuation need to be integrated to accomplish the sensor and actuary combination. One promising method is to integrate this sensing system as a skin covering a robotic fingertip which is driven by servo motor and twisted string [93]. By rotating the servo motor, twisted string is able to pull or release the skin resulting in variation of the morphology of the wrinkle.

One limitation with the sensor is to differentiate the sensor signal resulted by self-state change and by external stimuli. For example, when both stimuli happen at the same time, the single sensing element might not be able to tell the difference. This concern need to be solved before it can actually be implemented in real application, such as the active sensing system in the future.

3.7 Conclusion

This paper introduced the idea of VANmorph and presented an implementation prototype inspired by water-induced wrinkle morphology. The fabrication of wrinkle pattern was analysed based on an analytical model to show the repeatability and controllability of the fabrication process. For thorough evaluation of the model, both actual fabrication with various material combination and Finite Element Analysis simulation using ABAQUS are scheduled for next stage research.

This proposal of wrinkle-based sensing system is our first step toward different robotic applications. Thanks to introduction of the wrinkle morphology, the sensor can capture both the location of the contact and shape of probe during sliding, which makes it possible for such applications as contact localization and texture discrimination coupled with machine learning techniques. More evaluation on such property will be conducted in future research.

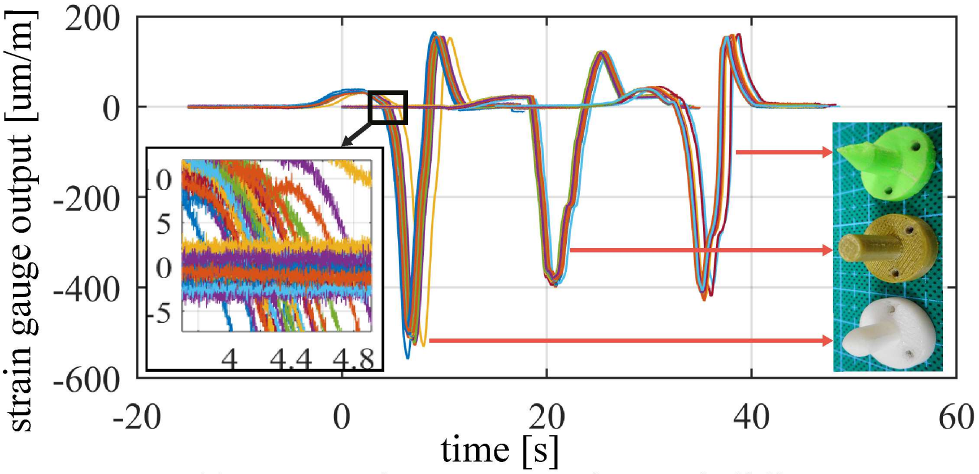

(a) Repeated response to forward sliding

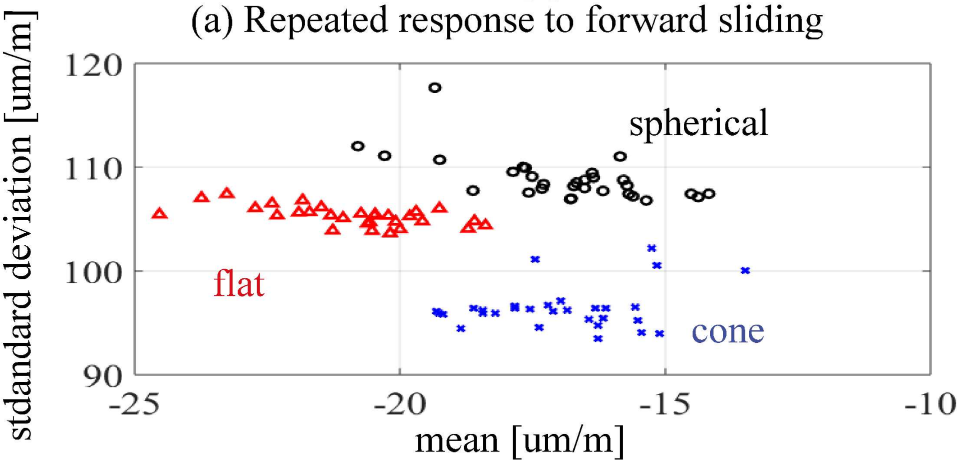

(b) Mean and standarad deviation of trials

Figure 3.12: (a) Repeated response to forward sliding with different shapes of probe in the case with wrinkle (30 times each). The spherical and cone probes are similar in term of time spanning while the former has a negative peak with larger absolute value. The time span of flat probe response is larger than the others thanks to its larger contact surface, and it gives a more stable response when sliding over the wrinkle 1. (b) Mean and standard deviation of each trial. It gives a glimpse that how distinguishable each shape is.

Chapter 4

Adaptive Morphology Facilitating Sensing : WrinTac Based on Bending Actuation

Abstract

Based on the same prototype, “WrinTac”, this chapter proposes another actuation approach for the soft sensor. The design was slightly modified to better fit such actuation. When bended, the sensor exhibits a series of morphological variations which are further investigated in terms of the function-morphology relation. It was further tested in two tasks, shape classification and texture detection, and found that, for each different task, there is always an optimal morphology that optimizes perceptual performance. It sheds light to novel active sensing system design in that the “active” part can be achieved by varying the sensor morphology, which conventionally was always exploited from the sensory motor coordination aspect.

4.1 Introduction

Sensor morphology has been recognized as a source of “intelligence” in that it shapes the external stimuli to usable afferent signal and that variation of it results in different perceivable signal [13, 16]. This interdependent relationship of morphology and function has inspired researches investigating how particular sensor morphology influences the sensing property and perception performance. Two popular tactile morphological structures in this regard are whiskers [94–96] and wrinkles (or fingerprints) [56–58, 97, 98], where both

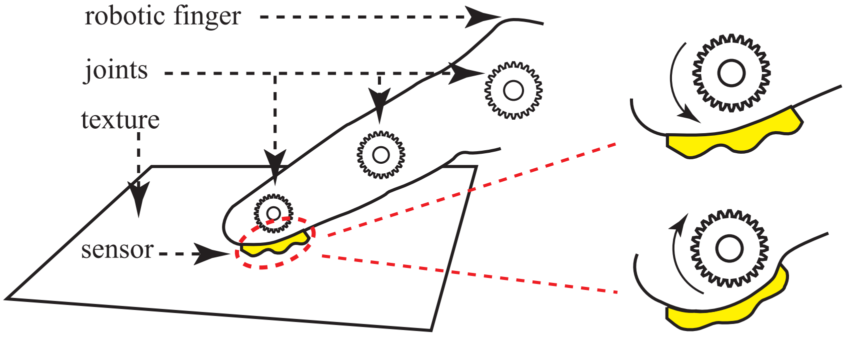

(A) Scenario of texture palpation using robotic finger equipped with wrinkled sensor (B) Morphological variation of sensor by joint rotation

Figure 4.1: (A) An envisioned future application scenario: texture exploration with the wrinkled tactile sensor on a robotic finger. (B) The morphological variation of wrinkles is actuated by joint rotation mimicking joint movement of human fingers. When it rotates clockwise, the sensor is bent thus wrinkle magnitude shorten, wavelength prolonged, overall stiffness increased. All contribute to variation of sensor property, offering the chance to optimize perception by adapting sensor morphology.

morphologies were found effective tuning sensor performance in tasks such as force sensing, obstacle avoidance and texture detection. These findings are particularly important in active tactile sensing systems where agents, in order to get better perception, purposefully adapt either the sensor morphological state or the sensorimotor control strategy to specific tasks [99].

While most previous researches focused on changing control algorithm, this research attempts to answer whether it is possible to realize active tactile sensing by adapting tactile sensor morphology. This was done by testings on a wrinkled tactile sensor with changeable morphology in three common tactile sensing tasks, including force sensing, shape discrimination and texture detection. It was found that, for each task, the sensor presented an uniquely optimal morphology elicited by its bending state. This finding offer an opportunity to adapt morphology to different tasks if the morphology-function relationship is known, enabling novel active sensing mechanism, thus contributing to the field.

4.2 Related Works

4.2.1 Active tactile sensing

Human master active touch sensing in that they change sensing strategy to best fulfill perception tasks. Consider the process we stroke a surface with fine but detectable texture for texture detection, as illustrated in Fig. 4.2. We first lean the finger slightly against the surface, and slide forth and back to feel the roughness with the contact force monitored. Within an initial force range, the magnitude of contact force determines the sensing performance. The higher the force is, the clearer we can feel the texture. The process here is active in two perspectives. One is the sensorimotor control strategy, the other the morphological change of finger that is not commonly aware of. In term of this aspect there is a series of changes as illustrated in Fig. 4.2 (B): upon pressing harder, the soft skin complies more closely with texture details, and the tissue in between the surface and underlying mechanoreceptors becomes locally thinner, denser and stiffer, thus facilitating vibration detection [17]. While the perception of fine texture mainly relies on vibration sensed by Pacinian Corpuscles [100], the morphological variation here is key for this purposive palpation [101]. An artificial active sensing system by Nurzaman *et al.* [59] was capable of detecting different physical quantity, *i.e.* softness and temperature, by varying the sensor morphology. The sensing probe, made of Hot Melt Adhesive (HMA) was fabricated, extended for sensing, melted and then re-fabricated to update its morphology for a different sensing task.

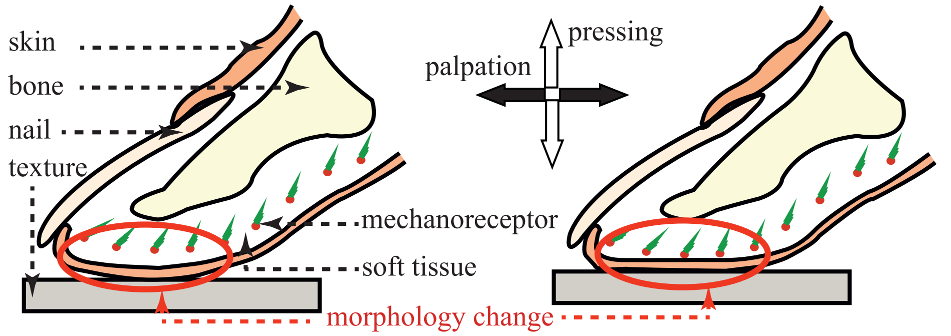

(A) Palpation with slight pressing force (B) Palpation with larger pressing force

Figure 4.2: Illustration of scenario when human stroke with finger a surface of fine while detectable texture. (A) Palpation with slight pressing force. (B) Palpation with larger force. As observed, upon pressing harder, the soft tissue between textures and mechanoreceptors becomes locally thinner, denser and stiffer, benefiting vibration detection.

4.2.2 Biomimetic researches of fingerprints on tactile sensor

Biomimetic tactile sensors with wrinkles mimicking fingerprints structure have been developed to investigate the enhancement effect of tactile sensing. Scheibert *et al.* demonstrated the spectral selection and amplification of tactile information [97]. Oddo *et al.* found that curvature of fingerprints can enhance the directional isotropy in detecting tactile stimuli with structural anisotropy [56]. Vasaarhelyi *et al.* aimed to increase sensitivity of tactile sensing by adding elastic cover on taxel sensor [57], and Yamada *et al.* utilized skin ridges for grasping force control [58].

4.2.3 Texture and shape detection with tactile sensation

Texture and shape detection are two common areas where tactile sensing dominates especially when vision is constrained [102]. Considering the complex contact situation that makes it impossible for precise modeling, learning methods based on large data set are common approaches to discriminate different textures and shapes [103, 104]. Several learning algorithms are clustering (K Nearest Neighbour), Bayesian-based (Naive Bayesian), and tree-based (Decision Tree) classifiers. While common machine learning methods highly rely on domain expertise for feature representation, Artificial Neural Networks, especially Convolutional Neural Networks (CNN) has been popular recently as it extracts feature within the algorithm itself [105].

4.2.4 Comparison with previous design

The present study was motivated by a wrinkled tactile sensor design previously proposed by Qi *et al.* [2]. There are important differences in order to make the sensor more compact as this design was expected for a future application on robotic finger as envisioned in Fig. 4.1. In detail, previous dimension was $l = 100\,\mathrm{mm}$, $w = 15\,\mathrm{mm}$, $h = 20\,\mathrm{mm}$ while present is $l = 100\,\mathrm{mm}$, $w = 10\,\mathrm{mm}$, $h = 8\,\mathrm{mm}$. The substrate material has been modified from Ecoflex-0050 (Shore Hardness 00-50, 100% Linearized Tensile Modulus 82.74 kPa) to Ecoflex-0020 (Shore Hardness 00-20, 100% Linearized Tensile Modulus 55.16 kPa) that is much softer. Apart from the top film, another tape was attached to the bottom for easy integration in experimental platform. Most importantly, the previous design was based on stretching actuation while the present design on bending actuation.

4.3 Fabrication, Characterization and Finite Element Modeling

4.3.1 Fabrication

The fabrication process was initially detailed in [2] and summarized here along with modifications that have been made to suit for bending actuation. As illustrated in Fig. 4.3, Ecoflex00-20 (Smooth-On, USA) was thoroughly mixed with the weight ratio of Part A:B being 1:1, modeled into rectangular shape ($l = 100\,\mathrm{mm}$, $w = 10\,\mathrm{mm}$, $h = 8\,\mathrm{mm}$) with a 3D printed mold, then degassed and cured in an oven. The cured soft material was pre-stretched from original length to $l = 120\,\mathrm{mm}$ before a commercially available strain gauge and stiffer kapton tape were attached to the top surface in sequence using silicon-compatible glue (PPX). Wrinkle structure formed automatically upon releasing the pre-stretching. Another tape was then attached to the bottom.

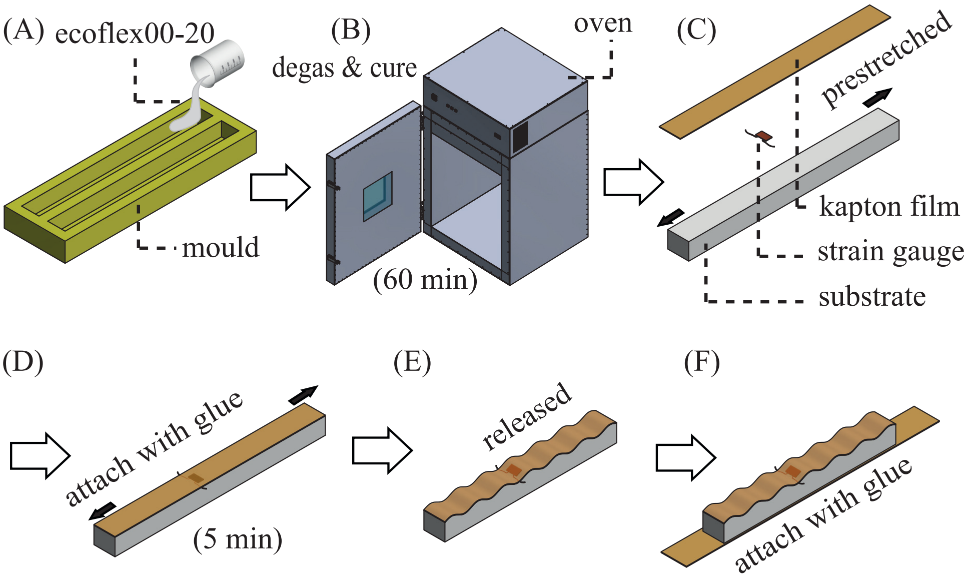

Figure 4.3: Sensor fabrication process. (A) Ecoflex00-20 was mixed with the weight ratio of Part A:B being 1:1, then poured into a 3D printed mold. (B) The whole model was degassed and cured at room temperature in a vacuum oven. (C) The sensing element and kapton tape were attached in sequence to the pre-stretched substrate. (D) After 5 minutes for glue drying, the pre-stretch was released. (E) Wrinkle structure formed on top with sensing element located at one wrinkle bump. (F) Another tape was attached to the bottom for easy integration into experimental platform.

4.3.2 Geometrical characterization of wrinkle structure

The morphological variation of the proposed sensor will be provided by bending actuation, which is a mimicking abstraction of bending behavior of human finger. It is then worthy of modeling how the wrinkle structure changes upon bending in order to characterize this structure. Symbols used for modeling are listed in Table 4.1. In addition, following assumptions are made:

- Wrinkles over whole structure are identical. The bending is circular and uniform, thus $\theta = N * \theta'$, $L = N * L'$, $l = N * l'$ and $l_w = N * l'_w$.
- Thickness (t) remains constant during bending.

- As in Fig. 4.4, the wrinkles are sinusoidal and the basic features of each can be approximated by that of the isosceles triangle, namely, $\alpha = \alpha'$, $l' = l_{tb}$ and $l'_w = l_{ts}$.

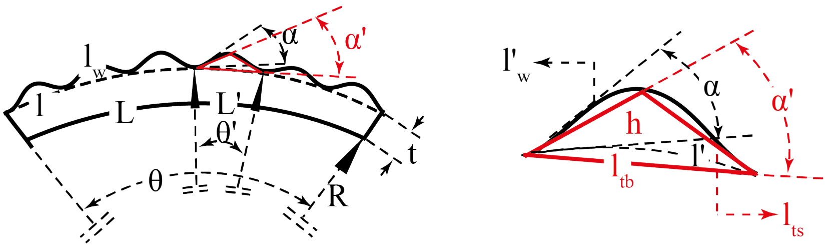

Figure 4.4: Geometrical modeling of sensor, where geometrical property of wrinkle structure can be approximated by that of the characterization triangle marked in red. Symbols and definitions are listed in Table 4.1.

At the beginning, wrinkle number N, wrinkle height h and length of sensor bottom line L are determined by fabrication, thus known at initial state when no bending happens. Moreover, N and L remain constant since the kapton tape is inextensible whereas h varies during bending. As assumed, basic features of wrinkle wave can be approximated by that of the isosceles triangle, following relationship holds based on Pythagoras' Theorem,

$$l_{ts} = \sqrt{h_{ini}^2 + (\frac{l_{tb}}{2})^2} \tag{4.1}$$

Bending platform in here was design as circular, where the radius R and bending angle θ change while perimeter L remain constant, thus, $L = R * \theta$ and $l = (R + t) * \theta$. According to Cosine Formula,

$$l_{ts}^2 + l_{tb}^2 - 2 l_{ts} l_{tb} \cos(\alpha') = l_{ts}^2 \tag{4.2}$$

Therefore, geometrical structure of wrinkle can be determined by following equations, which are derived by solving assumptions equations, Eq. 4.1 and Eq. 4.2,

$$\begin{cases} l' = \frac{(L+\theta t)}{N} \\ h = \sqrt{h_{ini}^2 - \frac{L\theta t}{2N^2} - \frac{\theta^2 t^2}{4N^2}} \\ \alpha = \arccos(\frac{L+\theta t}{\sqrt{4N^2 h_{ini}^2 + L^2}}) \end{cases} \tag{4.3}$$

that indicate bending actuation θ can directly vary wrinkle's geometrical morphology. Upon bending increases, l' increases, h and α decrease, and vice versa.

4.3.3 Finite element modeling

In here, the wrinkling and bending behavior of the sensor were simulated and analyzed with the commercial software ABAQUS. As can be readily and intuitively inferred, the proposed sensor design was symmetrical w.r.t x-axis and z-axis. Therefore, all simulations here were simplified to two-dimensional (2D) analysis with in xy-plane.

Table 4.1: Nomenclatures (refer to fig. 4.4)

Symbols	**Definitions**
N	Number of wrinkles over structure (constant)
L	Length of bottom line/arc over wrinkles (constant)
L'	Length of bottom line/arc over one wrinkle
l	Length of arc tangential to valleys over whole structure
l'	Length of arc tangential to valleys over one wrinkle
l_{tb}	Length of bottom side of approximation isosceles triangle
l_{ts}	Length of equal sides of approximation isosceles triangle
l_w	Length of sinusoidal wave over wrinkles
l'_w	Length of sinusoidal wave over one wrinkle
t	Thickness between valley and bottom line
h	Amplitude of wrinkle structure at initial state
h_{ini}	Value of h at initial state (known)
θ	Bending angle over wrinkles
θ'	Bending angle over one wrinkle
α	Inclined angle of embedded sensing element
α'	Inclined angle of approximation triangle

Simulation of wrinkling behavior

The wrinkling behavior was modeled as 2-step analysis that simulated the real fabrication process [106]. In the first step, a rectangular substrate of 80 mm long and 8 mm thick was stretched to 120 mm and the stress distribution was recorded over the whole process. A symmetrical Boundary Condition (BC) on left, a planar deformation BC on bottom and a displacement BC on right were constrained. The second step was shown in Fig. 4.5. The deformed geometry together with stress output from last step was imported before the thin film of 120 mm long and 0.2 mm thick was added and tied to the substrate. The BCs are two symmetrical constraint on left surfaces of substrate and film, and a planer deformation constraint on the bottom surface. The imported stress acted as a predefined field. Wrinkle structure appeared when the stress was released, as in Fig. 4.5 (B). Note that colormap in Fig. 4.5 (A) indicated no numerical difference because the pre-stretching was simulated as a static process, causing uniform stress distribution in substrate.

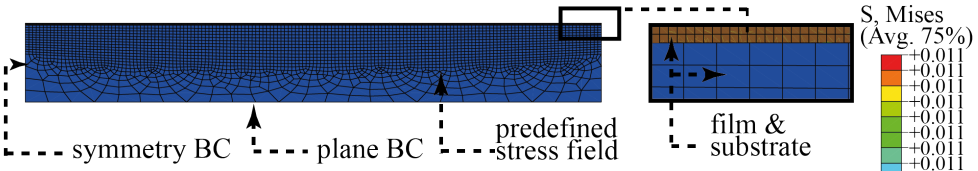
S, Mises
(Avg. 75%)
+0.011
+0.011
+0.011
+0.011
+0.011
+0.011
+0.011
+0.011
+0.011
+0.011
+0.011
+0.011
+0.011
symmetry BC
plane BC
predefined stress field
film & substrate

(A) Initial state of step-2

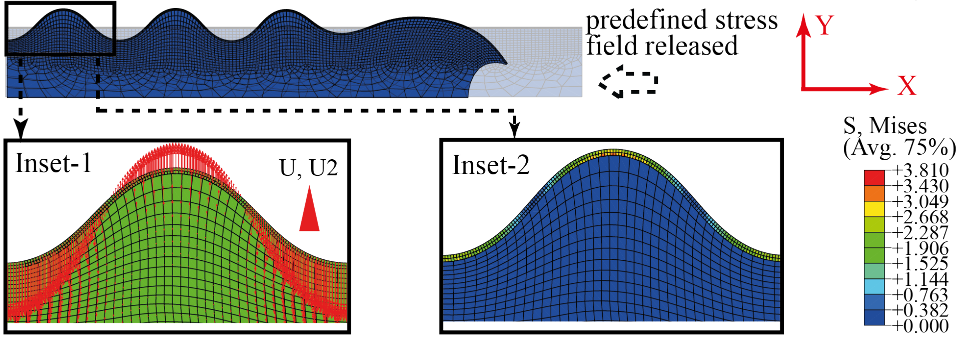
predefined stress field released
Y
X
Inset-1
U, U2
Inset-2
S, Mises
(Avg. 75%)
+3.810
+3.430
+3.049
+2.668
+2.287
+1.906
+1.525
+1.144
+0.763
+0.382
+0.000

(B) Release of pre-stretching

Figure 4.5: The wrinkling process of proposed sensor in Finite Element Modeling. This is a two-step analysis, where step - 1 is the pre-stretching of the substrate and step - 2 includes attachment of film and strain gauge, and release of pre-strteching. It shows merely step - 2 as wrinkle forms in this stage. The stress is expressed in Mpa. (A) Initial state of step - 2 where three boundary conditions were set. (B) Wrinkling process with two insets, one showing node displacement along vertical direction from initial state and the other the stress distribution. It shows that where there is no vertical displacement in Inset - 1, there is minimum stress in Inset - 2.

Simulation of bending behavior

Bending behavior was simulated here to demonstrate that bending actuation can significantly vary the wrinkle structure as shown in Eq. 4.3. In here, the circular bending was introduced by a platform, which is much stiffer than any other part this model, under pure bending moment. Specifically, there were three parts including the deformed film, substrate and bending platform. Similar to last simulation, both substrate and film were imported as orphan mesh with stress field. Three parts were tied together in sequence. Four BCs included symmetrical BC on left of film, substrate and platform, and a moment constraint on the right of platform. Different bending states could be achieved when various moment was applied. Fig. 4.6 shows the geometrical change of wrinkle structure. Note here that each sub-figure was mirrored by y-axis to show the whole structure of the sensor. As can be seen here, the more the sensor is bent, the smaller the wrinkle height and the inclined angle are. This agrees with the trend by Eq. 4.3, indicating that the geometrical model can well predict the bending behavior. The same trend can also be observed in Fig. 4.7 that presents the experimental setup as well as the morphological variation in real experiment.

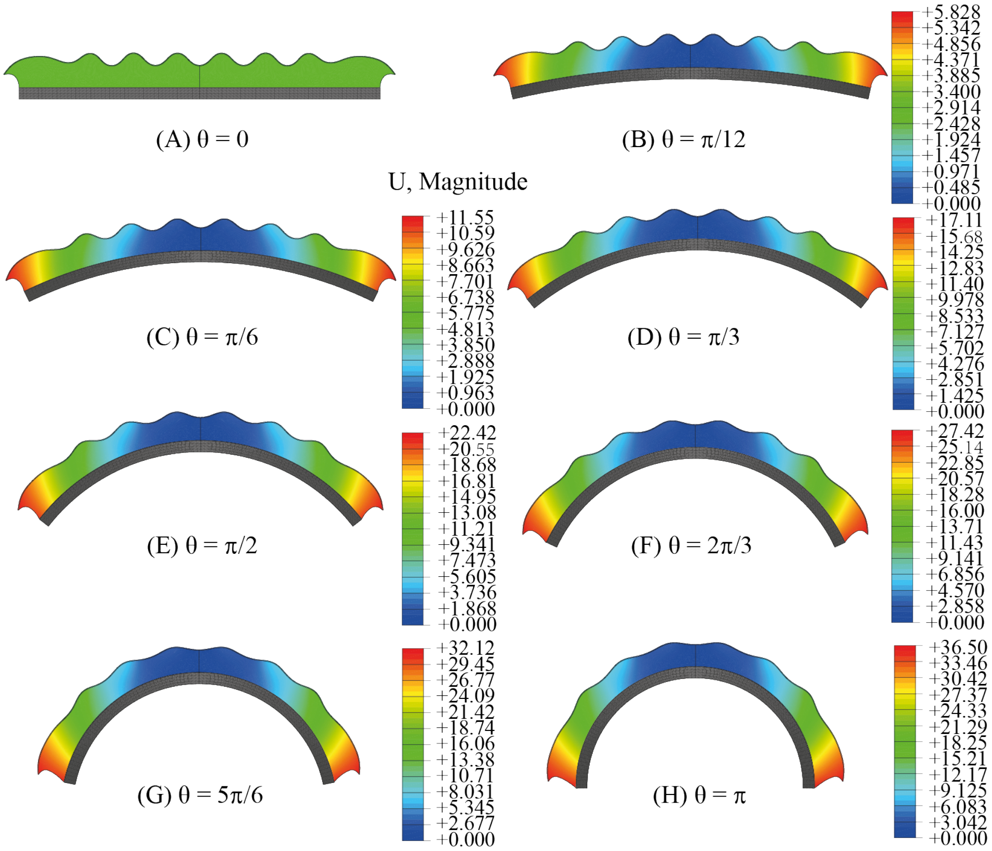
(A) $\theta = 0$ (B) $\theta = \pi/12$ (C) $\theta = \pi/6$ (D) $\theta = \pi/3$ (E) $\theta = \pi/2$ (F) $\theta = 2\pi/3$ (G) $\theta = 5\pi/6$ (H) $\theta = \pi$

U, Magnitude
+5.828
+5.342
+4.856
+4.371
+3.885
+3.400
+2.914
+2.428
+1.924
+1.457
+0.971
+0.485
+0.000
+11.55
+10.59
+9.626
+8.663
+7.701
+6.738
+5.775
+4.813
+3.850
+2.888
+1.925
+0.963
+0.000
+17.11
+15.68
+14.25
+12.83
+11.40
+9.978
+8.533
+7.127
+5.702
+4.276
+2.851
+1.425
+0.000
+22.42
+20.55
+18.68
+16.81
+14.95
+13.08
+11.21
+9.341
+7.473
+5.605
+3.736
+1.868
+0.000
+27.42
+25.14
+22.85
+20.57
+18.28
+16.00
+13.71
+11.43
+9.141
+6.856
+4.570
+2.858
+0.000
+32.12
+29.45
+26.77
+24.09
+21.42
+18.74
+16.06
+13.38
+10.71
+8.031
+5.345
+2.677
+0.000
+36.50
+33.46
+30.42
+27.37
+24.33
+21.29
+18.25
+15.21
+12.17
+9.125
+6.083
+3.042
+0.000

Figure 4.6: Simulation of sensor bending behavior. (A) - (H) Morphological difference when bent by different angles. As observed, the more the bending is, the shorter the wrinkle magnitude and longer the wavelength. Note that the modeling was performed as a symmetric structure while visualized as a whole. The colormap was expressed in mm.

4.4 Experiments and Results

The experiments were inspired by how human use the sense of touch. We press to determine softness, palpate edges to judge shape and stroke a surface to detect texture. As an analogue, three tasks that are normal indention, shape discrimination and texture detection were conducted for the sensor under multiple morphological states.

4.4.1 Normal indention

Setup

As shown in Fig. 4.7, the sensor was attached to a series of platforms with different bending angles. A semi-cylinder indenter was connected with a loadcell (Nano 17, ATI Industrial Automation, USA) to perform indention so that force can be monitored. The horizontal and vertical movement were provided by a X-Z linear stage. Furthermore, for integrated control, a Python script was developed to synchronize motor control, sensor signal reading and force recording. The sensor signal and force data were recorded by an integrated strain measurement device (EDX-10B, EDX15A and UI54A-120, Kyowa, Japan) and a data acquisition device (NI USB-6343, National Instrument, USA), respectively.

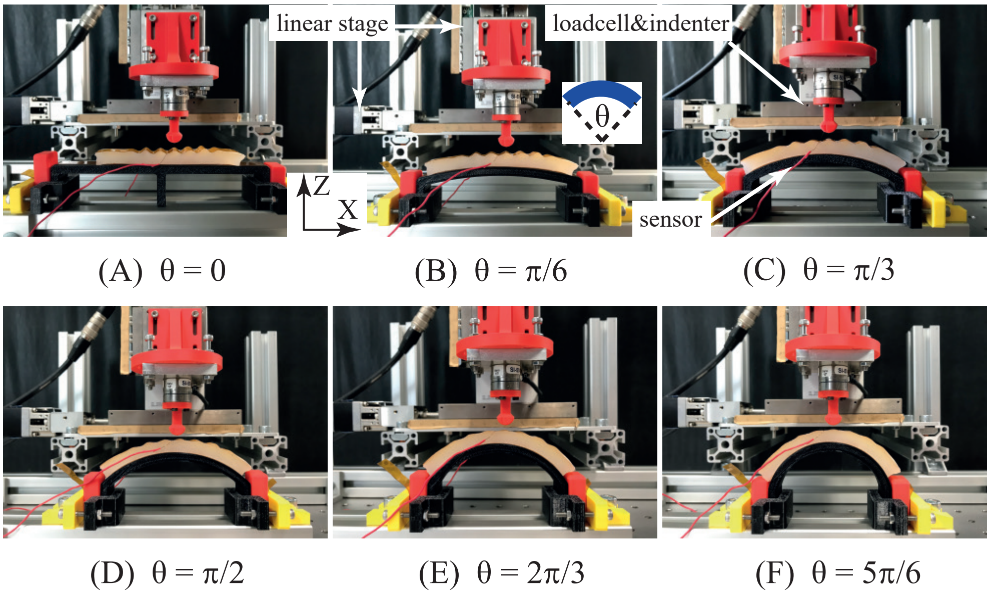

(A) $\theta = 0$ (B) $\theta = \pi/6$ (C) $\theta = \pi/3$

(D) $\theta = \pi/2$ (E) $\theta = 2\pi/3$ (F) $\theta = 5\pi/6$

Figure 4.7: Experimental setup and wrinkle morphological variation under different bending states. (A) - (F) Different bending states showing the same trend of morphology change as in Fig. 4.6. Since the strain gauge was embedded at one side of wrinkle bump, its orientation changes during bending as well. θ indicates the bending angle.

Method

The indention test was performed for every one of the bending states characterized by following angles $[0, \pi/6, \pi/3, \pi/2, 2\pi/3, 5\pi/6, \pi]$. Specifically, at one bending state, the exact wrinkle bump with strain gauge was pressed with force up to each of the values [0.1, 0.2, 0.3, 0.4, 0.5] N. Each indention was repeated 10 times, thus 350 recordings in total were derived from this testing. Note that the force range was selected since larger forces may trigger highly nonlinear contact behavior, same as the reason in [2].

Results

Fig. 4.8 (A) showcases different responding profiles when the sensor was bent by $\pi/3$. Note that curves were shifted 1 second along time for clearer presentation. Inset-1 shows a closeup of the case of 0.1 N, indicating that the sensor reached maximum output in a step manner. The step profile was due to the loading process as shown in supplement video. Further, it demonstrated a good dynamic response as it reacted to the short pause induced by control strategy. Fig. 4.8 (B) plotted the mean and standard deviation of all the data. The sensitivity to normal indention of small force range was tuned by a trade-off effect of two factors that are the inclined angle of strain gauge and the overall stiffness [2]. Here, this effect can be observed when indention force is smaller than 0.3 N. Take loading case of 0.2 N for example, the sensitivity increases from $\theta = 0$ to $\theta = \pi/2$ mainly because of inclined angle change, then decreases from $\theta = 2\pi/3$ to $\theta = \pi$ due to stiffness increase which provides more resistance to normal stimulus. Then, when sensor was exposed to force range larger than 0.3 N, the stiffness change dominantly tuned the sensitivity. This is the reason that sensitivity decreases along the bending extent for loading cases of 0.4 N and 0.5 N. In summary, wrinkle morphological variation introduces orientation and stiffness changes thus varying sensitivity to normal stimuli.

4.4.2 Shape discrimination

Setup

The same equipment setup as the indention test was adopted, except that three indenters of different shapes was used here. The three shapes are semi-cylinder referred as “C”, wedge as “W” and square as “S”, as shown in Fig. 4.10 (B).

Method

Each indenter was controlled to slide over the wrinkle with strain gauge such that the maximum vertical force was 0.1 N. In detail, the procedures are as followed (a) The indenter was pressed down to the wrinkle until force threshold. (b) Slide leftward horizontally for 5 mm to the initial place starting from where the data was to be recorded. (c) Slided the indenter rightward for 10 mm at one of preset speeds [2, 4, 6, 8, 10] mm/s, meantime

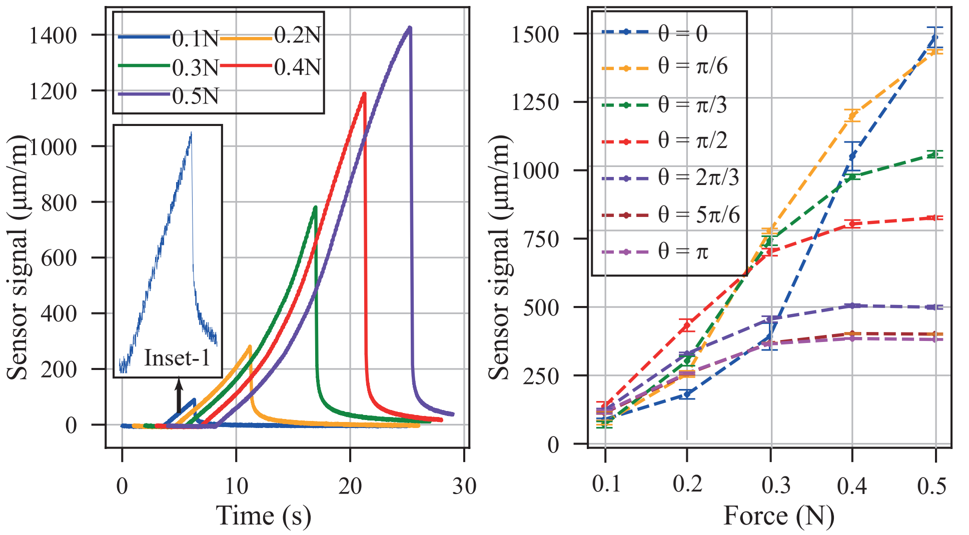

(A) Indention loading curves when under bended by θ = π/3

(B) Sensor signal to indention under all bending angles

Figure 4.8: (A) The loading cases while sensor was bent by θ=$\pi/3$. The sensor was pressed up to a normal force threshold while reading recorded. The same pressing was repeated for each of [0.1, 0.2, 0.3, 0.4, 0.5] N. Inset - 1 is a closeup showing step response manner. (B) The response profiles to a series of normal forces as in (A) when sensor is under various bending angles [0, $\pi/6$, $\pi4/3$, $\pi/2$, $2\pi/3$, $5\pi/6$, π]. The sensitivity to stimuli under 0.3 N was affected by a combination of two factors that are the inclined angle of strain gauge and the overall stiffness, as verified in [2]. While sensitivity to larger force was dominantly tuned by the latter.

recorded the sensor response. (d) Each sliding was repeated 50 times. It is emphasized that (a) and (b) were performed to control the vertical force during sliding so as to make sliding condition constant. Here, the experiment were performed for sensor under three bending states that are θ=0, θ=$\pi/3$ and θ=π. Accordingly, dataset for each bending state contains 750 samples and within each dataset there are 250 samples for one indenter.

As for classification, four supervised learning algorithms including Decision Tree (DT), K-Nearest Neighbor (KNN), Support Vector Machine (SVM) and logistic regression (LR) were implemented. The original data, before feature extraction, were scaled to range between -1 and 1 with Maximum Absolute Normalization method (MAN). Mean and standard deviation of each sample were extracted as classification feature. At last, 30% of all data were selected as testing dataset. The classifiers and data pre-processing were performed with scikit-learn 0.20.1 [107]. While the performance of supervised learning highly depends on extracted features, it may undermine any conclusion derived from those results. Thereby, CNN was constructed for this classification task as it extracts features within own algorithm and requires no special domain expertise [105]. The structure of CNN is detailed in Fig. 4.9. In there, features of training data were extracted by four convolutional layers and four pooling layers before they were fed to a fully connected networks with one hidden layer for class output. Note that original data was downsampled to fixed length (1200) with scipy 1.3.1 [108] first. CNN was implemented in Tensorflow 1.14.0 [109]. All classifications were implemented on a computer with a CPU @ 2.40 GHz (Intel Core i5-9300H) and a RAM @ 16.0 GB.

The detailed parameters and settings of each classifier are as below. Note that I have tried to use the default setting by the package (scikit-learn) as it is the difference of performance on each data set that is of my care.

- DT: In this classifier, the "gini" impurity was used as the criteria to measure the quality of one split .
- KNN: KNN chooses k nearest neighbours to the classifying point from the training data and determines the label based on the label of these k training points [107]. In this classification, k is set as 5.
- SVM: The SVM was implemented with a Radial Basis Function (RBF) kernel. Two important parameters are key affecting the performance, that is C and γ, where C trades off the training accuracy and the margin of the hyper-plane, and γ tunes the influence of a single training sample [107]. In this task, $\mathrm{C} = 1.0$, and $\gamma = 0.01$.
- LR: The solver of the "One-vs-One" multinomial LR model was selected as "newton-cg" with L_2 regulation method [107]. In this model, the parameter C was set to be 1.0 by default.
- CNN: As shown in Fig. 4.9, the CNN consists of four convolutional layers with ReLU as activation function, and four pooling layers using maxpooling and "same" padding method. Each experiment was performed 100 epochs with learning rate being 0.0001.

Results

Fig. 4.10 shows typical sensor response during sliding at two different speeds, 8 mm/s in (A) and 4 mm/s in (B). The solid line indicates the average of 50 samples, and the shading area is the standard deviation. As clearly presented, the sliding pattern within each shape is quite constant, and unique compared with other shapes. Changing the sliding speed resulted in the same profile in different time scale, which indicates that the sliding pattern contains information unique to that indenter of particular shape. Further, mean and standard deviation of each sample were extracted and visualized in Fig. 4.11

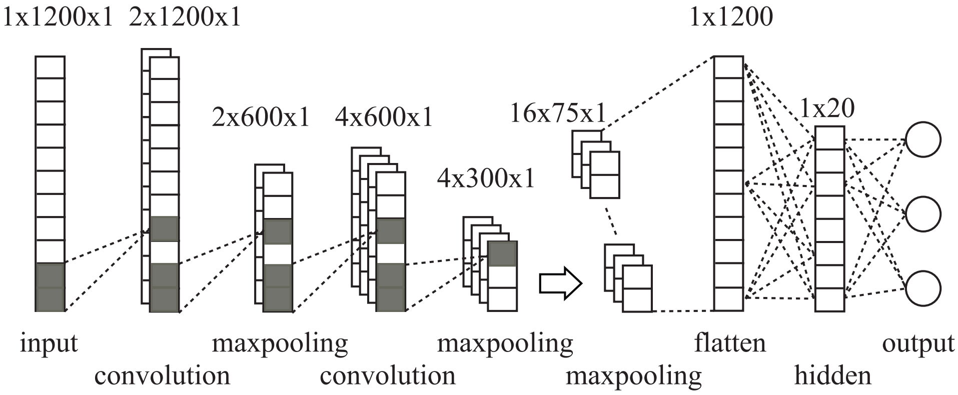

Figure 4.9: Architecture of the convolutional neural network, in which feature of signal was extracted by four convolutional layers and four pooling layers before it was flattened and fed to a fully connected network with one hidden layer for final classification. The overhead number indicates the data structure of that layer.

in order to examine the separability. (A) - (C) are data for bending cases $\theta=0$, $\theta=\pi/3$ and $\theta=\pi$ respectively in both 3D and 2D space. Note that the 3D panels are same data as 2D panel that were scattered by item number since some overlapping data in 2D space are not fully visible. Intuitively, sensor without bending shows most separable data, as in Fig. 4.11 (A). This remained true with the learning experiments where for all the four classifiers (DCT, KNN, SVM and LR), the case with largest wrinkles performed the best in term of classification accuracy presented in Table 4.2. Interestingly, while it does not rely on feature extraction, CNN showed the same performance trend as the common machine learning results. Therefore, it is fair to conclude that the changeable morphology offers this selectivity of the shape perception performance. Regarding the computation time, DCT, KNN, SVM and LR finished the training within 0.01 s, and CNN took about 20.38 s to complete 100 epochs.

Table 4.2: Learning Results (Classification Accuracy)

Bending Angles	**DT**	**KNN**	**SVM**	**LR**	**CNN**
0	0.991	0.991	0.959	0.991	0.996
$\pi/3$	0.898	0.893	0.671	0.671	0.984
π	0.796	0.671	0.668	0.711	0.792

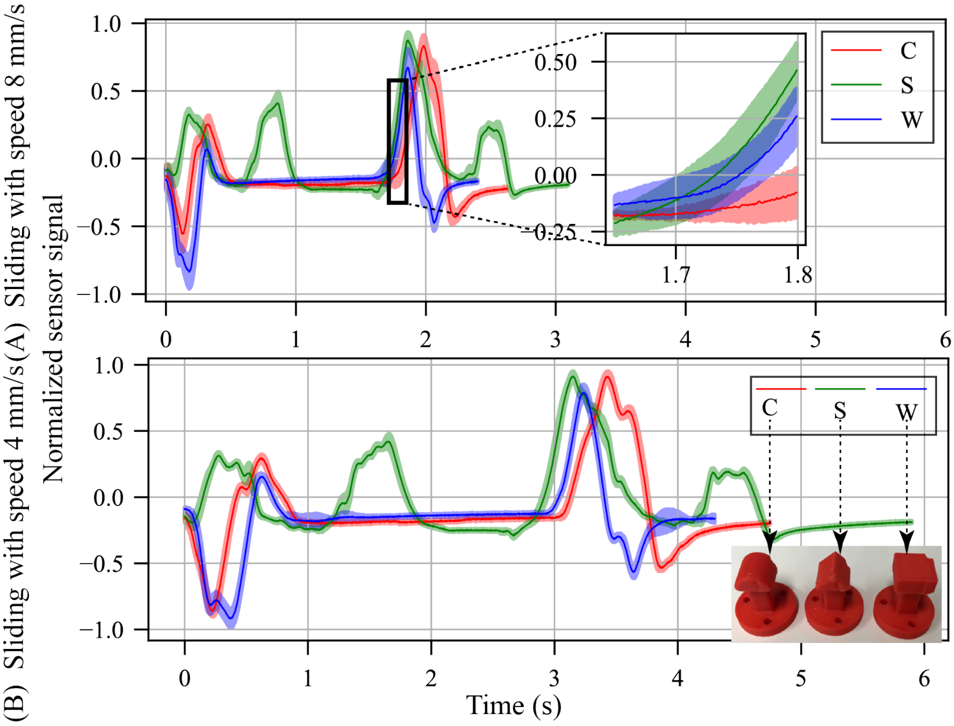

Figure 4.10: Sensor reading when indenter of different shapes slides on it with two speed options, 8 mm/s in (A) and 4 mm/s in (B). C, S and W indicate the shapes, namely semi-Cylinder, Square and Wedge, respectively. The solid line indicates the average of 50 samples, and the shading area the standard deviation. The response patterns are quite constant within each shape, and unique compared with other shapes. Different speeds resulted in the same profile but in different time scale, indicating that the response pattern contains information unique to that indenter of particular shape.

4.4.3 Texture detection

Setup

Same equipmental setup with two textured indenters as shown in Fig. 4.12 were utilized in this experiment. There are four grooves evenly distributed (10 mm apart) on each interacting surface. One indenter is with grooves of 0.1 mm wide (referred as "Texture 1") and the other of 0.2 mm (referred as "Texture 2"). Both were printed using a standard resin material (Clear FLGPCL04, formlabs, USA) with 3D printer (Form 2, formlabs, USA) that has minimum layer thickness of 25 microns. Closeup views of the texture grooves, illustrated in Fig. 4.12(C) and (D), were taken by a laser microscope (VK-9700, KEYENCE). Three measured sections for Texture 1 are 127.143, 127.979, 99.720 μm and for texture 2 are 183.097, 201.105, 181.158 μm.

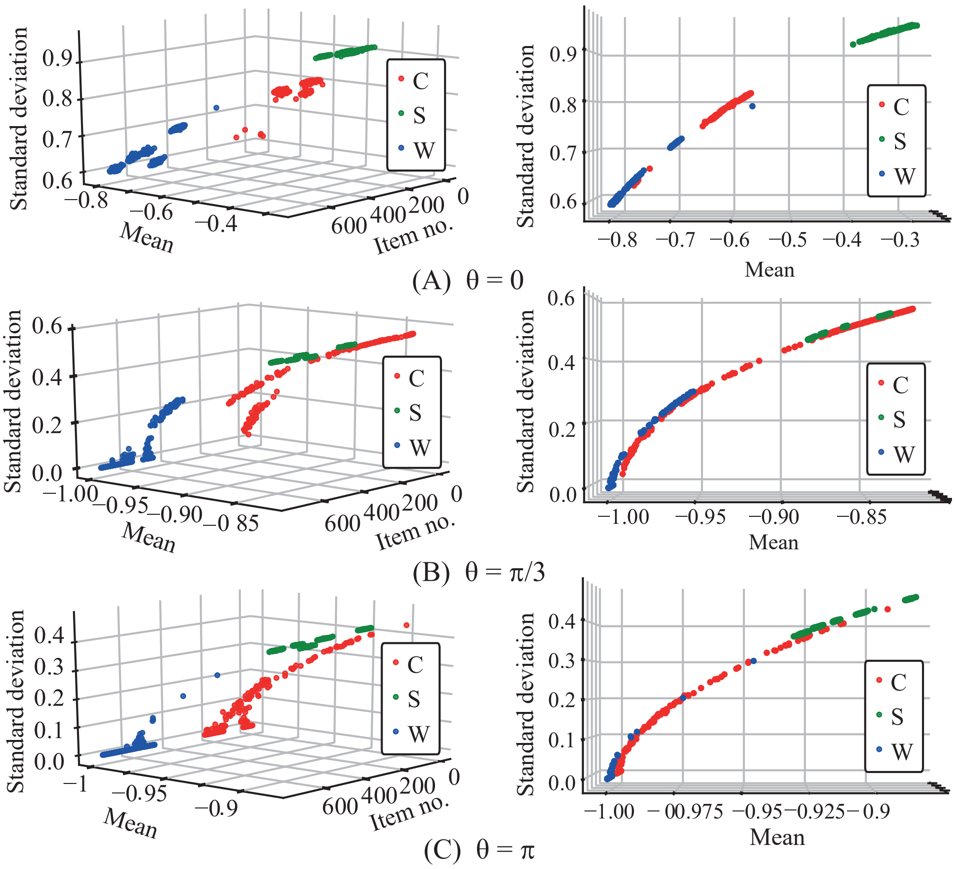

(A) θ = 0

(B) θ = π/3

(C) θ = π

Figure 4.11: Feature representation of sliding data with indenters of different shapes. Here, mean and standard deviation of each sliding data were extracted to represent one sliding sample. Panel (A), (B) and (C) show data points derived from sensor under $\theta = 0$, $\theta = \pi/3$ and $\theta = \pi$ in 3D (left) and 2D (right) spaces. Note that data in 3D coordinates are same data as those in 2D space but scattered by item number in order to visualize all the data points. Intuitively, sensor without bending shows most separable responses, as in panel (A).

Method

The indenter was adjusted so that the wrinkle with strain gauge was right under middle of the textured surface. The data were collected during sliding the textured surface over the wrinkled sensor. For each of the two indenters, following procedures were performed (a) Pressed the indenter against sensor until vertical force reached 0.1 N. (b) Slided the indenter leftward by 20 mm so that two grooves would pass over the sensor. (c) Slided rightward by 20 mm. (d) Repeated (b) and (c) once again before restoring indenter position. Each sliding test was repeated 3 times. The sliding speed was 4 mm/s.

For data evaluation, both temporal and frequency domain analysis were conducted. In detail, the distance from the minimum signal peak to signal mean value was compared with the standard deviation. Then the Fast Fourier Transform (FFT) was performed over the signal in order to find main frequency components. Specifically, for temporal analysis, it is assumed that the more obvious the target information is, the higher the accuracy of texture perception [98]. Thereby a good perception should (1) detect all the texture details it passes over. (2) has signal peak far away from the mean indicating the perception is more obvious. (3) has smaller standard deviation since signal fluctuation confuses target signal. For spectral analysis, the expected dominating frequency was calculated as Eq. (4.5),

$$f = \frac{1}{\frac{s}{v} + t_{delay}} \approx 0.363Hz \tag{4.4}$$

where s (10 mm), v (4 mm/s) and t_{delay} (0.25 s) denote the distance between grooves, the sliding speed and the delay time of control, respectively. Further, the amplitude ratio of the target frequency over sum of the range frequency as calculated as below for evaluation.

$$R = \frac{A_{target}}{\sum A_i}, i \in [0.2, 0.4] \tag{4.5}$$

where R is the ratio and A is the amplitude value.

Results

The sliding data were normalized with MAN and plotted in Fig. 4.13. Since two grooves slided over the wrinkled sensor for 4 times, it is expected to see 8 peaks detected in each sliding. As observed, the sensor could not find grooves on Texture 1 while all were able to detect those on Texture 2 with different sensitivity. Further, it shows a trend that the more the sensor is bent, the less variation the signal is. This was due to the stiffness change of the whole sensor. In order to evaluate the performance quantitatively, several parameters were listed in Table 4.3, where Signal Mean corresponds to red dotted line in Fig. 4.13, Signal Std. evaluates the signal overall fluctuation, Item No. marks the series number of lowest peak from left to right in Fig. 4.13, and distance measures the distance between the minimum peak and the signal mean. From here, bending state by $\pi/3$ outperforms others with largest distance. While bending state by π is most stable with least variation of signal. Based on the criterion aforementioned, bending state by $\pi/3$ is believed to be best in term of perception generally.

Additionally, the FFT was performed on the normalized signal after average has been removed for Texture 2, and the frequency components were plotted in Fig. 4.15, where (A), (B) and (C) show data from three bending cases by $\theta = 0$, $\theta = \pi/3$ and $\theta = \pi$, respectively. It shows that sensor when in all three bending states can detect the preferred frequency though the detected frequency is not the dominant component, which may require more sliding cycles for enhancement. Nonetheless, it is argued that the sensor when

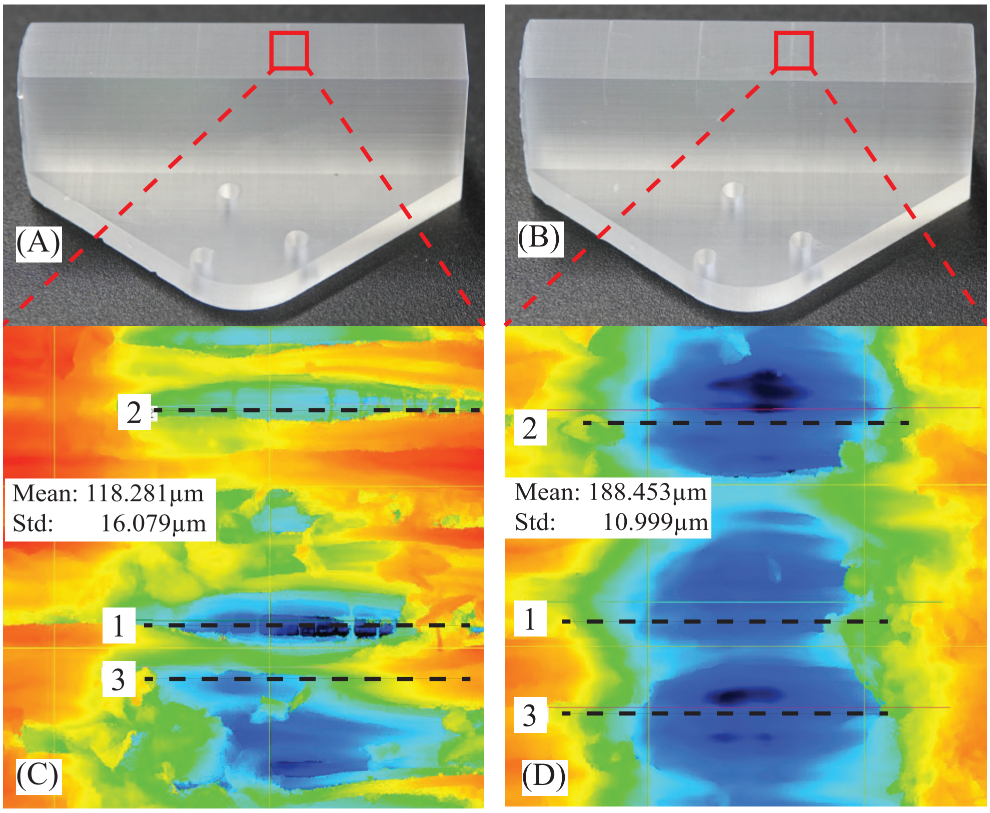

Figure 4.12: Indenters with grooves of 0.1 mm (Texture 1) in (A) and of 0.2 mm (Texture 2) in (B). (C) & (D) show closeup views of Texture 1 & 2 by a violet laser microscope. Dotted lines with item number indicate sections of measurement, where widths in (C) are 127.143, 127.979, 99.720 μm and in (D) are 183.097, 201.105, 181.158 μm. Note that the groove edges are blurred since laser beam goes through transparent indenters, causing less reflection for clearer boundaries.

bent by $\pi/3$ performed better than other states for three considerations, (1) Compared with bending case by 0, the ranking of the true sliding frequency in (B) is higher than that in (A), making the true frequency more obvious among other components within the signal itself. (2) Compared with bending case by π, true frequency has higher magnitude which indicates sensitive detection of the true frequency. (3) The amplitude ratio under this state is maximum ($R_0 = 0.41$, $R_{\pi/3} = 0.50$, $R_\pi = 0.46$). Therefore, among all three bending cases the bending by $\pi/3$ stands out in both temporal and spectral analysis.

4.5 Discussion

A few remarks need to be further discussed. First, compared with previous material combination, the present design showed a smaller range of vertical force because a softer substrate was utilized. Nonetheless, this would not be our concern as one can always

Table 4.3: Information about Lower Peak

Bending Angles	**Signal Mean**	**Signal Std**	**Item No.**	**Distance**
0	-0.293	0.123	4^{th}	0.228
$\pi/3$	-0.486	0.091	4^{th}	0.274
π	-0.575	0.078	1^{st}	0.135

manipulate this by using an alternative material combination, which had been modeled and elaborated in [2].

The tunable ability of texture detecting found can infer the function of human fingerprints. As shown in Fig. 4.14, when there is no or very small wrinkle, no local deformation will be caused during sliding. On the contrary, when the wrinkle exists, it can then extend itself to find the texture detail on the surface.

The bending actuation was implemented in a discrete manner, namely by an array of static platforms. However, for the purpose of a future application in an active tactile sensing system, an actuator capable of continuous bending is then required. A promising solution is an robotic finger as illustrated in Fig. 4.1, where the bending state of the sensor can be tuned by the joint rotary motion.

A limited number of morphological options were tested for shape classification and texture detection. The integration of continuous bending actuator will enable an online optimization process thus offering an unlimited number of sensor morphology in order to get best performance. Once this interdependence relationship is thoroughly known, only a simple controller with less expensive computational power will be needed for realization of active sensing process, as part of the computational work that would have been done to vary the sensorimotor strategy for better perception has been “offloaded” to sensor morphology.

4.6 Conclusion

We have presented that the wrinkle structure and overall stiffness of the proposed sensor could be changed significantly by simple bending actuation. These morphological variations were demonstrated to be effective in tuning the performance of sensing and perception in different tasks, by implementing three tests including vertical force sensing, shape classification and texture detection for the sensor in different bending states. Within the range of morphological variation tested, there was an uniquely optimal state for each

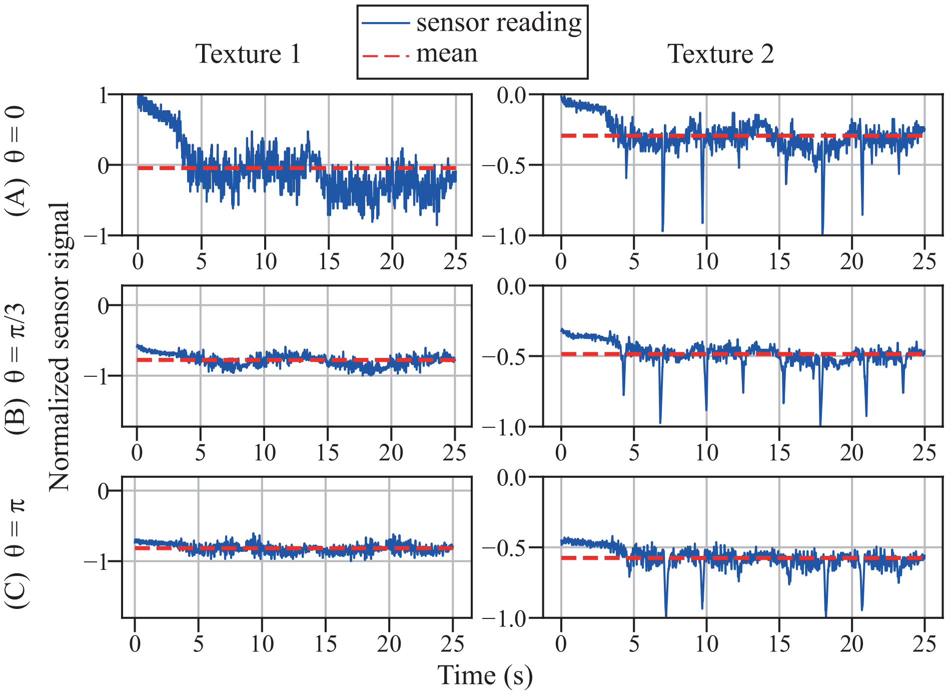

Figure 4.13: Sensor responses to sliding with two textures when sensor is under three banding states, $\theta=0$ in (A), $\theta=\pi/3$ in (B) and $\theta=\pi$ in (C). Since two grooves slided over the sensor for 4 times, it is expected to detect 8 peaks. Obviously, the sensor can not find grooves on Texture 1 while was able to detect those on Texture 2. While it performed best when sensor was bent by $\pi/3$ as the distance between minimum peak and signal mean is most obvious, which limits the best sensitivity to that groove. This conclusion will be further justified by spectral analysis.

task, indicating the possibility of enhancing tactile perception by, rather than changing sensorimotor control strategy, adapting the sensor morphology to specific tasks, which is computationally much cheaper. These findings are believed to shed light for novel active sensing system design that alleviates the needs for high computational power and large integration complexity of the central control system.

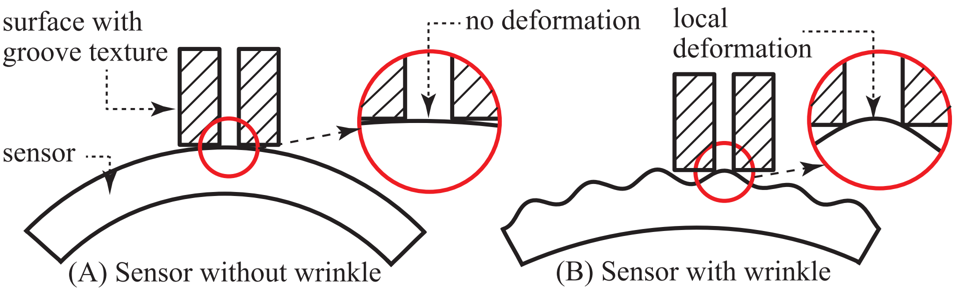
surface with
groove texture
sensor
no deformation
local
deformation
(A) Sensor without wrinkle
(B) Sensor with wrinkle

Figure 4.14: Illustration of texture detection scenarios. (A) When there is no wrinkle on sensor, no local deformation happens in between object and sensor. (B) Wrinkle of feasible size can extend itself and interact with texture more closely in order to respond during sliding.

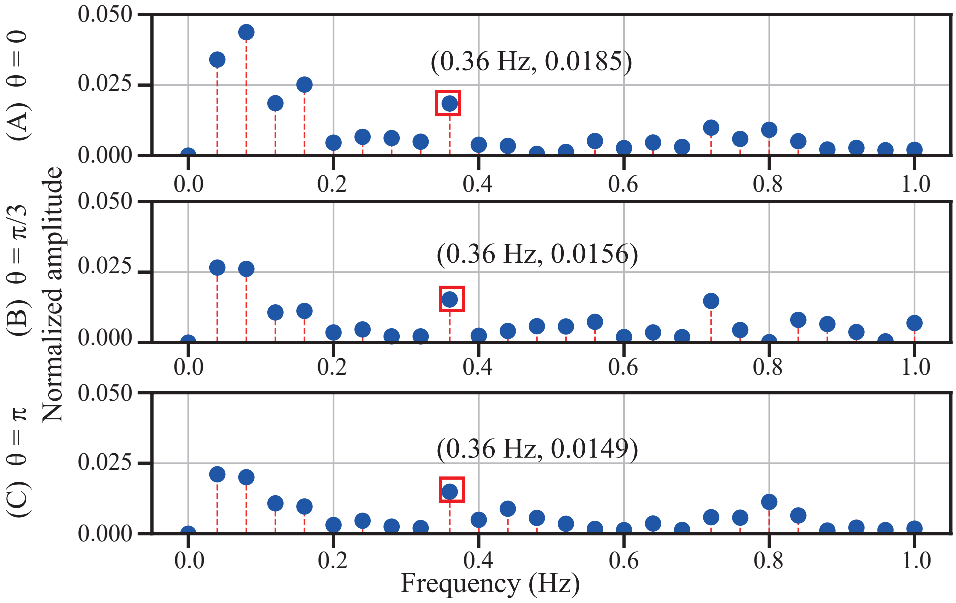

Figure 4.15: FFT analysis of texture sliding signal when sensor is under three different bending states, $\theta = 0$ in (A), $\theta = \pi/3$ in (B) and $\theta = \pi$ in (C). While the sensor in all three bending states can find the real sliding frequency, the sensor bent by $\pi/3$ is argued to perform the best based on two observations, (1) compared with case of no bending, the ranking of the true sliding frequency in (B) is higher than in (A), making the true frequency more obvious among other components, (2) compared with bending case by π, true frequency has higher magnitude which infers sensitive detection of the true frequency.

Chapter 5

Adaptive Morphology Facilitating Gripping Functionality : RetracTip

Abstract

This chapter introduces a new prototype called "RetracTip" which is a multifunctional and energy-efficient gripper. RetracTip consists of a pinned gripper for gripping and an embedded camera for sensing functionality. The gripper is enabled by an adaptive morphing dome membrane with pins on its outer surface. The morphing dome is bistable in that it can stay at either of the two stable states "natural" and "retracted" with further energy input. This property is potentially very helpful in that during holding an object, the gripper costs no power regardless of the operating time. This chapeter includes a series of evaluations on the functions separately and then jointly for characterization. From the viewpoint of the mechanical design, RetracTip was evolved from its early predecessor, "TacTip" which is a visual tactile sensor, by fitting the pinned morphing membrane into the structure, offering the extra gripping functionality. This provides another argument that adaptive morphology can potentially extends functionality of soft robotics and optimized the gripping function by improving the power efficiency.

5.1 Introduction

Soft robotics has been directed to augment the ability of robots to function more securely, adaptively and autonomously with reduced system complexity in unstructured environments [5, 10, 110]. This trend embraces those robots that are multifunctional and energy efficient [10]. Biology has long been a source of inspiration for robotics. From this perspective, sea anemones are enormously potential. Extremely simple as they are since neither visual capacity nor centralized nervous system but four main components (tentacles, a mouth, an internal cavity and a hydraulic skeleton with retract muscles as in Fig. 5.1 Inset 1) exist, they can effectively detect, immobilize, catch and transport for ingestion preys of arbitrary sizes and shapes [111], which have been enabled by the efficient coupling of sensing and actuation. The sea anemones deliver remarkable enlightenment towards compact and multifunctional soft robotic grippers capable of self-sensing, detecting, and grasping unknown objects with enhanced security, reliability and energy efficiency, and the trend has been proposed in review articles [19, 112, 113].

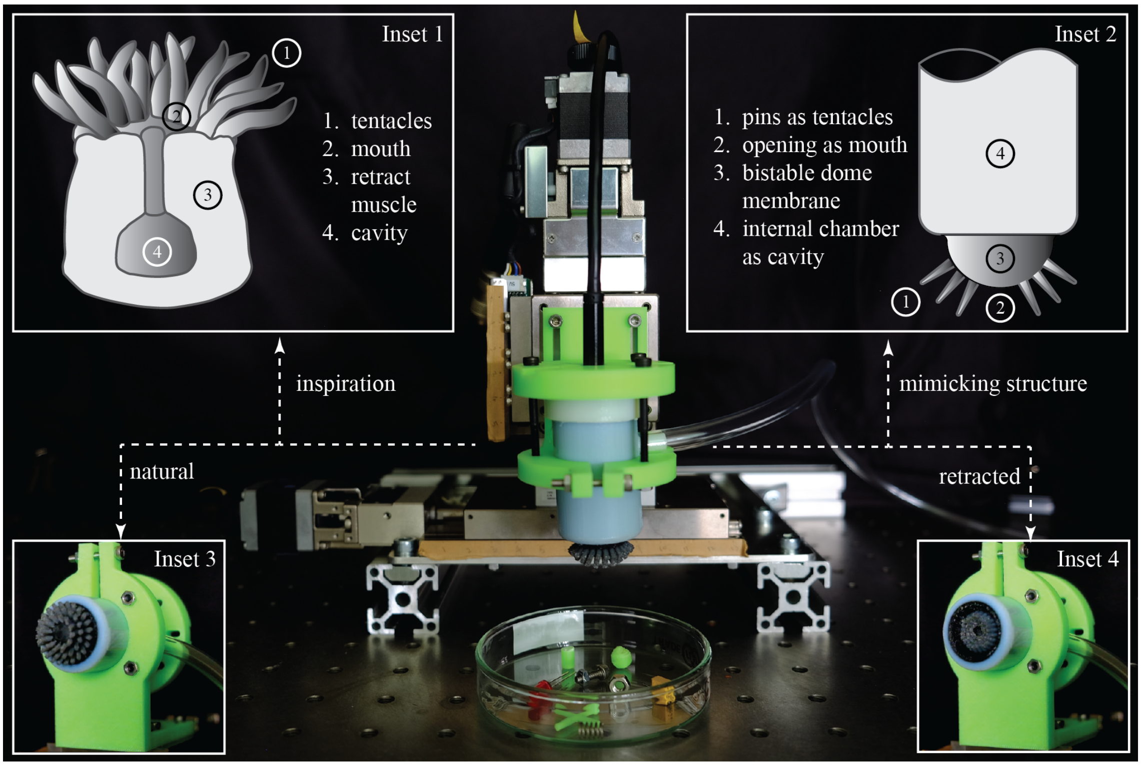
Inset 1
①
②
③
④
1. tentacles
2. mouth
3. retract muscle
4. cavity
Inset 2
1. pins as tentacles
2. opening as mouth
3. bistable dome membrane
4. internal chamber as cavity
inspiration
mimicking structure
natural
retracted
Inset 3
Inset 4

Figure 5.1: Conceptual design of RetracTip and its engineering setup of an autonomous gripping system. Inset 1 is the biological structure of sea anemone and inset 2 is the bio-inspired structure of RetracTip. Insets 3 and 4 indicate the two states ("natural" and "retracted") that enable the grip and release functionality.

By mimicking the body structure of sea anemones, we propose a compact, multifunctional and energy efficient universal gripper design as in Fig. 5.1. As an analogy to the predation behaviour of sea anemones, the gripper can self-sense, detect and grip various objects with arbitrary sizes, shapes and weights. The energy efficiency is improved by eliminating the need for continuous actuation during the holding process with creative implementation of a bistable spherical dome membrane. Moreover, because of the bistability, the gripper is augmented with friction modulating capability that can potentially be useful for applications such as active manipulation.

The article starts with an introduction of the concept and the background. Then it is followed by an elaboration of conceptual design and fabrication. The threshold geometry of transition from monostability to bistability is decided based on finite element method simulation. The gripper is then verified in terms of its separate multiple functions including sensing (proprioceptive and exteroceptive), gripping (grasping and pinching) and friction modulation. After, a case study is presented to demonstrate the potential to serve as an intelligent sensorized gripper. The discussion is followed before the conclusion finally.

5.2 Related Works

5.2.1 Robotic grippers

Robotic grippers often appear in three common morphological designs, that is, multifinger-based, suction-based and pin-based. The pioneer anthropomorphic multifinger grippers are represented by the work of Suzumori et al. consist of four fluidic elastomer actuators yielding the ability to grasp and manipulate a variety of objects even metal handtools [114]. Since then, there have been a substantial number of examples that either diversify materials [115] and principles in design [116], specify application [106, 117] or augment functionality [118]. Provided the success in animals, this design obviously has many advantages. Yet, fast gripping of small items remains challenging as precise synchronization of all fingers is vital. The suction-based grippers usually include a membrane-chamber structure enabling envelop of objects by various actuation approaches such as pneumatic [14, 119, 120], tendon-driven [121], gravity-induced [122]. The jamming grippers, within the pneumatic category, have attracted much attention because of rapid reaction, increased adaptability and reduced system complexity [14]. Apart from the representative design of granular jamming, new mechanisms are being exploited such as tubular jamming [42], fibre jamming [40] and layer jamming [41]. However, as a pre-gripping enveloping is required, such design may struggle in soft and flat material handling. The pin-based design often adapts to the shape of objects by vertical and exert force by lateral movement of an array of pins. Since the early demonstration [123], there have been a number of updates that contribute to optimization [124], bioinspiration [125] and new applications [126, 127]. Compared with the other two morphological forms playing important roles in soft robotics, the pin-based designs remain active dominantly in conventional robotics, offering great research potentials for soft robotic grippers.

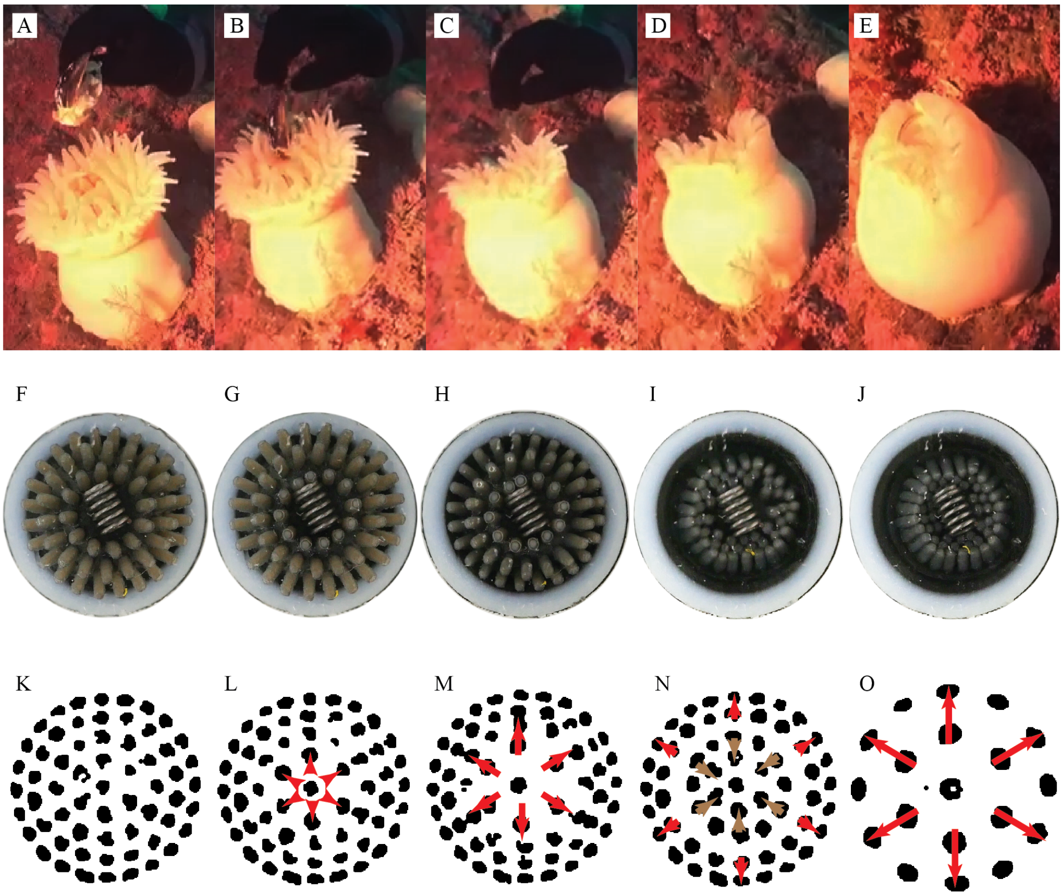

Figure 5.2: Demonstration of preying process of sea anemones and the gripping and sensing functionality of RetracTip. (A)-(E) show the preying behaviors of sea anemone, and filming courtesy of Erlendur Bogason [3]. (F) - (J) present the spring-gripping process of RetracTip. The gripping is enabled by pressing RetracTip against the target to activate the snap-through behavior of RetracTip along which the wrapping movement of pins happens. (K) - (O) show the distribution of markers during the spring gripping process, demonstrating the sensing capability of RetracTip.

5.2.2 Tactile sensing in robotics

Tactile sensing enables the agents, biological or artificial, into which it is incorporated the ability to understand both themselves and environment [113]. It is vital towards intelligent and autonomous grippers. Various tactile sensing technologies have been developed, including those that are piezoelectric [128], resistive [129, 130], capacitive [131], magnetic [132], and optical [133]. For soft robotic integration, tactile sensors must be compliant to not affect the intrinsic property of the soft body, and resilient to provide reliable signals over many cycles [134]. Given all these needs mentioned, one promising technology provides tactile knowledge, such as deformation, force and material property, by visual information, and representative examples include Gelforce [135], GelSight [136], TacTip [137].

The TacTip is particularly interesting because of its compact and biomimetic design that was inspired by the mechanoreceptors in human fingertips making it possible to provide abundant tactile information [137]. Sensorized grippers with TacTip integration include M2 [138] and TacEA [139].

5.2.3 Energy efficiency and bistable structures

Improving energy efficiency is a preferable trend towards unleashing the full potential of soft robotics [110, 140]. All the aforementioned grippers, however, require continuous energy input to maintain holding objects thus intuitively are less efficient in power. Bistable structures are potentially promising to reduce the energy consumption because they seek to settle in either of the equilibrium configurations without the need for continuous actuation [141]. Specifically, spherical caps, as recognized among the simplest examples of bistability [142], can snap through from the "natural" (initial) state to the "retracted" state and stabilize there when loading is removed. They can as well snap back in the reversed direction when properly actuated. Once the material is specified, bistable spherical caps can be monostable or pseudostable [143] depending on the parameter variations such as depth, thickness and boundary condition [144]. By leveraging the stability of bistable structures, extraordinary performance can be achieved for soft robots with examples including autonomous control [145], rapid locomotion [146] and energy efficient actuation [147, 148]. Based on different applications, the actuation can be pneumatic [147], piezoelectric [146], magnetic [149], and thermal [150], among which the pneumatic approach is straightforward to fabricate and implement.

5.3 Concept, Simulation and Design

5.3.1 Concept

As aforementioned, sea anemones demonstrate a compact and elegant design of body structure that couples sensing and actuation functionality, enabling their autonomous and effective predation behavior. As illustrated in Fig. 5.1 Inset 1, the body mainly consists of four components, that is the tentacles, the mouth, the membrane with retract muscles, and the internal cavity. When preying, sea anemones detect targets with extended membrane and tentacles, then catch and transport them to the mouth for ingestion by retracting the membrane and tentacles to envelop the targets before swallowing (as shown in Fig. 5.2 A - E) [3].

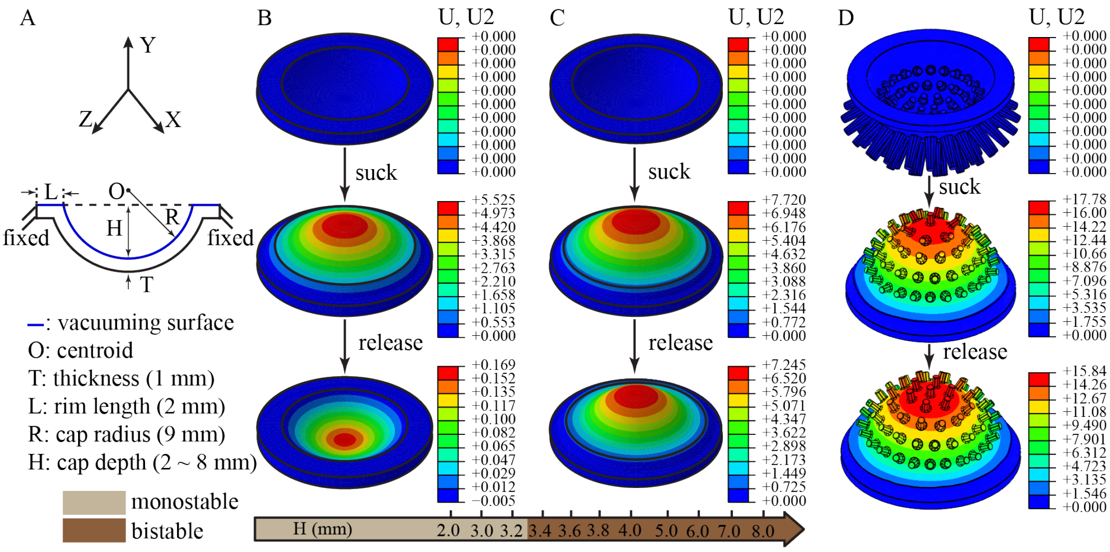
A
B
C
D
Y
Z
X
L
O
R
H
T
fixed
fixed
—: vacuuming surface
O: centroid
T: thickness (1 mm)
L: rim length (2 mm)
R: cap radius (9 mm)
H: cap depth (2 ~ 8 mm)
monostable
bistable
suck
release
suck
release
suck
release
U, U2
+0.000
+0.000
+0.000
+0.000
+0.000
+0.000
+0.000
+0.000
+0.000
+0.000
+0.000
+5.525
+4.973
+4.420
+3.868
+3.315
+2.763
+2.210
+1.658
+1.105
+0.553
+0.000
+0.169
+0.152
+0.135
+0.117
+0.100
+0.082
+0.065
+0.047
+0.029
+0.012
−0.005
U, U2
+0.000
+0.000
+0.000
+0.000
+0.000
+0.000
+0.000
+0.000
+0.000
+0.000
+0.000
+7.720
+6.948
+6.176
+5.404
+4.632
+3.860
+3.088
+2.316
+1.544
+0.772
+0.000
+7.245
+6.520
+5.796
+5.071
+4.347
+3.622
+2.898
+2.173
+1.449
+0.725
+0.000
U, U2
+0.000
+0.000
+0.000
+0.000
+0.000
+0.000
+0.000
+0.000
+0.000
+0.000
+0.000
+17.78
+16.00
+14.22
+12.44
+10.66
+8.876
+7.096
+5.316
+3.535
+1.755
+0.000
+15.84
+14.26
+12.67
+11.08
+9.490
+7.901
+6.312
+4.723
+3.135
+1.546
+0.000
H (mm)
2.0
3.0
3.2
3.4
3.6
3.8
4.0
5.0
6.0
7.0
8.0

Figure 5.3: FEM simulation results of bistability of spherical caps and of RetracTip. (A) indicates the dimension of spherical caps. (B) and (C) present the typical behavior of monostability ($H < 3.3$ mm) and bistability ($H > 3.3$ mm), respectively. The colormaps show the displacement along Y-axis. (D) verifies the bistability of RetracTip before fabrication.

Inspired by this retracting-characterized predation mechanism and sensing behavior, we propose a compact and multifunctional universal gripper with sensing (proprioceptive and exteroceptive) and gripping (grasping and pinching) integrated. The conceptual design is presented in Fig.5.1 Inset 2. As an analogy to the biological structure, RetracTip consists of an array of rigid pins distributed on a spherical membrane with an open area in the middle to offer space for objects. The internal chamber generates adequate space for membrane to retract for griping. Here, the membrane is bistable offering two equilibrium configurations referred to as “natural” and “retracted” state shown in Inset 3 and Inset 4, respectively. When forced to push against objects or pneumatically vacuumed, the gripper can retract from the “natural” state to the “retracted” state and settle there without continuous loading required. The gripping functionality is realized by the centripetal gathering movement of the pins because of the local-lever effect along with the membrane retraction (as demonstrated in Fig. 5.2 F - J). Because of this, the gripper is coined as “RetracTip”. To further equip RetracTip with sensing capability, one overhead camera is adopted to track the movement and distribution of markers printed inside the membrane thus to realize both proprioceptive and exteroceptive sensing. Fig. 5.2 K - O demonstrate the exteroceptive sensing potentials. Additionally, compared with peer grippers, RetracTip is energy efficient in that it can settle in either of the stable states and no further energy input is required.

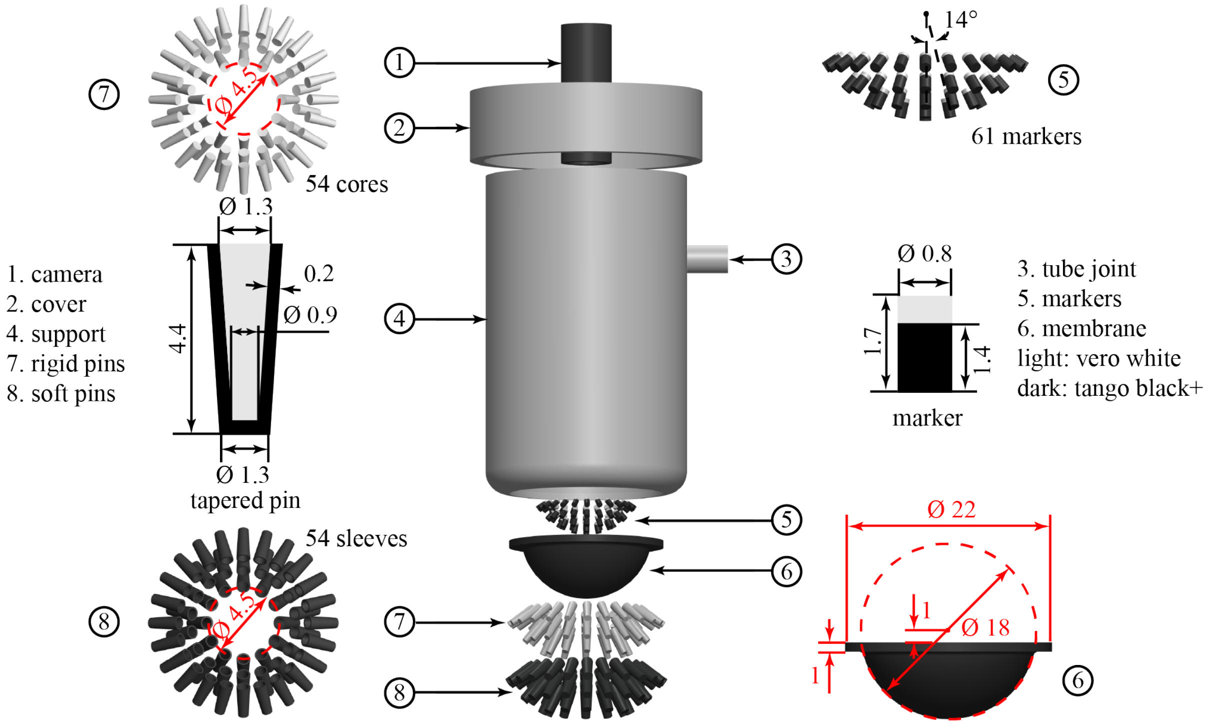
⑦
Ø 4.5
54 cores
Ø 1.3
1. camera
2. cover
4. support
7. rigid pins
8. soft pins
4.4
0.2
Ø 0.9
Ø 1.3
tapered pin
54 sleeves
⑧
Ø 4.5
①
②
③
④
⑤
⑥
⑦
⑧
14°
⑤
61 markers
Ø 0.8
1.7
1.4
marker
3. tube joint
5. markers
6. membrane
light: vero white
dark: tango black+
Ø 22
1
Ø 18
1
⑥

Figure 5.4: Mechanical design of RetracTip. 54 tapered pins and 61 markers are printed on a bistable membrane. The rigid core inside the pins is to stiffen them and the white cap on top of markers is for the tactile information tracking by the overhead camera sensor. External pneumatic source is used to trigger the snap-through and snap-back by vacuuming and pressurizing RetracTip via the tube joint.

5.3.2 Design and simulation

The bistability of the spherical membrane is essential in this design. As reviewed in the introduction, it depends on several factors including the depth (H), the thickness (T) and the boundary conditions (as shown in Fig. 5.3 A). The dome membrane with specified material can be either monostable or bistable depending on these parameters. For instance, when the boundary condition and thickness are specified, there is a threshold depth in that caps "deeper" than this threshold are bistable, otherwise are monostable. In an effort to minimize the trial-and-error design and fabrication process, we first ran a series of Finite Element Method (FEM) simulations for dome membranes with a predefined thickness to decide the threshold depth. Then we came up with the mechanical design of RetracTip as illustrated in Fig. 5.4. Finally we simulated the bistability of RetracTip before fabrication in order to verify that the bistability would not be affected by the added pins and markers. The simulation was performed with Abaqus/CAE, a professional software for FEM modelling.

Simulation of dome membranes. The bistability was simulated by vacuuming the internal surface of the dome membrane with a fixed rim as shown in Fig. 5.3 A. Here, we fixed the radius (R) and thickness (T), and varied the depth (H) from 2 mm to 8 mm with a step increment of 0.2 mm. The material was set to be Tango Black+ with a linear constitutional model (Young's modulus: 0.1 MPa, Poisson ratio: 0.48) [151]. It was modeled as a two-step quasi-static process (dynamic, implicit) as the dynamic response is beyond our concern. We first vacuumed the membrane with a negative pressue (P) to trigger the snap-though, then released the vacuum after it stabilized in the retracted position. As illustrated in Fig. 5.3, the threshold depth was found to be 3.3 mm. A typical monostate example is present in Fig. 5.3 B (Monostable, H = 3 mm, P = 0.5 kPa) and a bistable result in Fig. 5.3 C (Bistable, H = 4 mm, P = 0.5 kPa). As can be seen, both membrane snap through from the natural state to the retracted state when activated. When deactivated, the monostable structure snaps back to the original state while the bistable remains at the retracted position.

Design. With the threshold depth being determined, the mechanical design of the gripper was then settled as shown in Fig. 5.4. To mimick the tentacles of sea anemone, we printed an array of 54 tapered pins on the outer surface of the membrane. The pins consist of rigid cores to increase the stiffness and soft skins to increase friction force for gripping. Inside the chamber, we printed a total number of 61 cylindrical markers on the internal surface for tactile information extraction. The markers were designed to have white caps on top for the purpose of easier tracking their movement and distribution. The dimensions were designed to not affect the bistability of the dome membrane. For fabrication, the whole structure was 3D printed with a dualmaterial 3D printer (Stratasys Ltd, USA). The rigid components (marked as light colour in Fig. 5.3) were printed in hard plastic material (Vero White) while the soft parts (marked as dark color) were in a rubber-like material (Tango Black). A USB camera (640 × 480 pixels, Inspection Cameras, UK) with tunable LED illumination was mounted overhead to extract the tactile information during action.

Simulation of RetracTip. As the pins and markers would increase the overall stiffness thus influence the bistable property, we simulated the complete membrane structure with pins and markers to verify the bistability of the design before fabrication. Instead of the method of "dynamic, implicit", "dynamic, explicit" was adopted because the former struggled with an infinite long calculation time. The rigid material was set to be Vero White with a linear constitutional model (Young's modulus: 2495 MPa, Poisson ratio: 0.4)51, the soft material was the same Tango Black +. In order to improve the efficiency of analysis, the mass during the simulation was scaled up by a factor of 1,000,000. The quasi static process was achieved by increasing the step time, that is, 40 s for vacuuming and 120 s for releasing. The result is finally presented in Fig. 5.3 D and the bistability was found to remain with the added pins and markers, justifying the feasibility of our design.

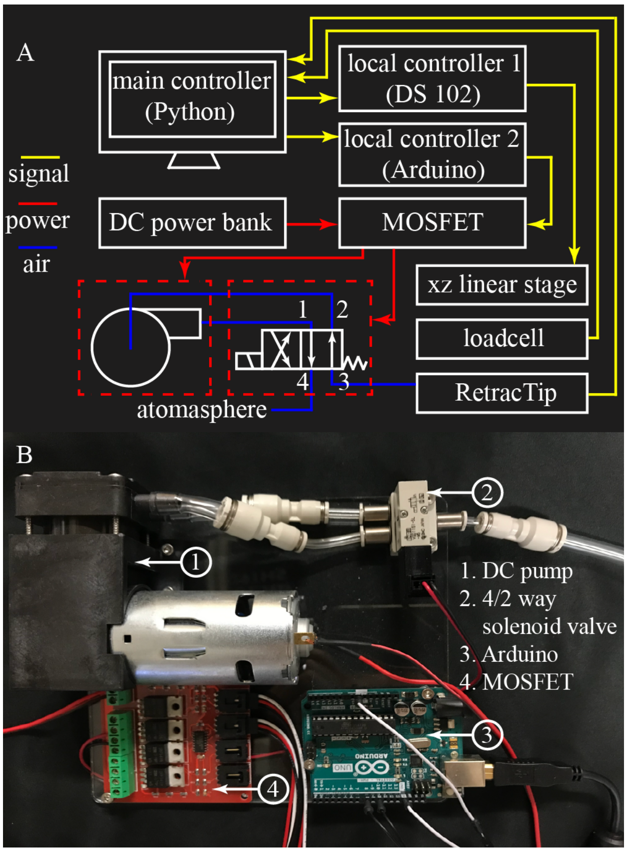
A
main controller
(Python)
local controller 1
(DS 102)
local controller 2
(Arduino)
signal
power
air
DC power bank
MOSFET
xz linear stage
loadcell
RetracTip
1
2
4
3
atomasphere
B
②
①
1. DC pump
2. 4/2 way
solenoid valve
3. Arduino
4. MOSFET
③
④

Figure 5.5: The experimental setup. (A) overviews the system setup including control, power, pneumatic and motor systems. The control system consists of one main controller and two local controllers (DS 102 for the motor system and Arduino for the pneumatic system). The main controller synchronizes the sensing of RetracTip and the control of two local controllers. (B) illustrates the pneumatic system which is capable of vacuuming and pressurizing RetracTip by switching off/on the solenoid valve. A distributed control algorithm is implemented in local controller 2 (Arduino) which receives a control signal from the main controller.

5.4 Experiments and Results

RetracTip has multiple functionalities including sensing (proprioceptive and exteroceptive), multimodal gripping (grasping and pinching) and friction modulating. Here, we first conducted a series of experiments to validate all the claimed functions separately. Then we constructed an autonomous gripping system to demonstrate the potential to achieve closed-loop gripping control that is all based on the integrated functionalities within RetracTip.

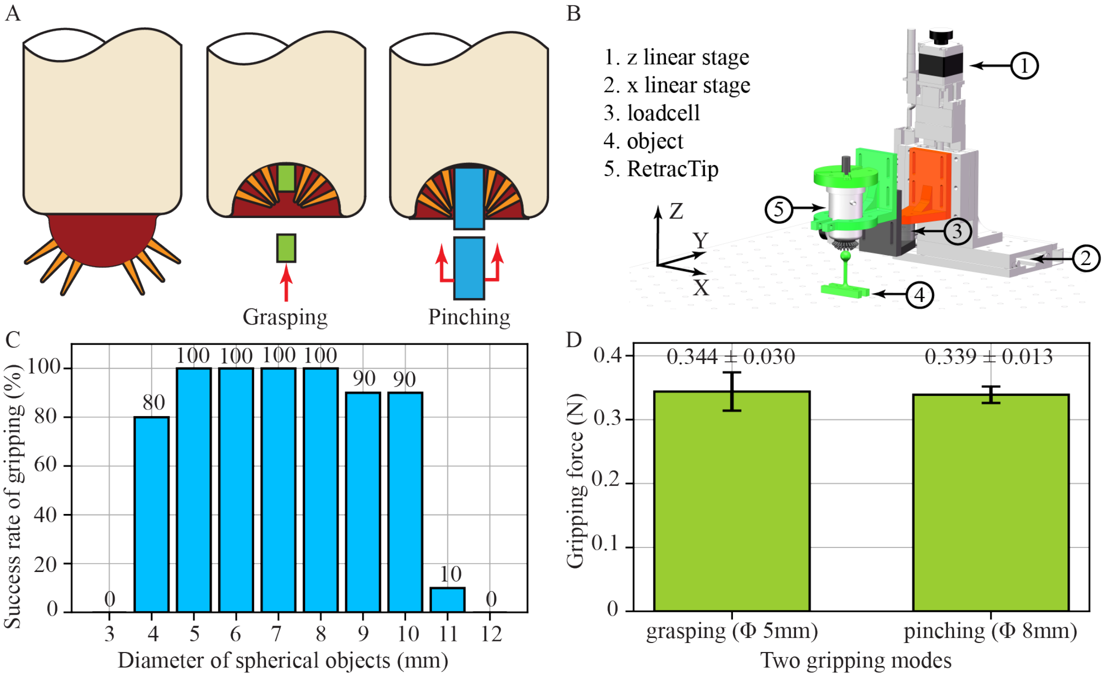

Figure 5.6: Two gripping modes and the corresponding characterization of griping capability. (A) shows the schematic of two gripping modes, that is, grasping and pinching, depending on the size of objects. (B) indicates the experimental setup for the characterization experiments in (C) the gripping size testing and in (D) the gripping force testing. The gripping size testing was performed by examining the successful rate of gripping a series of spherical objects with various diameters. The gripping force testing was conducted for the two gripping modes by selecting the size of targets.

5.4.1 Experimental setup and methodology

System overview. As presented in Fig. 5.5 A, the experimental setup consists of a control system, a power system, a motor system, a pneumatic system (xz linear stage) and a loadcell system in addition to RetracTip. The hierarchical control system contains a main controller in Python and two local controllers, one for motor system and the other for pneumatic system. The main controller here is used to synchronize control of two local controllers and sensing of RetracTip. The motor system is A 2-DOF linear stage (horizontal: PG-650, vertical PZG-615, Suruga Seiki, Japan) with a local controller (DS 102, Suruga Seiki, Japan). The pneumatic system, as shown in Fig. 5.5 B, can be used to either vacuum or persurize RetracTip by switching off and on the solenoid valve. A distributed control algorithm is implemented in local controller 2 (Arduino UNO) which receives the control signal from the main controller (in Python). Additionally, the loadcell (Nano17 SI-50-0.5, ATI Industrial Automation, USA) can provide force information, where needed, to the main controller via a data acquisition device (NI USB 6343, National

Instrument, USA).

Sensing methodology. As shown in **Table** 5.1, the sensing capability is realized by examining the distribution and location of markers in images sampled by the overhead camera (at 20 fps) using OpenCV (www.opencv.org) in Python. Specifically, the RGB images are filtered, converted into binary colour and cropped to 300×300 pixels. Each image is then divided into four regions of interest (ROI), that is top, bottom, left and right (as shown in **Table** 5.1 note section). The distribution of markers in each ROI is extracted by calculating the area of marker in pixels and denoted by T, B, L and R. The tactile perception can be realized based on the analysis of these marker distributions.

Table 5.1: Results for Proprioceptive and Exteroceptive Sensing

Tasks	Image samples		Area of makers (pixels)	Sensing principles
Selfstate sensing	Natural state	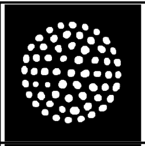	T: 11342 ± 116 (T_{ori}) B: 11512 ± 85 (B_{ori}) L: 11241 ± 38 (L_{ori}) R: 10923 ± 167 (R_{ori})	$T_{ori} \approx B_{ori} \approx L_{ori} \approx R_{ori}$
	Retracted state	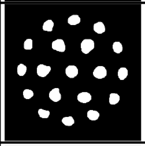	T: 9827 ± 125 B: 8128 ± 69 L: 7079 ± 153 R: 6983 ± 31	$T, B, L, R \ll T_{ori}, B_{ori}, L_{ori}, R_{ori}$
Self direction sensing	Sliding rightwards	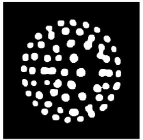	T: 10516 ± 161 B: 10500 ± 399 L: 11609 ± 280 R: 10242 ± 29	1. $T, B < T_{ori}, B_{ori}$ 2. $L > R$
	Sliding leftwards	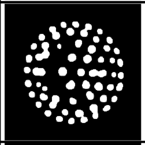	T: 10679 ± 385 B: 10477 ± 279 L: 9544 ± 255 R: 11040 ± 307	1. $T, B < T_{ori}, B_{ori}$ 2. $L < R$
Terrain sensing	Tapping on convex terrain	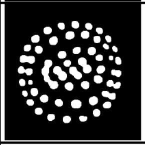	T: 10477 ± 252 B: 8960 ± 19 L: 13146 ± 129 R: 13366 ± 422	1. $T, B < T_{ori}, B_{ori}$ 2. $L, R > L_{ori}, R_{ori}$
	Tapping on flat terrain	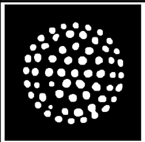	T: 10592 ± 62 B: 11338 ± 11 L: 10195 ± 267 R: 10497 ± 143	1. $T \approx B \approx L \approx R$ 2. $T, B, L, R < T_{ori}, B_{ori}, L_{ori}, R_{ori}$
	Tapping on concave terrain	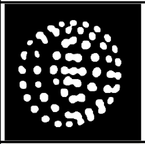	T: 12777 ± 383 B: 12419 ± 215 L: 9038 ± 162 R: 11799 ± 137	1. $T, B > T_{ori}, B_{ori}$ 2. $L, R < L_{ori}, R_{ori}$
Note		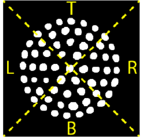	**1.** T, B, L, R refer to the area of markers in top, bottom, left and right region of interest, respectively. **2.** The regions of interest (T, B, L, R) are segmented by left regime.	

5.4.2 Sensing

Proprioceptive sensing

Proprioceptive sensing refers to the ability of agents to sense and perceive their own state. Here, we performed two experiments demonstrate this functionality of RetracTip. One is to sense the present stable state and the other is to detect its moving direction. In the first experiment, RetracTip was vacuumed with the pneumatic system to snap through from the natural state to the retracted state and then was inflated to snap back. In the meantime, the distribution and movement of the markers on the membrane were recorded by the overhead camera. This process is demonstrated in **supplementary video** 1. This test was repeated for three times, and typical marker distribution for each state is shown in **Table** 5.1 self-state sensing section. As can be seen, the markers distributed evenly in each ROI in the natural state and reduced substantially in the number and the density in the retracted state (T, B, L, R $\ll$ Tori, Bori, Lori, Rori, over 10%), enabling the differentiation of these two state.

In the second experiment, RetracTip was slided on a flat surface rightwards and then leftwards along x direction (as illustrated in Fig. 5.8 A), with a predefined initial vertical force of 1 N. Specifically, RetracTip was first pressed agrainst the surface (by the z linear state) until the force threshold monitored by the loadcell. It was then slid along x direction forth and back (0.5 mm/s) while the membrane deformation was recorded by the camera. As shown in **supplementary video** 2, the distribution of the markers in each ROI when sliding leftwards is quite distinct from that when sliding rightwards, especially in the left and right regions. For direction detection, the marker areas were quantified and presented in **Table** 5.1 self-direction sensing section. While the areas in top and bottom remained similar for both stokes, those in left and right presented obvious distribution characteristics, that is $L > R$ (11609 ± 280 and 10242 ± 29, respectively) when sliding towards right and $L < R$ (9544 ± 255 and 11040 ± 307, respectively) in the other direction.

Exteroceptive sensing

Exteroceptive sensing relates to the ability to acquire information about the external environment, for example shape and texture of objects. Human beings usually tap to feel softness and press to sense edges and shapes. Inspired by such behaviours, we indented RetracTip with specified vertical force (1 N) against a surface on which there exist three different terrains (convex, flat and concave). In each indention, as shown in **supplementary video** 3, RetracTip was pressed by z linear stage (0.5 mm/s) and the pressing force was monitored by the loadcell. When the pressing force reached the threshold, RetracTip was then lifted to the original position, then moved to the next terrain by the x linear stage. The markers information during the whole process was recorded in the meantime, and presented in **Table** 5.1 terrain sensing section after analysis. Depending on specific terrains, the marker distribution exhibited a clear orientation difference in distribution. Compared with the original state, there are more markers in left and right and less in top and bottom for convex terrain ($\mathrm{T}, \mathrm{B} < \mathrm{T}_{ori}, \mathrm{B}_{ori}, \mathrm{L}, \mathrm{R} > \mathrm{L}_{ori}, \mathrm{R}_{ori}$), while the reverse trend for concave surface ($\mathrm{T}, \mathrm{B} > \mathrm{T}_{ori}, \mathrm{B}_{ori}, \mathrm{L}, \mathrm{R} < \mathrm{L}_{ori}, \mathrm{R}_{ori}$). For the flat surface, the markers distribute evenly in each region with a slight reduction in all regions than the natural state ($\mathrm{T}, \mathrm{B}, \mathrm{L}, \mathrm{R} < \mathrm{T}_{ori}, \mathrm{B}_{ori}, \mathrm{L}_{ori}, \mathrm{R}_{ori}$). This experiment demonstrates that RetracTip can effectively detect and differentiate different shapes and terrains.

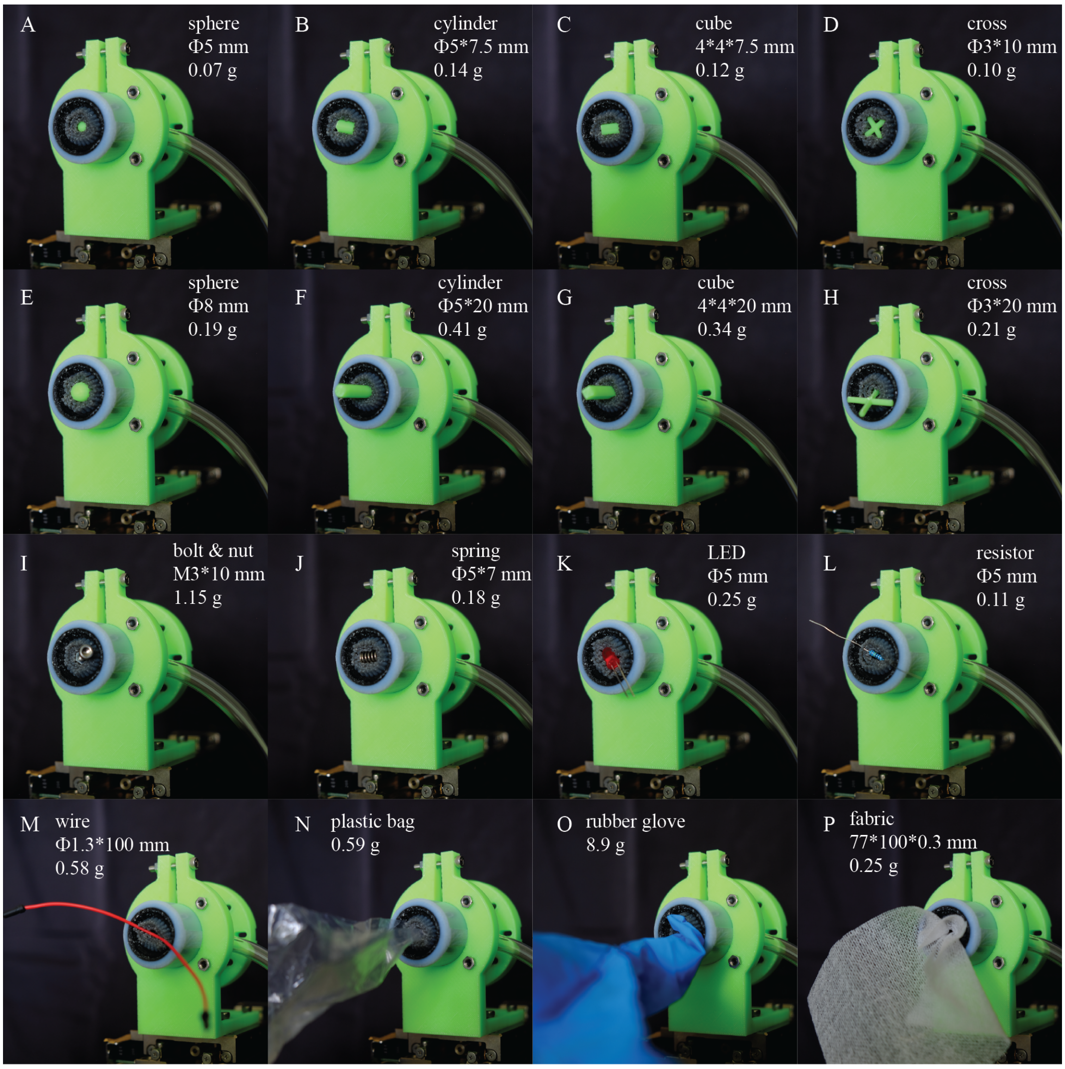
A
sphere
Φ5 mm
0.07 g
B
cylinder
Φ5*7.5 mm
0.14 g
C
cube
4*4*7.5 mm
0.12 g
D
cross
Φ3*10 mm
0.10 g
E
sphere
Φ8 mm
0.19 g
F
cylinder
Φ5*20 mm
0.41 g
G
cube
4*4*20 mm
0.34 g
H
cross
Φ3*20 mm
0.21 g
I
bolt & nut
M3*10 mm
1.15 g
J
spring
Φ5*7 mm
0.18 g
K
LED
Φ5 mm
0.25 g
L
resistor
Φ5 mm
0.11 g
M
wire
Φ1.3*100 mm
0.58 g
N
plastic bag
0.59 g
O
rubber glove
8.9 g
P
fabric
77*100*0.3 mm
0.25 g

Figure 5.7: Demonstration of gripping capability. (A) – (H) show the gripping of a series of printed objects by grasping (A) - (D) and by pinching (E) - (H). (I) – (P) present the gripping of various daily objects, from those that are rigid to those that are thin, soft and flexible.

5.4.3 Gripping

The gripping process of RetracTip is passive. When pressed against the object to trigger the snap-through behaviour, RetracTip will envelop the object by the centripetal movement of the pins on the outer membrane. Depending on the size of the objects, it can form either a complete wrap-up or a partial envelop, inducing two gripping modes (grasping mode and pinching mode, respectively) as illustrated in Fig. 5.6 A. In this section, we evaluate the gripping capability regarding the object size that can be gripped and the gripping force for both gripping modes.

Gripping size and force

In order to determine the minimum and maximum object size, we run a gripping test on a series of 3D printed spherical objects with a diameter varying from 3 mm to 12 mm by an increment of 1 mm. We chose spheres here to exclude the influence by different shapes. The testing scenario is illustrated in Fig. 5.6 B and each test was repeated ten times. The successful rate of gripping for each category was recorded in Fig. 5.6 C. The minimum diameter of a successful gripping is 4 mm, and the maximum is 10 mm considering the rate for 11 mm is relatively low. Moreover, Retractip tends to grip spheres smaller than 6 mm by grasping and those larger than that by pinching. To evaluate the gripping force for two gripping modes, we chose two spheres to represent the grasping mode (5 mm) and pinching mode (8 mm). The force was collected by the loadcell and reported in Fig. 5.6 D. The force by grasping is slightly higher than that by pinching, because intuitively it would take more energy to fall off from the complete wrap-up than from the partial envelope.

Gripping various objects

We validated the capability to grip objects of a wide range of arbitrary sizes, weights and shapes in this section, and present the result in Fig. 7. The top four subfigures (A - D) present the ability to grasp small size objects with various shapes including sphere, cylinder, cube and cross. Subfigures (E - H) report the pinching cases with larger objects, where only a small partial envelop was formed in each case. It was also tested on a series of daily components including screw and nut (1.15 g), a spring (0.18 g), a LED (0.25 g) and a resistor (0.11 g) (I - L), and on several flat and compliant materials that are a wire (0.58 g), a plastic bag (0.59 g), and rubber glove (8.9 g) and a piece of fabric (0.25 g) (M-P). We showed that RetracTip can pick up with ease and elegance all these small, delicate, compliant and flat objects that could be challenging for conventional universal grippers.

5.4.4 Friction Modulating

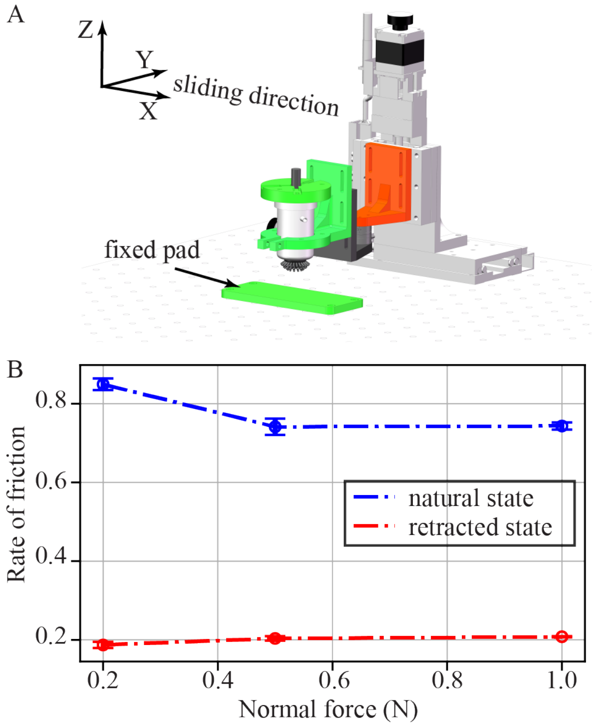

Figure 5.8: Friction modulation testing. (A) is the experimental setup and (B) presents the friction rate for two stable states of RetracTip. The friction can be tuned very effectively by selecting either.

The friction modulation is enabled by actively selecting the interacting material, either the rubber-like compliant material of dome membrane or the plastic-like rigid material of the gripper frame, with environment. In order to quantitively verify such possibility, we performed this test to measure the friction coefficient under both states. Specifically as shown in **supplementary video** 3 and Fig. 5.8 A, RetracTip was controled to slide under two stable states individually against a 3D printed ABS flat surface. The initial vertical force was specified as 0.2 N, 0.5 N and 1.0 N and controlled by the loadcell, and the horizontal force was recorded during sliding by the same sensor. Each slikding was repeated by 3 times. The data is analysed and plotted in Fig. 5.8 B. The average coefficient values are 0.894 ± 0.015, 0.741 ± 0.021 and 0.743 ± 0.009 for the natural state, and 0.187 ± 0.008, 0.204 ± 0.006 and 0.208 ± 0.001 for the retracted state, demonstrating very efficient friction modulation capability which can be potentially useful for scenarios such as active manipulation.

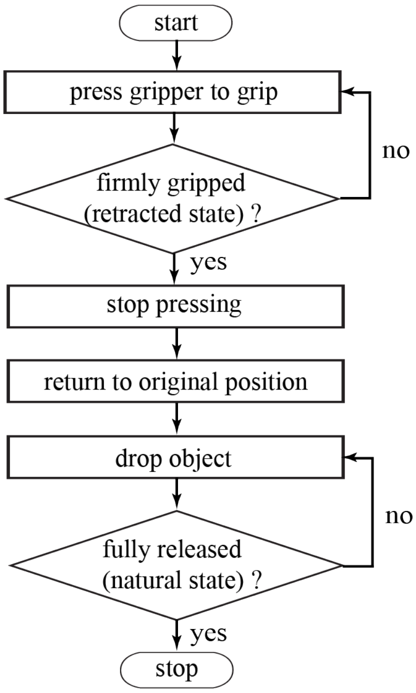
start
press gripper to grip
no
firmly gripped
(retracted state) ?
yes
stop pressing
return to original position
drop object
no
fully released
(natural state) ?
yes
stop

Figure 5.9: The control flowchart of the RetracTip control system.

5.4.5 Autonomous Gripping Control

Up to now, we have tested the main functionalities of RetracTip separately. Here, we demonstrate a case study for autonomous gripping control, in which we used the integrated tactile sensor to first sense and perceive the gripping condition and then to feedback to the controller in order to determine next move. The control flowchart of this process is shown in Fig. 5.9. The demonstration is presented in **supplementary video** 4. Specifically, RetracTip was pressed against a cylinder to grip while monitoring the gripping condition by the sensing functionality. Once a snap-through of the membrane that assures a firm gripping was detected, the system will stop going down, returned to the initial position before dropping the object. By such a simple demonstration we showed the great potential of our compact universal gripper design towards a fully autonomous gripping system.

5.5 Discussion

The mechanical design is key to shape the functionality of RetracTip. Particularly there is a trade-off relationship between the functions of gripping and friction modulation, which exhibit when varying the depth of cap (H) and the length of pins (L). As illustrated in

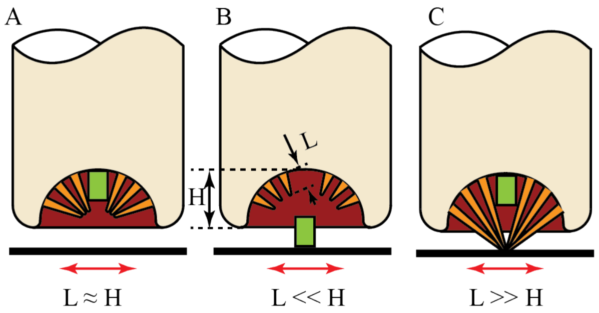

condition	L ≈ H	L << H	L >> H
gripping function	√	×	√
friction modulation	√	√	×

Figure 5.10: The trade-off relationship between two functionalities (gripping and friction modulating) induced by the variance of pin length (L) and membrane depth (H). Both functionalities can be achieved simultaneously only when a suitable ratio of the two parameters (L, H) is selected as in (A).

Fig. 5.10, both functionalities can be achieved at the same time when L is approximately equal to H. The case where L is far greater or far smaller than H will always lose either of the two functions.

Apart from the passive gripping that has been verified in this article, RetracTip can potentially realize active gripping as well by vacuuming the gripper when approaching the target. While the active gripping may yield a safer interaction between the membrane and the object as no hard contact is required to active the snap-through, it will need a precise control to ensure a firm grasp with a sufficient part of the object immersed in the pin envelope.

The design of the makers inside the dome membrane influence the sensing functionality. For example, the size and layout of the markers determine the separability of them and stability of data extraction in the image processing. RetracTip has been demonstrated to be capable of both proprioceptive and exteroceptive sensing. However, to achieve sensing that is robust and accurate, the marker designs need to be optimized and advanced sensing algorithms need to be explored.

RetracTip is tested in this article as an end effector capable of sensing, gripping and friction modulation. Inspired by the terrain sensing capability, RetracTip can also potentially be used as a robotic foot that can provide tactile sensing for terrain based control strategy.

The energy efficiency of the gripper need to be properly characterzied in order to reveal the benefit of the bistable design. A possible solution could be to compare the energy consumption performance with that of a similar but monostable design.

The bistability of the dome membrane was analyzed in terms of the depth of the structure. There are more parameters affecting this property actually, for example, the thickness, the dimension of the rim, and the existence of the pins etc. More detailed analysis need to done thoroughly in the future to understand the bistable behavior.

Compared with the jamming gripper [14, 119], RetracTip overcomes one key limitation by integrating both proprioceptive and exteroceptive sensing functionality enabling it to sense the self and external state. Another advantage is the improved energy efficiency during holding objects. Jamming gripper needs to keep pressurized to maintain the gripping force while RetracTip eliminates this need by using the bistable dome membrane. One concern, however, is that RetracTip will suffer to control the griping force actively as it mainly operates in the passive gripping mode, as mentioned earlier. Future plan involves testing if the active gripping mode can realize the gripping force control.

Regarding the sensing functionality, very preliminary demonstrations have been done in this thesis. Finer sensing algorithms need to be developed for real applications such as object localization, object detection, and object shape detection.

5.6 Conclusion

Multifunctionality and energy efficiency are two preferences for autonomous soft robots as such robots can potentially achieve multiple vital functions with a simple and lightweight structure and can survive longer with limited power supply. While most previous researches on soft robotic grippers (RetracTip) focused on enhancing the multifunctionality, we proposed a sea-anemone-inspired compact universal gripper with improved energy efficiency and multiple functionalities including sensing (proprioceptive and exteroceptive), multimodal gripping (grasping and pinching) and friction modulating. The energy efficiency was improved by eliminating the need for continuous energy input to hold objects thanks to the intrinsic bistability. For verification, we have simulated the bistability of RetracTip and demonstrated the multiple functionalities both individually and jointly by separate testing on each and a final demonstration of autonomous gripping control.

The contributions of this work include: (1) the first proposal of a bionic universal gripper with both augmented multifunctionality and improved energy efficiency, (2) the creative implementation of a bistable dome membrane to eliminate the continuous energy requirement for holding objects, and (3) the construction and demonstration of an autonomous gripping system with a hierarchical control regime. In summary, this work delivers an excellent example for bioinspired gripper that mimicking both the structure and action of the biology analog, and is expected to pave the way for soft robotic design aiming to improve multifunctionality and energy efficiency simultaneously.

Chapter 6

Conclusions and Outlook

This thesis studies the beneficial effect of adaptive morphology on soft robotics via the research work on two prototypes, a soft tactile sensor "WrinTac" and a multifunctional soft gripper "RetracTip". Within both samples, adaptive morphology was incorporated appropriately in order to enable adjustable behaviour accordingly. A few case studies are given in Chapter 3 – 5, demonstrating that adaptive morphology are beneficial not only to sensing and perception, but also to actuation, gripping for example. While the underlying mechanism for such enhancement remains not fully revealed, it was speculated to be the stiffness and shape changes that have led to the variations.

In this chapter, it first summarizes the contributions of this study by revisiting some key points argued in previous chapters. Then the conclusion with insights is drawn in order to bring this study to the interests of a wider community. Finally, it speculates and points out the future work that needs to be done.

6.1 Summary of Contributions

Overall, the exploration of adaptive morphology of soft sensors and grippers in this study provides a comprehensive and pioneer work looking into how variable and adaptable morphology can facilitate sensing and gripping function of soft robotics. It demonstrates the great potential of adaptive morphology to enable soft robots with more complex behaviours and optimized performance such as extended sensing range and operational space and improved energy efficiency, which are all vital requirements for future autonomous soft machines expected to work in ever-changing, complex and unstructured environment. Specifically, the numerous contributions of each chapter are summarized in detail here.

Apart from the demonstration of beneficial influence of adaptive morphology on tactile sensing, we, for the first time, integrates the wrinkle morphology that is variable into the design of a soft tactile sensor with a multilayer structure in chapter 3. This adaptive morphology, once stretched, varies its few key parameters while still remains in the basic wrinkled form, providing a novel integration of adaptive morphology. In order to understand the wrinkle morphology, we proposed a simplified analytical model, that differs from the complex modelling methodology in the literature, to describe the wrinkling behaviour of such design. By doing so, the fabrication process was verified and characterized in terms of repeatability and basic property of the formed wrinkle structure such as the number of waves.

The effect of adaptive morphology on soft tactile sensing was further evaluated based on WrinTac actuated by bending in chapter 4. It was found that the performance of two different tasks, shape classification and texture detection, can be tuned by the changing morphology, and an morphological optimizing process existed for each task. Moreover, the adaptive behaviour of the wrinkle structure was modelled analytically by a approximating approach, exhibiting good predictability of the morphing ability. It is proposed through the work on WrinTac that active sensing could be achieved by adapting the sensor morphology to specific task, which is believed to be computationally more costly, rather than by coordinating the sensory motor activity of the sensing systems conventionally.

Having shown that adaptive morphology can be utilised to facilitate sensing functionality, it was also found to be effective in tuning the actuation of soft robotics [21]. This could happen in many ways such as enabling new functions and extending operational space. In chapter 5, this idea was demonstrated by RetracTip, a multifunctional soft gripper with improved energy efficiency. The gripping capability was enabled by the integration of an adaptive pinned morphing membrane. Because of the same morphology, the power required was largely reduced by eliminating the power needed during holding an object. When applied properly, adaptive morphology could potentially be explored for a larger variety of behaviours for soft robotics.

6.2 Conclusions

Soft robotics has the potential to be integrated into human life ubiquitously and seamlessly. While existing soft robots are predominantly designed with particularly specific tasks, for example sensing, actuation (locomotion, grasping, transportation etc.), perception, or computing, those with multiple functions and capabilities are in the need. Such robots can operate in different environments and do not necessarily need to be constrained to specific tasks. They show robustness and resilience to the unpredictable surrounding them, and, even if they fail, cause no detrimental harm to agents within their proximity because of their inherent softness.

Adaptive morphology offers a promising design philosophy for such soft robots. It exploits the embodied intelligence by considering jointly the morphology, by which we refer to the geometrical and material property, and the environmental interactions in order to achieve more complex and adaptive behaviours. This has been demonstrated by the presented work in this study. This framework, however, complicates the design process as more dimensions are to be considered and co-designed. Nonetheless, the design complexity would be rewarded by the resultant robots.

Biology always provides a starting point to search for a proper morphology for a given target function. For example, the wrinkle morphology on human fingertips and the retract morphing structure of sea anemone in this study. However, no biological samples should be simply copied artificially without considering the target functions, the material, and the manufacturing techniques. Care should be paid to the driving methodology to make morphology adaptive actively in addition to the system actuation. The trade-off between the multifunctionality realized by adaptive morphology and the complexity induced by the extra actuation for adaptive morphology needs to be addressed appropriately.

6.3 Outlook

Adaptive morphology has been demonstrated to be effectively beneficial for soft robotics. To further extend this work toward achieving soft robots with robustness, adaptivity, autonomy, energy efficiency and other life-like functionalities, several directions are discussed here for investigation in the future.

Sensing, actuation, and computation are three fundamental components functions for soft robots to operate in the real world. In the integrated view of embodiment, each and every functionality of soft robotics can be shaped by their body morphology. While initial investigations of adaptive morphology into the former two components (sensing and actuation) are beginning lately, more focus on the computing side is needed in order to understand how morphology affect the behaviours of robot as a whole. Based on the fundamental understandings about the function-morphology relation, more appropriate body morphology can be expected for soft robotics that can suits better to the dynamic environment with improved adaptivity and autonomy.

Advanced understanding for the role of morphology forms the basis in order to master it in soft robotic design. Although traditional trail and error manner offers a practical approach for such purpose, it is expensive and even unaffordable in some occasions. Modelling and physical simulation are two cheaper manners. For example, the modelling of the body dynamics. The concerns are how the simplification is assumed and to what extent they reflect the reality. In this sense, the modelling and simulation of adaptive morphology are required to help for design. For example, modelling of the dynamic behaviour of adaptive morphology in soft actuator, and quantification of the information gain of adaptive morphology in soft sensor.

Actuators are necessary to enable the variation of a specific morphology, for example the stretching and bending actuation of WrinTac and thee pneumatic actuation for RetracTip. This requirement, to some extent, increases the complexity and cost of the system. Novel actuation needs to be investigated for this purpose. A viable solution might be to use existing actuators in the system for the adaptable morphology. More investigation need to done in the future.

WrinTac

The wrinkle morphology was found to be an effective adaptive morphology. Different mechanisms and materials could be explored. For example, dielectric elastomer actuator (DEA) with fix boundary can generate out of plane wrinkle-like structure.

Sensor morphology as an intelligent source has been explored mainly in two areas, vision and touch, because both involve environmental interactions frequently. More sensing modalities could be considered from the viewpoint of embodied intelligence to introduce adaptive morphology enabling variable sensing capability.

A general calibration system can be proposed for WrinTac to tackle the material degradation problem that all soft sensors are experiencing. The system should be able to run autonomously to calibration the force stimuli from different directions, for example vertical and horizontal. This will require, as a minimum, a driving subsystem, a loadcell subsystem, and the corresponding control and data processing algorithms.

A potential application is an active sensing system as envisaged in Fig. 4.1. The WrinTac will be integrated in a robotic finger that can bend the sensor. When put into different environments, the system can actively morph for optimal performance. In this case, more advanced algorithms need to be proposed for WrinTac based on the preliminary investigation. For example, algorithms for shape classification under more complex situations such as variable speed and pressing pressure. A very key consideration for such purpose might be to take the information encoded in the time series signal into account as, for example, human rely much on the dynamic rather than static signal for tactile exploration.

RetracTip

RetracTip has been tested regarding its basic functionality claimed, that is sensing, gripping and variable friction. More application scenario will be proposed to demonstrate the capability and potential of this design. For example, an autonomous gripping system that detects and localizes objects, adjusts the self posture, picks objects and places them to the target place. Another example will be to use RetracTip as a robotic foot for sensorized locomotion. The foot can vary its friction property according to different requirement by multiple terrains.

The bistability of the dome membrane has been simulated and analyzed by FEM modeling. It is found that the bistability of the structure is affected by the adding of the pins. More detailed analysis need to be done for other geometrical factors. The static and dynamic behaviors of the bistable dome under different actuation will be thoroughly modeled in the future. These two properties are key to the energy cost of the structure, which can hopefully be modeled and predicted based on the static and dynamic modeling. The structure can then be optimized for improved performance in terms of, for example, energy efficiency.

Bibliography

[1] M. Garrad, G. Soter, A. Conn, H. Hauser, and J. Rossiter, "A soft matter computer for soft robots," *Science Robotics*, vol. 4, no. 33, 2019.

[2] Q. Qi, S. Hirai, *et al.*, "Wrinkled soft sensor with variable afferent morphology," *IEEE Robotics and Automation Letters*, vol. 4, no. 2, pp. 1908–1915, 2019.

[3] B. Erlendur, C. Michael, and P. Halldórsson, "Sea anemone."

[4] E. Guizzo, "What is a robot," 2018.

[5] C. Laschi, B. Mazzolai, and M. Cianchetti, "Soft robotics: Technologies and systems pushing the boundaries of robot abilities," *Science Robotics*, vol. 1, no. 1, p. eaah3690, 2016.

[6] M. A. K. Bahrin, M. F. Othman, N. H. N. Azli, and M. F. Talib, "Industry 4.0: A review on industrial automation and robotic," *Jurnal Teknologi*, vol. 78, no. 6-13, 2016.

[7] E. Broadbent, R. Stafford, and B. MacDonald, "Acceptance of healthcare robots for the older population: Review and future directions," *International journal of social robotics*, vol. 1, no. 4, p. 319, 2009.

[8] M. M. Veloso, "Entertainment robotics," *Communications of the ACM*, vol. 45, no. 3, pp. 59–63, 2002.

[9] R. Pfeifer, M. Lungarella, and F. Iida, "The challenges ahead for bio-inspired'soft'robotics," *Communications of the ACM*, vol. 55, no. 11, pp. 76–87, 2012.

[10] D. Rus and M. T. Tolley, "Design, fabrication and control of soft robots," *Nature*, vol. 521, no. 7553, pp. 467–475, 2015.

[11] M. A. McEvoy and N. Correll, "Materials that couple sensing, actuation, computation, and communication," *Science*, vol. 347, no. 6228, 2015.

[12] D. Howard, A. E. Eiben, D. F. Kennedy, J.-B. Mouret, P. Valencia, and D. Winkler, "Evolving embodied intelligence from materials to machines," *Nature Machine Intelligence*, vol. 1, no. 1, pp. 12–19, 2019.

[13] R. Pfeifer, M. Lungarella, and F. Iida, "Self-organization, embodiment, and biologically inspired robotics," *science*, vol. 318, no. 5853, pp. 1088–1093, 2007.

[14] E. Brown, N. Rodenberg, J. Amend, A. Mozeika, E. Steltz, M. R. Zakin, H. Lipson, and H. M. Jaeger, "Universal robotic gripper based on the jamming of granular material," *Proceedings of the National Academy of Sciences*, vol. 107, no. 44, pp. 18809–18814, 2010.

[15] R. Pfeifer, F. Iida, and G. Gómez, "Morphological computation for adaptive behavior and cognition," in *International Congress Series*, vol. 1291, pp. 22–29, Elsevier, 2006.

[16] F. Iida and S. G. Nurzaman, "Adaptation of sensor morphology: an integrative view of perception from biologically inspired robotics perspective," *Interface focus*, vol. 6, no. 4, p. 20160016, 2016.

[17] J. E. Bernth, V. A. Ho, and H. Liu, "Morphological computation in haptic sensation and interaction: from nature to robotics," *Advanced Robotics*, vol. 32, no. 7, pp. 340–362, 2018.

[18] Y.-F. Zhang, N. Zhang, H. Hingorani, N. Ding, D. Wang, C. Yuan, B. Zhang, G. Gu, and Q. Ge, "Fast-response, stiffness-tunable soft actuator by hybrid multimaterial 3d printing," *Advanced Functional Materials*, vol. 29, no. 15, p. 1806698, 2019.

[19] J. Hughes, U. Culha, F. Giardina, F. Guenther, A. Rosendo, and F. Iida, "Soft manipulators and grippers: a review," *Frontiers in Robotics and AI*, vol. 3, p. 69, 2016.

[20] H. Hauser, "Resilient machines through adaptive morphology," *Nature Machine Intelligence*, vol. 1, no. 8, pp. 338–339, 2019.

[21] S. Mintchev and D. Floreano, "Adaptive morphology: A design principle for multimodal and multifunctional robots," *IEEE Robotics & Automation Magazine*, vol. 23, no. 3, pp. 42–54, 2016.

[22] K. Oliver, A. Seddon, and R. S. Trask, "Morphing in nature and beyond: a review of natural and synthetic shape-changing materials and mechanisms," *Journal of Materials Science*, vol. 51, no. 24, pp. 10663–10689, 2016.

[23] D. Shah, B. Yang, S. Kriegman, M. Levin, J. Bongard, and R. Kramer-Bottiglio, “Shape changing robots: Bioinspiration, simulation, and physical realization,” *Advanced Materials*, p. 2002882, 2020.

[24] M. Manti, V. Cacucciolo, and M. Cianchetti, “Stiffening in soft robotics: A review of the state of the art,” *IEEE Robotics & Automation Magazine*, vol. 23, no. 3, pp. 93–106, 2016.

[25] H. Hauser and F. Corucci, “Morphosis—taking morphological computation to the next level,” in *Soft Robotics: Trends, Applications and Challenges*, pp. 117–122, Springer, 2017.

[26] R. Pfeifer and J. Bongard, *How the body shapes the way we think: a new view of intelligence*. MIT press, 2006.

[27] D. Lentink, U. Müller, E. Stamhuis, R. De Kat, W. Van Gestel, L. Veldhuis, P. Henningsson, A. Hedenström, J. J. Videler, and J. L. Van Leeuwen, “How swifts control their glide performance with morphing wings,” *Nature*, vol. 446, no. 7139, pp. 1082–1085, 2007.

[28] D. Falanga, K. Kleber, S. Mintchev, D. Floreano, and D. Scaramuzza, “The foldable drone: A morphing quadrotor that can squeeze and fly,” *IEEE Robotics and Automation Letters*, vol. 4, no. 2, pp. 209–216, 2018.

[29] J. Sun and J. Zhao, “An adaptive walking robot with reconfigurable mechanisms using shape morphing joints,” *IEEE Robotics and Automation Letters*, vol. 4, no. 2, pp. 724–731, 2019.

[30] B. Vanderborght, A. Albu-Schäffer, A. Bicchi, E. Burdet, D. G. Caldwell, R. Carloni, M. Catalano, O. Eiberger, W. Friedl, G. Ganesh, *et al.*, “Variable impedance actuators: A review,” *Robotics and autonomous systems*, vol. 61, no. 12, pp. 1601–1614, 2013.

[31] S. Wolf, G. Grioli, O. Eiberger, W. Friedl, M. Grebenstein, H. Höppner, E. Burdet, D. G. Caldwell, R. Carloni, M. G. Catalano, *et al.*, “Variable stiffness actuators: Review on design and components,” *IEEE/ASME transactions on mechatronics*, vol. 21, no. 5, pp. 2418–2430, 2015.

[32] K. Oliver, A. Seddon, and R. S. Trask, “Morphing in nature and beyond: a review of natural and synthetic shape-changing materials and mechanisms,” *Journal of Materials Science*, vol. 51, no. 24, pp. 10663–10689, 2016.

[33] R. A. Grant, B. Mitchinson, C. W. Fox, and T. J. Prescott, “Active touch sensing in the rat: anticipatory and regulatory control of whisker movements during surface exploration,” *Journal of neurophysiology*, vol. 101, no. 2, pp. 862–874, 2009.

[34] R. L. Baines, J. W. Booth, F. E. Fish, and R. Kramer-Bottiglio, “Toward a bio-inspired variable-stiffness morphing limb for amphibious robot locomotion,” in *2019 2nd IEEE International Conference on Soft Robotics (RoboSoft)*, pp. 704–710, IEEE, 2019.

[35] D. S. Shah, M. C. Yuen, L. G. Tilton, E. J. Yang, and R. Kramer-Bottiglio, “Morphing robots using robotic skins that sculpt clay,” *IEEE Robotics and Automation Letters*, vol. 4, no. 2, pp. 2204–2211, 2019.

[36] E. Hawkes, B. An, N. M. Benbernou, H. Tanaka, S. Kim, E. D. Demaine, D. Rus, and R. J. Wood, “Programmable matter by folding,” *Proceedings of the National Academy of Sciences*, vol. 107, no. 28, pp. 12441–12445, 2010.

[37] D.-Y. Lee, S.-R. Kim, J.-S. Kim, J.-J. Park, and K.-J. Cho, “Origami wheel transformer: A variable-diameter wheel drive robot using an origami structure,” *Soft robotics*, vol. 4, no. 2, pp. 163–180, 2017.

[38] K. Suzumori, S. Wakimoto, K. Miyoshi, and K. Iwata, “Long bending rubber mechanism combined contracting and extending tluidic actuators,” in *2013 IEEE/RSJ International Conference on Intelligent Robots and Systems*, pp. 4454–4459, IEEE, 2013.

[39] M. Cianchetti, M. Calisti, L. Margheri, M. Kuba, and C. Laschi, “Bioinspired locomotion and grasping in water: the soft eight-arm octopus robot,” *Bioinspiration & biomimetics*, vol. 10, no. 3, p. 035003, 2015.

[40] M. Brancadoro, M. Manti, S. Tognarelli, and M. Cianchetti, “Fiber jamming transition as a stiffening mechanism for soft robotics,” *Soft Robotics*, 2020.

[41] M. Ibrahimi, L. Paternò, L. Ricotti, and A. Menciassi, “A layer jamming actuator for tunable stiffness and shape-changing devices,” *Soft Robotics*, 2020.

[42] T. Miller Jackson, Y. Sun, R. Natividad, and C. H. Yeow, “Tubular jamming: A variable stiffening method toward high-force applications with soft robotic components,” *Soft robotics*, vol. 6, no. 4, pp. 468–482, 2019.

[43] C. Majidi and R. J. Wood, “Tunable elastic stiffness with microconfined magnetorheological domains at low magnetic field,” *Applied Physics Letters*, vol. 97, no. 16, p. 164104, 2010.

[44] C. Cao and X. Zhao, “Tunable stiffness of electrorheological elastomers by designing mesostructures,” *Applied Physics Letters*, vol. 103, no. 4, p. 041901, 2013.

[45] N. G. Cheng, A. Gopinath, L. Wang, K. Iagnemma, and A. E. Hosoi, "Thermally tunable, self-healing composites for soft robotic applications," *Macromolecular Materials and Engineering*, vol. 299, no. 11, pp. 1279–1284, 2014.

[46] R. F. Shepherd, F. Ilievski, W. Choi, S. A. Morin, A. A. Stokes, A. D. Mazzeo, X. Chen, M. Wang, and G. M. Whitesides, "Multigait soft robot," *Proceedings of the national academy of sciences*, vol. 108, no. 51, pp. 20400–20403, 2011.

[47] B. Aktas and R. D. Howe, "Flexure mechanisms with variable stiffness and damping using layer jamming," in *Proceedings of the IEEERSJ International Conference on Intelligent Robots and Systems*, 2019.

[48] Y. Yang, Z. Kan, Y. Zhang, Y. A. Tse, and M. Y. Wang, "A novel variable stiffness actuator based on pneumatic actuation and supercoiled polymer artificial muscles," in *2019 International Conference on Robotics and Automation (ICRA)*, pp. 3983–3989, IEEE, 2019.

[49] M. Zhu, Y. Mori, T. Wakayama, A. Wada, and S. Kawamura, "A fully multi-material three-dimensional printed soft gripper with variable stiffness for robust grasping," *Soft robotics*, vol. 6, no. 4, pp. 507–519, 2019.

[50] Y. Jiang, D. Chen, C. Liu, and J. Li, "Chain-like granular jamming: a novel stiffness-programmable mechanism for soft robotics," *Soft robotics*, vol. 6, no. 1, pp. 118–132, 2019.

[51] J. Sun, B. Pawlowski, and J. Zhao, "Embedded and controllable shape morphing with twisted-and-coiled actuators," in *2018 IEEE/RSJ International Conference on Intelligent Robots and Systems (IROS)*, pp. 5912–5917, IEEE, 2018.

[52] T. L. Buckner, E. L. White, M. C. Yuen, R. A. Bilodeau, and R. K. Kramer, "A move-and-hold pneumatic actuator enabled by self-softening variable stiffness materials," in *2017 IEEE/RSJ International Conference on Intelligent Robots and Systems (IROS)*, pp. 3728–3733, IEEE, 2017.

[53] W. Ruotolo, F. S. Roig, and M. R. Cutkosky, "Load-sharing in soft and spiny paws for a large climbing robot," *IEEE Robotics and Automation Letters*, vol. 4, no. 2, pp. 1439–1446, 2019.

[54] S. J. Lederman and R. L. Klatzky, "Haptic perception: A tutorial," *Attention, Perception, & Psychophysics*, vol. 71, no. 7, pp. 1439–1459, 2009.

[55] R. S. Dahiya, G. Metta, M. Valle, and G. Sandini, "Tactile sensing—from humans to humanoids," *IEEE transactions on robotics*, vol. 26, no. 1, pp. 1–20, 2009.

[56] C. M. Oddo, L. Beccai, J. Wessberg, H. B. Wasling, F. Mattioli, and M. C. Carrozza, "Roughness encoding in human and biomimetic artificial touch: Spatiotemporal frequency modulation and structural anisotropy of fingerprints," *Sensors*, vol. 11, no. 6, pp. 5596–5615, 2011.

[57] G. Vásárhelyi, B. Fodor, and T. Roska, "Tactile sensing-processing: Interface-cover geometry and the inverse-elastic problem," *Sensors and Actuators A: Physical*, vol. 140, no. 1, pp. 8–18, 2007.

[58] D. Yamada, T. Maeno, and Y. Yamada, "Artificial finger skin having ridges and distributed tactile sensors used for grasp force control," in *Proceedings 2001 IEEE/RSJ International Conference on Intelligent Robots and Systems. Expanding the Societal Role of Robotics in the the Next Millennium (Cat. No. 01CH37180)*, vol. 2, pp. 686–691, IEEE, 2001.

[59] S. G. Nurzaman, U. Culha, L. Brodbeck, L. Wang, and F. Iida, "Active sensing system with in situ adjustable sensor morphology," *PLoS One*, vol. 8, no. 12, p. e84090, 2013.

[60] S. Hirose, S. Inoue, and K. Yoneda, "The whisker sensor and the transmission of multiple sensor signals," *Advanced Robotics*, vol. 4, no. 2, pp. 105–117, 1989.

[61] R. A. Russell, "Using tactile whiskers to measure surface contours," in *Proceedings 1992 IEEE International Conference on Robotics and Automation*, pp. 1295–1296, IEEE Computer Society, 1992.

[62] M. Lungarella, V. V. Hafner, R. Pfeifer, and H. Yokoi, "An artificial whisker sensor for robotics," in *IEEE/RSJ International Conference on Intelligent Robots and Systems*, vol. 3, pp. 2931–2936, IEEE, 2002.

[63] J. H. Solomon and M. J. Hartmann, "Robotic whiskers used to sense features," *Nature*, vol. 443, no. 7111, pp. 525–525, 2006.

[64] D. Kim and R. Möller, "Passive sensing and active sensing of a biomimetic whisker," in *International Conference on the Simulation and Synthesis of Living Systems*, vol. 131, Bloomington: Indiana University Press, 2006.

[65] G. R. Scholz and C. D. Rahn, "Profile sensing with an actuated whisker," *IEEE Transactions on Robotics and Automation*, vol. 20, no. 1, pp. 124–127, 2004.

[66] M. J. Pearson, B. Mitchinson, J. C. Sullivan, A. G. Pipe, and T. J. Prescott, "Biomimetic vibrissal sensing for robots," *Philosophical Transactions of the Royal Society B: Biological Sciences*, vol. 366, no. 1581, pp. 3085–3096, 2011.

[67] M. J. Pearson, B. Mitchinson, J. Welsby, T. Pipe, and T. J. Prescott, “Scratchbot: Active tactile sensing in a whiskered mobile robot,” in *International Conference on Simulation of Adaptive Behavior*, pp. 93–103, Springer, 2010.

[68] K. Nakajima, H. Hauser, T. Li, and R. Pfeifer, “Information processing via physical soft body,” *Scientific reports*, vol. 5, p. 10487, 2015.

[69] K. Nakajima, H. Hauser, R. Kang, E. Guglielmino, D. G. Caldwell, and R. Pfeifer, “A soft body as a reservoir: case studies in a dynamic model of octopus-inspired soft robotic arm,” *Frontiers in computational neuroscience*, vol. 7, p. 91, 2013.

[70] K. Nakajima, T. Li, H. Hauser, and R. Pfeifer, “Exploiting short-term memory in soft body dynamics as a computational resource,” *Journal of The Royal Society Interface*, vol. 11, no. 100, p. 20140437, 2014.

[71] K. Nakajima, H. Hauser, T. Li, and R. Pfeifer, “Exploiting the dynamics of soft materials for machine learning,” *Soft robotics*, vol. 5, no. 3, pp. 339–347, 2018.

[72] J. Kuwabara, K. Nakajima, R. Kang, D. T. Branson, E. Guglielmino, D. G. Caldwell, and R. Pfeifer, “Timing-based control via echo state network for soft robotic arm,” in *The 2012 International Joint Conference on Neural Networks (IJCNN)*, pp. 1–8, IEEE, 2012.

[73] S. T. Mahon, A. Buchoux, M. E. Sayed, L. Teng, and A. A. Stokes, “Soft robots for extreme environments: Removing electronic control,” in *2019 2nd IEEE International Conference on Soft Robotics (RoboSoft)*, pp. 782–787, IEEE, 2019.

[74] J. Hughes and F. Iida, “Localized differential sensing of soft deformable surfaces,” in *2017 IEEE International Conference on Robotics and Automation (ICRA)*, p-p. 4959–4964, IEEE, 2017.

[75] H. Zhao, K. O’Brien, S. Li, and R. F. Shepherd, “Optoelectronically innervated soft prosthetic hand via stretchable optical waveguides,” *Science robotics*, vol. 1, no. 1, 2016.

[76] B. S. Homberg, R. K. Katzschmann, M. R. Dogar, and D. Rus, “Haptic identification of objects using a modular soft robotic gripper,” in *2015 IEEE/RSJ International Conference on Intelligent Robots and Systems (IROS)*, pp. 1698–1705, IEEE, 2015.

[77] V. C. Müller and M. Hoffmann, “What is morphological computation? on how the body contributes to cognition and control,” *Artificial life*, vol. 23, no. 1, pp. 1–24, 2017.

[78] V. Ho, H. Yamashita, Z. Wang, S. Hirai, and K. Shibuya, "Wrin'tac: Tactile sensing system with wrinkle's morphological change," *IEEE Transactions on Industrial Informatics*, vol. 13, no. 5, pp. 2496–2506, 2017.

[79] A. D. Hinitt, J. Rossiter, and A. T. Conn, "Wormtip: An invertebrate inspired active tactile imaging pneumostat," in *Conference on Biomimetic and Biohybrid Systems*, pp. 38–49, Springer, 2015.

[80] S. Ozel, E. H. Skorina, M. Luo, W. Tao, F. Chen, Y. Pan, and C. D. Onal, "A composite soft bending actuation module with integrated curvature sensing," in *2016 IEEE International Conference on Robotics and Automation (ICRA)*, pp. 4963–4968, IEEE, 2016.

[81] R. Xu, A. Yurkewich, and R. V. Patel, "Curvature, torsion, and force sensing in continuum robots using helically wrapped fbg sensors," *IEEE Robotics and Automation Letters*, vol. 1, no. 2, pp. 1052–1059, 2016.

[82] Y. L. Park, B. R. Chen, and R. J. Wood, "Design and fabrication of soft artificial skin using embedded microchannels and liquid conductors," *IEEE Sensors journal*, vol. 12, no. 8, pp. 2711–2718, 2012.

[83] J. B. Chossat, Y. L. Park, R. J. Wood, and V. Duchaine, "A soft strain sensor based on ionic and metal liquids," *Ieee sensors journal*, vol. 13, no. 9, pp. 3405–3414, 2013.

[84] U. Culha, U. Wani, S. G. Nurzaman, F. Clemens, and F. Iida, "Motion pattern discrimination for soft robots with morphologically flexible sensors," in *2014 IEEE/RSJ International Conference on Intelligent Robots and Systems*, pp. 567–572, IEEE, 2014.

[85] R. Reep and D. K. Sarko, "Tactile hair in manatees," *Scholarpedia*, vol. 4, no. 4, p. 6831, 2009.

[86] N. F. Lepora, M. Evans, C. W. Fox, M. E. Diamond, K. Gurney, and T. J. Prescott, "Naive bayes texture classification applied to whisker data from a moving robot," in *The 2010 International Joint Conference on Neural Networks (IJCNN)*, pp. 1–8, IEEE, 2010.

[87] E. P. Chan, E. J. Smith, R. C. Hayward, and A. J. Crosby, "Surface wrinkles for smart adhesion," *Advanced Materials*, vol. 20, no. 4, pp. 711–716, 2008.

[88] D. Y. Khang, J. A. Rogers, and H. H. Lee, "Mechanical buckling: mechanics, metrology, and stretchable electronics," *Advanced Functional Materials*, vol. 19, no. 10, pp. 1526–1536, 2009.

[89] E. P. Chan and A. J. Crosby, "Fabricating microlens arrays by surface wrinkling," *Advanced Materials*, vol. 18, no. 24, pp. 3238–3242, 2006.

[90] Q. Wang and X. Zhao, "A three-dimensional phase diagram of growth-induced surface instabilities," *Scientific reports*, vol. 5, no. 1, pp. 1–10, 2015.

[91] E. Cerda and L. Mahadevan, "Geometry and physics of wrinkling," *Physical review letters*, vol. 90, no. 7, p. 074302, 2003.

[92] H. Wakamatsu and S. Hirai, "Static modeling of linear object deformation based on differential geometry," *The International Journal of Robotics Research*, vol. 23, no. 3, pp. 293–311, 2004.

[93] H. Singh, D. Popov, I. Gaponov, and J. H. Ryu, "Twisted string-based passively variable transmission: Concept, model, and evaluation," *Mechanism and Machine Theory*, vol. 100, pp. 205–221, 2016.

[94] D. Kleinfeld, E. Ahissar, and M. E. Diamond, "Active sensation: insights from the rodent vibrissa sensorimotor system," *Current opinion in neurobiology*, vol. 16, no. 4, pp. 435–444, 2006.

[95] M. Fend, H. Yokoi, and R. Pfeifer, "Optimal morphology of a biologically-inspired whisker array on an obstacle-avoiding robot," in *European Conference on Artificial Life*, pp. 771–780, Springer, 2003.

[96] M. Fend, R. Abt, M. Diefenbacher, S. Bovet, and M. Krafft, "Morphology and learning-a case study on whiskers," in *Proc. 8th Int. Conf. on the Simulation of Adaptive Behavior*, pp. 114–122, 2004.

[97] J. Scheibert, S. Leurent, A. Prevost, and G. Debrégeas, "The role of fingerprints in the coding of tactile information probed with a biomimetic sensor," *Science*, vol. 323, no. 5920, pp. 1503–1506, 2009.

[98] L. Cramphorn, B. Ward-Cherrier, and N. F. Lepora, "Addition of a biomimetic fingerprint on an artificial fingertip enhances tactile spatial acuity," *IEEE Robotics and Automation Letters*, vol. 2, no. 3, pp. 1336–1343, 2017.

[99] T. J. Prescott, M. E. Diamond, and A. M. Wing, "Active touch sensing," 2011.

[100] M. Hollins, S. Bensmaıa, and E. Roy, "Vibrotaction and texture perception," *Behavioural brain research*, vol. 135, no. 1-2, pp. 51–56, 2002.

[101] N. Sornkarn, P. Dasgupta, and T. Nanayakkara, "Morphological computation of haptic perception of a controllable stiffness probe," *PloS one*, vol. 11, no. 6, p. e0156982, 2016.

[102] M. Wiertlewski, J. Lozada, and V. Hayward, “The spatial spectrum of tangential skin displacement can encode tactual texture,” *IEEE Transactions on Robotics*, vol. 27, no. 3, pp. 461–472, 2011.

[103] S. Salehi, J. J. Cabibihan, and S. S. Ge, “Artificial skin ridges enhance local tactile shape discrimination,” *Sensors*, vol. 11, no. 9, pp. 8626–8642, 2011.

[104] N. Jamali, P. Byrnes-Preston, R. Salleh, and C. Sammut, “Texture recognition by tactile sensing,” in *Australasian Conference on Robotics and Automation (ACRA)*, Citeseer, 2009.

[105] Y. LeCun, Y. Bengio, and G. Hinton, “Deep learning,” *nature*, vol. 521, no. 7553, pp. 436–444, 2015.

[106] Z. Wang, Y. Torigoe, and S. Hirai, “A prestressed soft gripper: design, modeling, fabrication, and tests for food handling,” *IEEE Robotics and Automation Letters*, vol. 2, no. 4, pp. 1909–1916, 2017.

[107] F. Pedregosa, G. Varoquaux, A. Gramfort, V. Michel, B. Thirion, O. Grisel, M. Blondel, P. Prettenhofer, R. Weiss, V. Dubourg, *et al.*, “Scikit-learn: Machine learning in python,” *the Journal of machine Learning research*, vol. 12, pp. 2825–2830, 2011.

[108] E. Jones, T. Oliphant, P. Peterson, *et al.*, “Scipy: Open source scientific tools for python,” 2001.

[109] M. Abadi, A. Agarwal, P. Barham, E. Brevdo, Z. Chen, C. Citro, G. S. Corrado, A. Davis, J. Dean, M. Devin, *et al.*, “Tensorflow: Large-scale machine learning on heterogeneous distributed systems,” *arXiv preprint arXiv:1603.04467*, 2016.

[110] S. I. Rich, R. J. Wood, and C. Majidi, “Untethered soft robotics,” *Nature Electronics*, vol. 1, no. 2, pp. 102–112, 2018.

[111] J. M. Shick, *A functional biology of sea anemones.* Springer Science & Business Media, 2012.

[112] J. Shintake, V. Cacucciolo, D. Floreano, and H. Shea, “Soft robotic grippers,” *Advanced Materials*, vol. 30, no. 29, p. 1707035, 2018.

[113] H. Wang, M. Totaro, and L. Beccai, “Toward perceptive soft robots: Progress and challenges,” *Advanced Science*, vol. 5, no. 9, p. 1800541, 2018.

[114] K. Suzumori, S. Iikura, and H. Tanaka, “Development of flexible microactuator and its applications to robotic mechanisms,” in *Proceedings. 1991 IEEE International*

Conference on Robotics and Automation, pp. 1622–1623, IEEE Computer Society, 1991.

[115] F. Ilievski, A. D. Mazzeo, R. F. Shepherd, X. Chen, and G. M. Whitesides, "Soft robotics for chemists," *Angewandte Chemie*, vol. 123, no. 8, pp. 1930–1935, 2011.

[116] J. Shintake, S. Rosset, B. Schubert, D. Floreano, and H. Shea, "Versatile soft grippers with intrinsic electroadhesion based on multifunctional polymer actuators," *Advanced Materials*, vol. 28, no. 2, pp. 231–238, 2016.

[117] N. R. Sinatra, C. B. Teeple, D. M. Vogt, K. K. Parker, D. F. Gruber, and R. J. Wood, "Ultragentle manipulation of delicate structures using a soft robotic gripper," *Science Robotics*, vol. 4, no. 33, p. eaax5425, 2019.

[118] S. Terryn, J. Brancart, D. Lefeber, G. Van Assche, and B. Vanderborght, "Self-healing soft pneumatic robots," *Science Robotics*, vol. 2, no. 9, 2017.

[119] J. R. Amend, E. Brown, N. Rodenberg, H. M. Jaeger, and H. Lipson, "A positive pressure universal gripper based on the jamming of granular material," *IEEE transactions on robotics*, vol. 28, no. 2, pp. 341–350, 2012.

[120] S. Song and M. Sitti, "Soft grippers using micro-fibrillar adhesives for transfer printing," *Advanced Materials*, vol. 26, no. 28, pp. 4901–4906, 2014.

[121] T. Zhu, H. Yang, and W. Zhang, "A spherical self-adaptive gripper with shrinking of an elastic membrane," in *2016 International Conference on Advanced Robotics and Mechatronics (ICARM)*, pp. 512–517, IEEE, 2016.

[122] H. Zang, B. Liao, X. Lang, Z. L. Zhao, W. Yuan, and X. Q. Feng, "Bionic torus as a self-adaptive soft grasper in robots," *Applied Physics Letters*, vol. 116, no. 2, p. 023701, 2020.

[123] P. B. Scott, "The'omnigripper': a form of robot universal gripper.," *Robotica*, vol. 3, no. 3, pp. 153–158, 1985.

[124] A. Mo and W. Zhang, "A novel universal gripper based on meshed pin array," *International Journal of Advanced Robotic Systems*, vol. 16, no. 2, p. 1729881419834781, 2019.

[125] Y. Park, G. Vella, and K. J. Loh, "Bio-inspired active skins for surface morphing," *Scientific reports*, vol. 9, no. 1, pp. 1–10, 2019.

[126] T. Takahashi, K. Nagato, M. Suzuki, and S. Aoyagi, "Flexible vacuum gripper with autonomous switchable valves," in *2013 IEEE International Conference on Robotics and Automation*, pp. 364–369, IEEE, 2013.

[127] S. Wang, H. Jiang, and M. R. Cutkosky, "A palm for a rock climbing robot based on dense arrays of micro-spines," in *2016 IEEE/RSJ International Conference on Intelligent Robots and Systems (IROS)*, pp. 52–59, IEEE, 2016.

[128] J. Shintake, E. Piskarev, S. H. Jeong, and D. Floreano, "Ultrastretchable strain sensors using carbon black-filled elastomer composites and comparison of capacitive versus resistive sensors," *Advanced Materials Technologies*, vol. 3, no. 3, p. 1700284, 2018.

[129] K. Elgeneidy, N. Lohse, and M. Jackson, "Bending angle prediction and control of soft pneumatic actuators with embedded flex sensors–a data-driven approach," *Mechatronics*, vol. 50, pp. 234–247, 2018.

[130] T. H. Yang, J. Shintake, R. Kanno, C. R. Kao, and J. Mizuno, "Low-cost sensor-rich fluidic elastomer actuators embedded with paper electronics," *Advanced Intelligent Systems*, p. 2000025.

[131] M. Tavakoli, P. Lopes, J. Lourenco, R. P. Rocha, L. Giliberto, A. T. de Almeida, and C. Majidi, "Autonomous selection of closing posture of a robotic hand through embodied soft matter capacitive sensors," *IEEE Sensors Journal*, vol. 17, no. 17, pp. 5669–5677, 2017.

[132] S. Ozel, N. A. Keskin, D. Khea, and C. D. Onal, "A precise embedded curvature sensor module for soft-bodied robots," *Sensors and Actuators A: Physical*, vol. 236, pp. 349–356, 2015.

[133] I. Van Meerbeek, C. De Sa, and R. Shepherd, "Soft optoelectronic sensory foams with proprioception," *Science Robotics*, vol. 3, no. 24, 2018.

[134] P. Polygerinos, N. Correll, S. A. Morin, B. Mosadegh, C. D. Onal, K. Petersen, M. Cianchetti, M. T. Tolley, and R. F. Shepherd, "Soft robotics: Review of fluid-driven intrinsically soft devices; manufacturing, sensing, control, and applications in human-robot interaction," *Advanced Engineering Materials*, vol. 19, no. 12, p. 1700016, 2017.

[135] K. Sato, K. Kamiyama, N. Kawakami, and S. Tachi, "Finger-shaped gelforce: sensor for measuring surface traction fields for robotic hand," *IEEE Transactions on Haptics*, vol. 3, no. 1, pp. 37–47, 2009.

[136] R. Li, R. Platt, W. Yuan, A. ten Pas, N. Roscup, M. A. Srinivasan, and E. Adelson, "Localization and manipulation of small parts using gelsight tactile sensing," in *2014 IEEE/RSJ International Conference on Intelligent Robots and Systems*, pp. 3988–3993, IEEE, 2014.

[137] B. Ward Cherrier, N. Pestell, L. Cramphorn, B. Winstone, M. E. Giannaccini, J. Rossiter, and N. F. Lepora, "The tactip family: Soft optical tactile sensors with 3d-printed biomimetic morphologies," *Soft robotics*, vol. 5, no. 2, pp. 216–227, 2018.

[138] B. Ward Cherrier, L. Cramphorn, and N. F. Lepora, "Tactile manipulation with a tacthumb integrated on the open-hand m2 gripper," *IEEE Robotics and Automation Letters*, vol. 1, no. 1, pp. 169–175, 2016.

[139] C. Xiang, J. Guo, and J. Rossiter, "Soft-smart robotic end effectors with sensing, actuation, and gripping capabilities," *Smart Materials and Structures*, vol. 28, no. 5, p. 055034, 2019.

[140] L. Shui, L. Zhu, Z. Yang, Y. Liu, and X. Chen, "Energy efficiency of mobile soft robots," *Soft Matter*, vol. 13, no. 44, pp. 8223–8233, 2017.

[141] Z. Zhang, Y. Li, X. Yu, X. Li, H. Wu, H. Wu, S. Jiang, and G. Chai, "Bistable morphing composite structures: A review," *Thin-walled structures*, vol. 142, pp. 74–97, 2019.

[142] M. Taffetani, X. Jiang, D. P. Holmes, and D. Vella, "Static bistability of spherical caps," *Proceedings of the Royal Society A: Mathematical, Physical and Engineering Sciences*, vol. 474, no. 2213, p. 20170910, 2018.

[143] A. Brinkmeyer, M. Santer, A. Pirrera, and P. Weaver, "Pseudo-bistable self-actuated domes for morphing applications," *International Journal of Solids and Structures*, vol. 49, no. 9, pp. 1077–1087, 2012.

[144] P. Sobota and K. Seffen, "Effects of boundary conditions on bistable behaviour in axisymmetrical shallow shells," *Proceedings of the Royal Society A: Mathematical, Physical and Engineering Sciences*, vol. 473, no. 2203, p. 20170230, 2017.

[145] P. Rothemund, A. Ainla, L. Belding, D. J. Preston, S. Kurihara, Z. Suo, and G. M. Whitesides, "A soft, bistable valve for autonomous control of soft actuators," *Science Robotics*, vol. 3, no. 16, 2018.

[146] Y. Tang, Y. Chi, J. Sun, T.-H. Huang, O. H. Maghsoudi, A. Spence, J. Zhao, H. Su, and J. Yin, "Leveraging elastic instabilities for amplified performance: Spine-inspired high-speed and high-force soft robots," *Science Advances*, vol. 6, no. 19, p. eaaz6912, 2020.

[147] B. Gorissen, D. Melancon, N. Vasios, M. Torbati, and K. Bertoldi, "Inflatable soft jumper inspired by shell snapping," *Science Robotics*, vol. 5, no. 42, 2020.

[148] Y. Wang, U. Gupta, N. Parulekar, and J. Zhu, “A soft gripper of fast speed and low energy consumption,” *Science China Technological Sciences*, vol. 62, no. 1, pp. 31–38, 2019.

[149] E. Loukaides, S. Smoukov, and K. Seffen, “Magnetic actuation and transition shapes of a bistable spherical cap,” *International Journal of Smart and Nano Materials*, vol. 5, no. 4, pp. 270–282, 2014.

[150] E. Eckstein, A. Pirrera, and P. M. Weaver, “Thermally driven morphing and snap-through behavior of hybrid laminate shells,” *AIAA Journal*, vol. 54, no. 5, pp. 1778–1788, 2016.

[151] 3D printers canada, *Tango Materials Product Brochures.*

Publications

Journal Paper

[1] Q. Qi and V. Ho, “Wrinkled Soft Sensor with Variable Afferent Morphology: Case of Bending Actuation”, *IEEE Robot. Autom. Lett.*, vol. 5, no. 3, pp. 4102 - 4109, 2020.

[2] Q. Qi, S. Hirai and V. Ho, “Wrinkled Soft Sensor with Variable Afferent Morphology”, *IEEE Robot. Autom. Lett.*, vol. 4, no. 2, pp. 1908 - 1915, 2019.

[3] Q. Qi, C. Xiang, V. Ho and J. Rossiter, “A Sea-Anemone-Inspired, Energy-Efficient Universal Gripper with Multifunctionality”, *Soft Robot.*. (Under Review)

International Conference

[4] Q. Qi, S. Yoshida, G. Kakihana, T. Torii, V. Ho and H. Xie, “BPActuators: Lightweight and Low-Cost Soft Actuators Fabricated with Balloons and Plastics”, *IEEE International Conference on Soft Robotics (RoboSoft 2021). (Under Review)*

[5] J. Guo, D. Kuhnel, Q. Qi, C. Xiang, V. Ho, C. Faul and J. Rossiter, “A Soft, Portable Electroadhesive Gripper by Laser-scribing Graphene Oxide on a Silicone File”, *IEEE International Conference on Robotics and Automation (ICRA 2021). (Under Review)*

International Conference for Oral Presentation

[6] Q. Qi and V. Ho, “Wrinkled Soft Sensor With Variable Afferent Morphology: Case of Bending Actuation”, *IEEE International Conference on Soft Robotics (RoboSoft 2020)* Online. (Best Paper Finalist)

[7] Q. Qi, S. Hirai and V. Ho, ”Wrinkled Soft Sensor With Variable Afferent Morphology”, *IEEE International Conference on Robotics and Automation (ICRA 2019)* May 20 - 24, Montreal Canada.

[8] Q. Qi and V. Ho, “Variable Afferent Network Morphology (VANmorph): An Implementation on Sensorized Soft Body”, *IEEE International Conference on Intelligent Robots and Systems (IROS 2018)* October 1 - 5, Madrid Spain. (Late Breaking Results Posters)